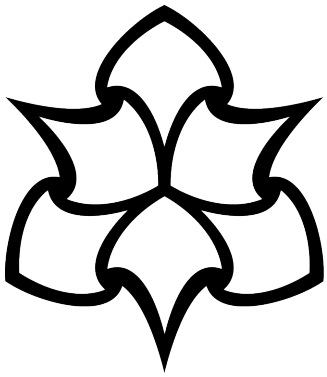

AN AUTONOMOUS AND INTELLIGENT SYSTEM FOR ROTATING MACHINERY DIAGNOSTICS

SIEW HON TEAY

PhD 2015

AN AUTONOMOUS AND INTELLIGENT SYSTEM FOR ROTATING MACHINERY DIAGNOSTICS

SIEW HON TEAY

A thesis submitted in partial fulfilment of the requirements of the
Manchester Metropolitan University for the degree of
Doctor of Philosophy

School of Engineering
Faculty of Science and Engineering
Manchester Metropolitan University
2015

Abstract

Rotating machinery diagnostics (RMD) is a process of evaluating the condition of their components by acquiring a number of measurements and extracting condition related information using signal processing algorithms. A reliable RMD system is fundamental for condition based maintenance programmes to reduce maintenance cost and risk. It must be able to detect any abnormalities at early stages to allow preventing severe performance degradation, avoid economic losses and/or catastrophic failures. A conventional RMD system consists of sensing elements (transducers) and data acquisition system with a compliant software package. Such system is bulky and costly in practical deployment. The recent advancement in micro-scaled electronics have enabled wide spectrum of system design and capabilities at embedded scale. Micro electromechanical system (MEMS) based sensing technologies offer significant savings in terms of system's price and size. Microcontroller units with embedded computation and sensing interface have enabled system-on-chip design of RMD system within a single sensing node.

This research aims at exploiting this growth of microelectronics science to develop a remote and intelligent system to aid maintenance procedures. System's operation is independent from central processing platform or operator's analysis. Features include on-board time domain based statistical parameters calculations, frequency domain analysis techniques and a time controlled monitoring tasks within the limitations of its energy budget. A working prototype is developed to test the concept of the research. Two experimental testbeds are used to validate the performance of developed system: DC motor with rotor unbalance and 1.1kW induction motor with phase imbalance. By establishing a classification model with several training samples, the developed system achieved an accuracy of 93% in detecting quantified seeded faults while consumes minimum power at 16.8mW. The performance of developed system demonstrates its strong potential for full industry deployment and compliance.

Declaration

No portion of the work referred to this Thesis has been submitted in support of an application for another degree or qualification of this or any other university or other institution of learning.

Copyright

Acknowledgements

First and foremost I want to thank my Director of Studies, Dr. Alhussein Albarbar. It has been an honour to be his Ph.D. student. He has encouraged and guided me, consciously and instinctively in my research not only to grow as a research student but also as an experimentalist and independent thinker. As a tremendous mentor for me I appreciate all his contributions of time, ideas, guidance, understanding, patience, and most importantly, his friendship to make my Ph.D. experience productive and stimulating. At times, the joys, enthusiasm, chastises and reprimands were contagious and motivational for me, even during tough times in the Ph.D. pursuit.

I would also like to thank my cousin brother, Associated Professor Dr. Shawyun Teay (KSU) for his excellent guidance, comments and many insightful discussions and suggestions. I am fortunate to have a cousin brother who was there for me during the Thesis writing ordeal to help me quickly proofread and copy-edit and was instrumental in helping me crank out this Thesis, within the tight schedule.

My university time in Manchester was made enjoyable in large part due to the many friends and groups that became a part of my life. I am grateful for the time spent with roommates and friends, and for many other people (too many to list here). The memories were also enriched by my spiritual teacher from Fo Guang Shan Temple, who blessed me with prayer on my endeavour. I specially would like to thank my Auntie Koonlin Eunice Chan who constantly bestowed her maternal love of encouragement and wisdom during my moment of desolation. She is like a god-mother to me now. I would also like to express my gratitude to Cathleen Liu for always being around and supportive throughout my time here and for helping me to stay psychologically strong and sane. I regard her as a big sister. And thank you also to Dr. Chandra Sarat Vegunta, Dr. Alex Tan and Kai Xian Won who always cheer me up and stood by me through the good times and bad.

I sincerely appreciate the organisation: The British Atmospheric Data Centre (BADC) for providing me decades of solar irradiance data for my analysis and lab simulation for solar harvesting application. I also thank the wonderful staff in the Lab-Tech Department for the hands-on assistance on setting up the experiments as well as in other departments for always being so nice and friendly. People here are genuinely helpful that I am glad to have interacted with so many. I apologise if I have forgotten anyone.

Lastly, I would like to thank my family for all their unconditional love and encouragement. For my parents who raised me and believe me in all my pursuits. My brother, Siew Yen has been non-judgmental of me and instrumental in instilling confidence, faith in my intellect both academically and personally to count on when times are rough during the final stages of this Ph.D. is so appreciated.

Contents

List of figures

List of Tables

Nomenclature

ADC	Analogue-digital converter
AI	Artificial intelligence
ANN	Artificial neural network
API	Application programming interface
CBM	Condition-based maintenance
DAC	Digital-analogue converter
DFT	Discrete Fourier transform
DSP	Digital signal processing
EEPROM	Electrically erasable programmable read-only-memory
ENO	Energy neutral operation
ESR	Equivalent series resistance
FFT	Fast Fourier transform
GBI	Global business intelligence
GPIO	General purpose input output
GSM	Global system for mobile
IC	Integrated circuit
IDE	Integrated development environment
IEEE	Institute of Electrical and Electronics Engineers
IMSEM	Intelligent monitoring sensor for e-maintenance
IS	Intelligent sensor
ISM	Industrial, scientific and medical
IFSA	International Frequency Sensor Association
ISR	Interrupt service routine
LPF	Low pass filter
MCM	Machinery condition monitoring
MCU	Microcontroller unit
MEMS	Micro electromechanical system
NEMA	National electrical manufacturers association
OSA-CBM	Open standard architecture – condition-based maintenance
OSA-EAI	Open standard architecture – Enterprise application integration
PCA	Principal component analysis
PGA	Programmable gain amplifier
PSoC	Programmable system-on-chip
PV	Photovoltaic
PWM	Pulse width modulation

P2P	Peer-to-peer
RBF	Radial basic function
RF	Radio frequency
RMD	Rotating machine diagnostics
RMS	Root mean square
SAR	Successive approximation
SD	Secure digital
SIVEH	Similar I-V for energy-harvesting
SoC	State of charge
SoDC	State of discharge
SPI	Serial peripheral interface
SRAM	Static random access memory
UART	Universal asynchronous receiver/transmitter
XML	eXtensible Mark-up Language

Chapter 1
Introduction

This chapter provides an overview of rotating machinery diagnostics, embedded smart sensing technology and discusses the research questions and novelty of the project. The aim and objectives are outlined at the end of the chapter.

1.1 Rotating machinery diagnostics

Rotating machinery diagnostics (RMD) is usually based on non-destructive machinery condition monitoring (MCM) strategy that measures and indicates rotating machine defects to avoid malfunction, degradation or catastrophic failures. It is recognised as one of the key factors in manufacturing and production plants for improving their quality of productivity and efficiency. As highlighted in [1], the implementation of MCM provides the following advantages:

- Achieved savings of 1.2% on value-added input (for example: material costs, hardware cost, etc.).
- Reduced unscheduled shutdown time by 75%.
- Reduced breakdown labour costs by 50%.

Today, RMD receives various attentions as a potential tool for maintenance engineering. The total expenses in terms of maintenance costs can be greater than any investment within a complete lifecycle of a manufacturing plant [2], as shown in Figure 1-1.

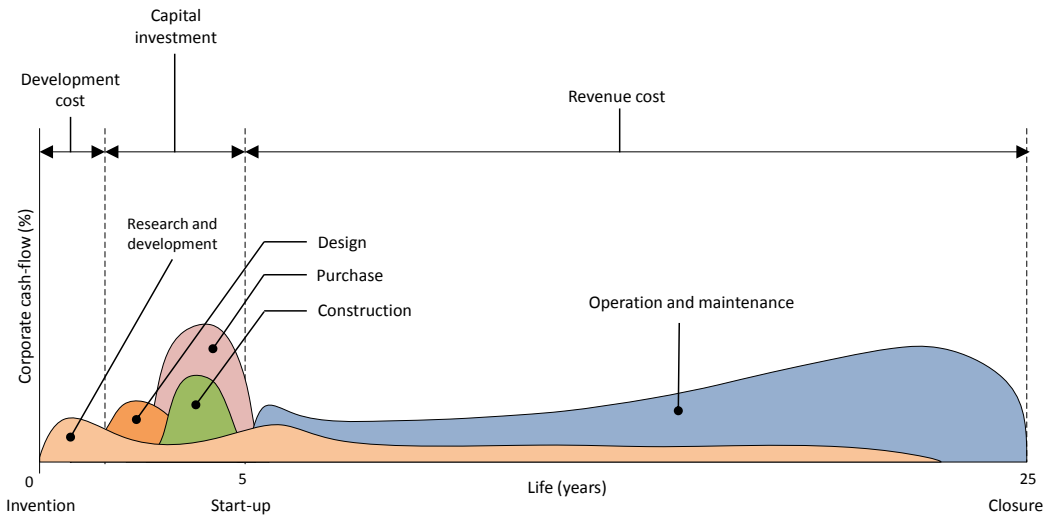

Figure 1-1: A lifecycle cost profile of a plant [2]

1.1.1 Overview

RMD is a kind of predictive maintenance strategy (fix it when it is right-on-time) in maintenance engineering. In general, there are three approaches in maintenance: reactive maintenance (fix it when it breaks), preventive maintenance (fix it when it is time) and predictive maintenance (fix it when it is right-on-time). Reactive maintenance suffers from service downtime and human risks, which degrade the overall performance of the plants. Despite preventive maintenance being effective in reducing service downtime, it is inefficient when the maintenance is applied to healthy machines. One of the major overhaul facilities reports that 60% of hydraulic pumps sent in for rebuild had nothing wrong with them [3]. Bloch et al. have also stated that, 'one out of three dollars spent on preventive maintenance is wasted [4]. Therefore, predictive maintenance provides efficient solution based on the aspects of cost and operating efficiency. It is a condition-based maintenance (CBM) strategy, which makes timely decisions for suitable maintenance based on the health condition and reliability of the machine.

There are various physical attributes being used as quantitative parameters for RMD: vibration, acoustic emission, thermography, lubricant oil, motor voltage and current. Respective sensing units include accelerometer, microphone, infrared thermography camera, voltmeter and clampmeter. These physical attributes are then transferred to the sensing channel for further processing. Among all physical entities, vibration monitoring is one of the most common techniques applied for machinery fault diagnostics. Throughout the past decades, various approaches of vibration monitoring have been developed [5]–[8].

1.1.2 Evolution of rotating machinery diagnostics

Since the early 1970s, RMD system has attracted attention as a potential monitoring strategy to improve machinery operating lifetime. Ontario Hydro has introduced an on-site portable instrument for monitoring partial discharge and on-

line cable type permanent couplers. This unit has been widely applied to hydro generator units. The monitoring modules have evolved through continuously emerging latest technology. In early 1990s, a Canadian company – IRIS has developed an on-site portable monitoring unit for operating turbine generator [9]. Nowadays, digital computer technology plays important roles in RMD systems. Analogue-digital agent such as analogue-digital converter (ADC) translates continuous waveforms to discrete signals, which is recognised by digital computer platforms. With rapid growth of computer technology, such monitoring systems have become the main trends of RMD system in industry. The monitoring circulation of RMD system is illustrated in Figure 1-2. In Figure 1-2, single or multiple sensing nodes are attached on operating components to acquire ambient physical measurand. The sensing nodes convert the target measurand into electrical signals and transmit to a monitoring system, which is built with signal conditioning module. Multiple monitoring systems transmit processed measurement signals to central computer unit for further computer analysis and data logging.

In late 1990s and early 2000s, scientists and developers have started to integrate digital computer with RMD systems. The research outcomes are well discussed by [4], [10]. These have led to a wider research spectrum for RMD systems in computer technology. In numerical computation, various signal processing techniques have been developed [6], [11], [12]. Artificial intelligence (AI) has also been implemented to enhance machinery condition diagnostics [13]–[15].

Current RMD system requires expensive hardware and software installation. Moreover, human expert is required to utilise the system effectively. Figure 1-3 shows a complete RMD system consisting sensing nodes, sensing channel, signal conditioning unit, computational core and man-machine interface. A robust monitoring system for RMD requires expensive installation and training cost. This has limited the deployment of RMD system at small or medium industries.

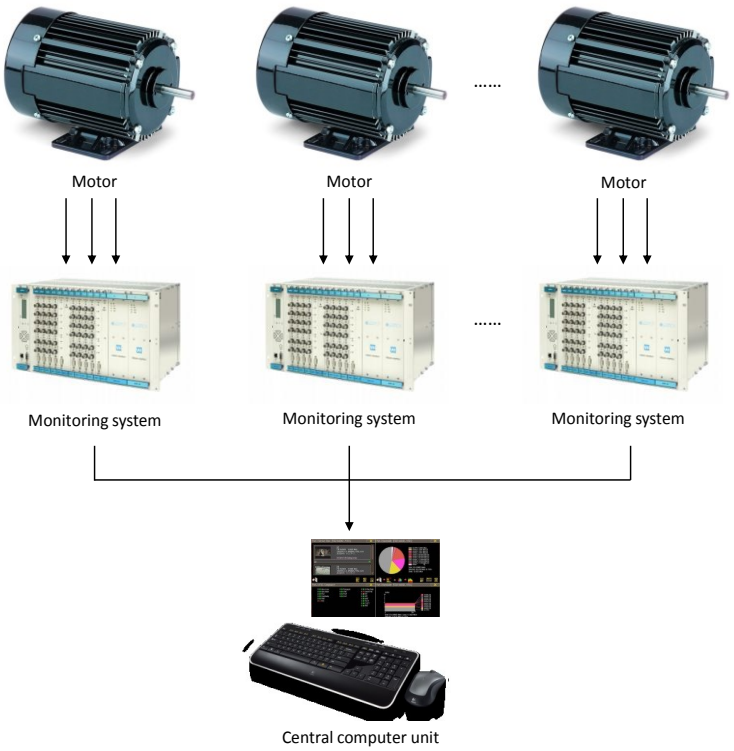

Figure 1-2: Monitoring system with multiple units of operating rotating machines

Recent microelectronic technology has enabled the electronic device to be established in micrometric volume, which dramatically improves the performance, functionality and reliability while reducing cost and size of deployment. Recent publications have focused on integrating microelectronic technology with RMD scheme, aiming to reduce cost and complexity of RMD deployment. One attribute that is benefited from the microelectronic is smart sensing technology, which serves as an important component of the future trends of RMD system.

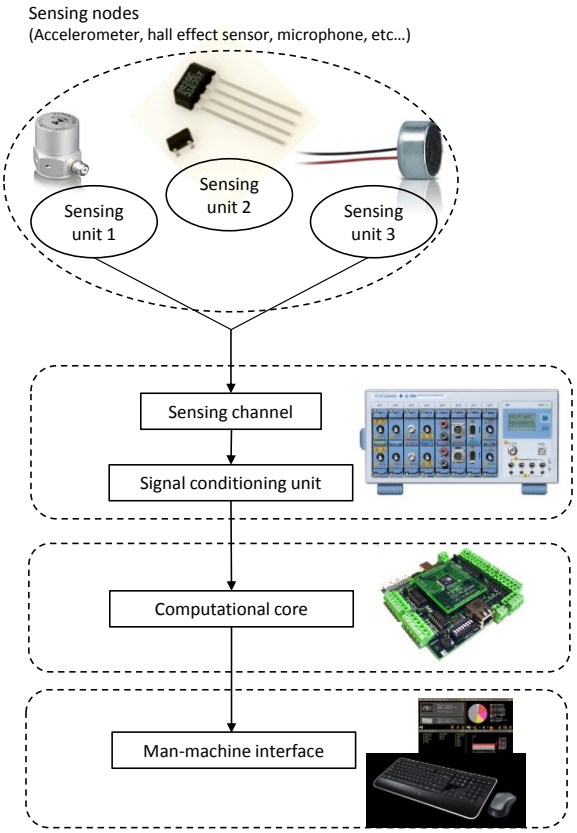

Figure 1-3: Fundamental functional unit of RMD system with computer technology.

1.2 Smart sensing technology

1.2.1 Overview

Smart sensing technology or smart sensors, is generally described as "a set of open, common, network independent communication interfaces for connecting transducers (sensors or actuators) to microprocessors, instrumentation systems, and control/field networks" [16], [17]. A complete smart sensing technology consists of sensing unit, sensing channel, signal conditioning unit, microprocessor and data communication module (wired or remote). Its respective features cover signal accumulation, signal conditioning, signal processing, feature extraction and decision making. Kim et al. have reported by implementing wireless monitoring unit has significantly reduced the sensing development cost by approximate 95% [18]. Their

survey on cost and evaluation of condition monitoring and diagnosis system is tabulated in Table 1-1.

Researchers foresee that smart sensing is the future trend to develop an intelligent system for RMD systems. Recent publications have discussed the design of new sensing framework for different applications for RMD [13], [19], [20].

Smart sensing unit with micro-metric computational core plays important role to manage the whole functionality of smart sensor. The recent growth of microcontroller from 16-bit to 32-bit has expanded the choice of system design. Their application on RMD system is briefly investigated in section 1.2.2.

Table 1-1 Cost comparison between currently available technologies and smart sensing unit

Type of unit	Cost of sensing nodes (S)/local sensing channel (L)	Cost of central control unit or portable unit
Conventional on-site portable monitoring unit	$6,000 (S)	$60,000
Continuous on-line monitoring unit	$6,000 (S) $30,000 (L)	$60,000
Digital computer monitoring unit	$6,000 (S) $3,000 (L)	$3,000
Smart sensing unit	$300 (S) and (L) integration	$2,000
Embedded smart sensing unit	$100 (S) and (L) integration	$2,000

1.2.2 Embedded systems and microcontrollers

Embedded system plays important roles to develop a decentralised intelligent sensor (IS) system. Being one of the subset in an embedded system, the microcontroller unit (MCU) has been widely deployed in many electronic appliances. By integrating a processor core, memory and various input/output peripherals in a single chip, MCU is the suitable choice to realise low cost system without undergoing a complicated development process. According to Global Business Intelligence

Research (GBI), the MCU market currently constitutes around 5% of the overall semiconductor market, and around 24% of the micro integrated circuit market in revenues [21]. Moreover, a faster learning curve and development time makes the MCU surpass other system-on-chip in the system design process.

The newer 32-bit microcontrollers have potential to realise the development of miniaturised embedded system. With the width of 32 data paths, a 32-bit MCU achieves faster speed and larger fragmented memory space as compared to the 8-bit and 16-bit microcontroller, which suit the niche where real-time processing is obligatory [22]. It is expected that the 32-bit MCU will become a key contestant in the next several years of electronic market. Complementing its high performance, marketing research has predicted that 32-bit MCU price tags will drop to $2.88 by 2014 [23].

Nowadays, MCU offers a wide spectrum of design application for various developments. Digital signal controllers are available for applications which require faster signals processing while maintaining the programming attributes of MCU. Sample products include dsPIC by Microchip Technology, LPC4300 by NXP Semiconductors and 56F803X by Freescale. The mixed signal microcontroller by Cypress, namely Programmable system-on-chip (PSoC) is a software-controlled mixed-signal array with MCU-typed architecture. With configurable digital and analogue blocks in its integrated development environment (IDE), Cypress PSoC enables users to quickly design either an analogue or digital embedded system. These enable a more flexible range in designing an application specified system of IS for RMD.

1.2.3 Smart sensors for rotating machinery diagnostic

The development of microelectronics and RMD systems are two major research areas of modern engineering. Recent publications have highlighted the use of smart sensing technology in the field of RMD [20], [24], [25]. With predefined action on the

integrated circuit (IC), this reduces the workload and power consumption between the sensor node and central operation unit, which is normally operated by computing hub or skilled operator. The growth of microcontroller has realised the multiple integrated modules which containing a microprocessor, memory, and programmable input/output peripherals in a single chip.

Currently, there are several issues that need to be addressed in order to realise the deployment of IS on RMD system:

- Intelligence – The current commercial smart sensing system for RMD has lower intelligence to carry out independent fault diagnostics as they only extract information from raw signals without any intelligence for decision making. With the advancement on computing technology, AI has the potential capability to generate end-result on decentralised sensing level. Various integrations of AI on RMD have shown promising result. Their implementation on embedded miniaturised system gives possibilities to establish an intelligent RMD system.
- System resource – Embedded microcontroller has limited processing speed and memory compared to conventional MCM system, which commonly runs on a central computer unit. Monitoring algorithms have to be miniaturised before implementing them onto embedded system.
- Robustness – Microcomputer or embedded system has wide deployment in commercial products. However, they have less applicability in heavy industries. These applications demand a very robust system to carry out monitoring tasks. Micro-electromechanical (MEMS) sensors have proven its performance in working harsh environment [26], while embedded microcontroller has typical -40^{o}C to 90 ^{o}C operating temperature [27]–[29]. The niche of IS on MCM should be well identified to assure its application.

- Sustainability – Wireless sensor is a variation of modern sensors to enable remote sensing operations. They are more advantageous in the aspects of installation and transplantation. In order to operate wirelessly, their power ratings become one of the most important criterions. Traditional wireless sensor uses battery as their primary sources. However, it needs replacement and occasionally is inconvenient when the sensor is installed at difficult location. Recent researches on power harvesting has the potential to solve this problem [30], [31]. This includes harvesting energy from solar, thermoelectric or mechanical vibration. On software layer, the sensor should have the ability to save energy by putting it into a hibernate/sleep mode.

1.2.4 Energy efficiency and sustainability

Energy capacity is key concern when designing a remote smart sensing unit. Possible candidate of energy providers include:

- Wired power supply
- Battery
- Rechargeable battery (Examples are: Nickel cadmium battery, nickel metal hydrate battery, lithium ion battery etc.)
- Supercapacitors

Each candidate has their pros and cons as an efficient energy provider. To provide longer operating lifespan, rechargeable batteries and supercapacitors are two main candidates which are widely used in wireless smart sensing unit. Their energy characteristic in respective energy and power density can be evaluated using Ragone chart, as shown in Figure 1-4 [32].

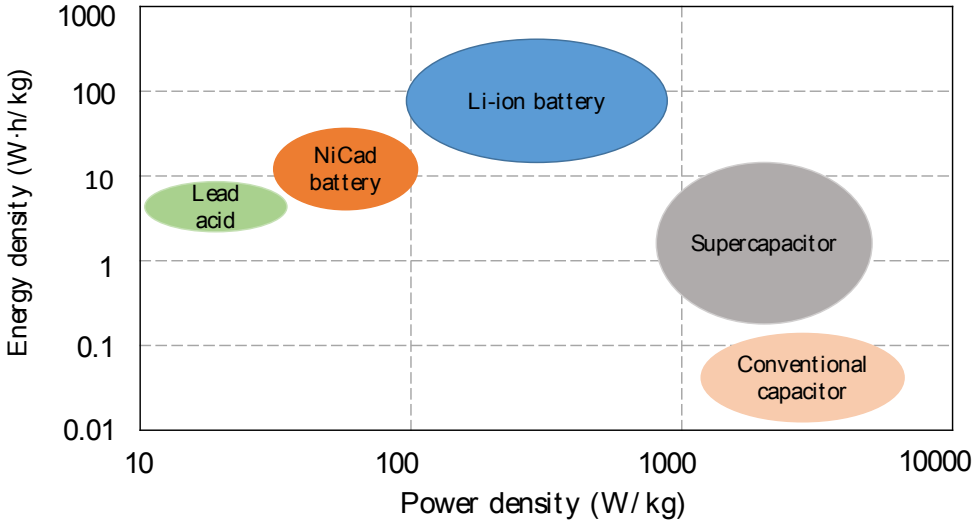

Figure 1-4 Energy characteristics of different rechargeable batteries [32]

Researchers and developers are emphasising the design of an energy aware sensing node to reduce power consumption. Sanchez et at. have recommended an intelligent sensing system through the integration of energy efficient module, such as energy harvesting unit and energy buffer module [33]. Other research have considered power management scheme when designing smart sensing unit [34], [35].

1.3 About this research

Wide research continuums are available to enhance the deployment of intelligent system for RMD engineering. In this section, a specific research direction is outlined. The motivation, originality and limitation of the research are also addressed.

1.3.1 Motivation

Smart sensing technology has broaden the research spectrum of RMD system in the prospects of cost, effective and intelligence level on machinery fault diagnostic. Based on this broader spectrum of research, the research questions which drive the motivation of this project can be listed as follows:

- *Development of an intelligent system using embedded microcontroller* – Conventional system for rotating machines relies on huge loads of

transmission data between the sensing node and the central processing unit. A decentralised intelligent sensing system will be beneficial to reduce continuous monitoring of central processing or operator analysis by performing signal analysis, fault detection and decision making on the sensor itself.

- *Power characteristics of intelligent system* – A low-power intelligent sensing system is desirable as it has longer operating period and is cost effective.

1.3.2 Novelty

The novelty of the project comprises the design and development of a smart sensing framework for RMD system. It is believed that such a miniaturised system has the potential to become the trend of modern sensors in the future. They have major advantages over conventional sensors in the aspects of user experience and power management. The sought sensing unit has the ability to carry out signal acquisition, signal conditioning, feature extraction and fault detection independently.

Conventional system for RMD requires bulky hardware to establish the monitoring process. Such system has no intelligence or computational capability on sensing level, leading all analysis and classification process to be carried out at central computing hub or by human expert. In this research, it is envisioned that the miniaturised IS has the potential to integrate all necessary features of the conventional system in a system-on-chip, featuring signal analysis and classification on decentralised IS. This novel concept reduces cost and installation complication, which enable the deployment of RMD system in larger spectrum. Moreover, the developed IS has multiple sensing channels, which allow multi-motor monitoring with a single sensing unit.

To improve operation sustainability, the integration of energy harvesting and energy storage module by using supercapacitor is taken into account. The global

solar irradiance in Manchester area is studied. The feasibility of energy storage using solar is studied together with the power budget of the sensor to analyse result and design of an energy aware smart sensing unit for RMD system.

1.3.3 Scope of research

The research work is partitioned in 3 major aspects: functionality, feasibility and sustainability of IS for RMD system. The functionality emphasises on the capability of the sensor in signal analysis and decision making. Feasibility covers the compatibility issue of the sensor with existing RMD technology. The sustainability aspect discusses the energy awareness issues of the developed sensor.

On hardware level, microcontroller device is chosen as the main component unit of intelligent system. Other possible system-on-chips such as Beagle Bone and Raspberry Pi are omitted due to their energy-hungry characteristics. Also, field programmable gate array-typed solutions are not discussed in this research due to their complicated development nature to realise the system design. Energy harvesting module is studied and analysed in simulation due to the limited time to gather experimental result throughout the year based on the global solar irradiance in Manchester. The energy characteristic of simulation model is then validated with experimental data to ensure its accuracy.

Performance of the working prototype is validated through two experimental test-beds: Fault diagnostics on DC motor with rotor unbalance and 3-phase induction motor with phase imbalance. At first, several training samples are collected to train the classification model of the developed sensor. Then, the classification model is evaluated through test sample. A simple diagnostics report is then sent to central computer unit as sensor's performance assessment and logging.

1.3.4 Defining the proposed intelligent sensor model

With modern e-business strategy, the developed sensing unit can be deployed for e-maintenance. In this section, the working prototype is defined as Intelligent

Monitoring Sensor for E-Maintenance (IMSEM). This acronym will be used to refer the working prototype throughout the Thesis.

1.4 Research aim and objectives

1.4.1 Aim

The aim of this research project is to investigate and develop a novel intelligent monitoring sensor for RMD. The proposed system is decentralised to eliminate the needs for huge amount of data transmission and system complexity between sensor node and central control unit.

1.4.2 Objectives

To effectively carry out the tasks of the research, following objectives are outlined:

- To review the research status in the deployment of smart sensors for machinery condition monitoring and diagnostics.
- To design an embedded monitoring system with on-board feature extraction, feature comparison and decision-making.
- To establish a low-power wireless communication system using XBee.
- To apply time and frequency domain analysis on rotating machinery induced vibration, such as Fourier transform.
- To implement hibernate mode and other power management techniques to prolong operation life.
- To validate the performance of working prototype using an induction motor test rig running under different operating conditions.
- To design, build and test a final working prototype with a friendly user interface.

1.5 Organisation of the Thesis

The Thesis can be divided into two sections: design of low cost wireless intelligent system as the fundamental sensing module for RMD. The embedded signal processing and computational capabilities enable the sensing unit to carry out monitoring task without the human involvement, whilst maintaining its hybrid configuration for advanced monitoring tasks carried out by human experts. The signal and monitoring data will be stored in the sensing unit module, for future data logging and trend analysis.

The latter section of the Thesis explores the feasibility of energy-aware system on the working intelligent sensor system. Here, energy harvesting and energy storage module are studied to realise their current technology status for the implementation for remote sensing unit. Surrounding global solar irradiance and temperature are taken into account to evaluate the performance of the sensing unit in Manchester. After that, improved power management strategy is outlined for the sensing unit for future network implementation.

This Thesis is organised as follows:

Chapter 2 presents the literature survey of the project. Current research and development in the target field of research is studied. Suitable technology and knowledge are highlighted for the design of the novel intelligent sensing unit for RMD.

Chapter 3 discusses the generic framework of the intelligent sensing unit. This comprises of sensing nodes, signal conditioning circuitry, core computational unit, wireless communication interface and other peripheral embedded module.

Chapter 4 presents the software architecture of the intelligent sensing unit. The software design is done in 3 abstraction layers: signal processing, feature extraction and decision making. To provide better industrial implementation, an open standard for MCM system is also studied and integrated into the developed sensing unit.

Chapter 5 elaborates on respective power management module. Different energy entropies are investigated to design an efficient power management module for the sensor. Energy storage unit is discussed and its performance is simulated to validate the performance of the module. Energy budget of developed system is addressed at the latter part of the chapter.

To validate the performance of the sensing unit, Chapter 6 discusses the experimental result. The practical exercises of the sensing unit on motor test-rigs are elaborated. Outcomes, problems and result discussion are the core element of this chapter.

To conclude the research study, Chapter 7 serves as a Thesis summary with the addressed aim and objectives. Contributions to the knowledge of RMD fields are also outlined. Future works to improve the developed system are also addressed.

Chapter 2
Literature review

This chapter presents the literature survey of the project. Current research and development on target field is studied. Suitable technology and knowledge are highlighted for the design of the novel intelligent sensing unit for RMD. The research synthesis is outlined at the end of the chapter, addressing the main direction of the project.

2.1 Overview

In the first chapter a general introduction to the Thesis, aim and objectives are defined to design an intelligent sensing system for RMD. In this chapter the literature review on related research fields are discussed in detail. The discussion topics include intelligent sensor (IS), modern maintenance strategies and power management systems. These 3 topics are inter-related as they enhance the functionality, feasibility and sustainability of intelligent sensing systems for RMD. In the latter part of this chapter, research problems are formulated as core research areas of the Thesis, setting up research directions for subsequent chapters.

2.2 Functionality – Intelligent sensor

2.2.1 Defining intelligent sensor

The definition of IS is vague. In 2009, the committee board of International Frequency Sensor Association (IFSA) took a survey titled "What does smart sensor mean and what does it constitute?", which 227 participants from both academia and industry participated in the survey. Their perspectives on smart and ISs are shown in Figure 2-1. From the survey, majority has the impression that smart sensor's definition refers to Institute of Electrical and Electronics Engineers (IEEE) 1451 compliant sensor category. At the end of the survey, Yurish et al. concluded that most professional individuals describe IS as "a sensing node which has additional hardware or software implementation than transmitting raw signals" [36].

In the Thesis, the IS is defined as "functional wireless sensor incorporated with sensing nodes to process higher level information from accumulated measurands".

2.2.2 Intelligent sensor for condition monitoring

The criterion for designing an IS can be outlined as:

- Consisting of sensing nodes to carry out signal acquisition.

- Integrating built-in signal conditioning and processing modules to coordinate measured signals.
- Embedding AI to process information which has higher level computational features than sending only raw signals.
- Interfacing wireless communication interface which transmits date remotely to other platforms.

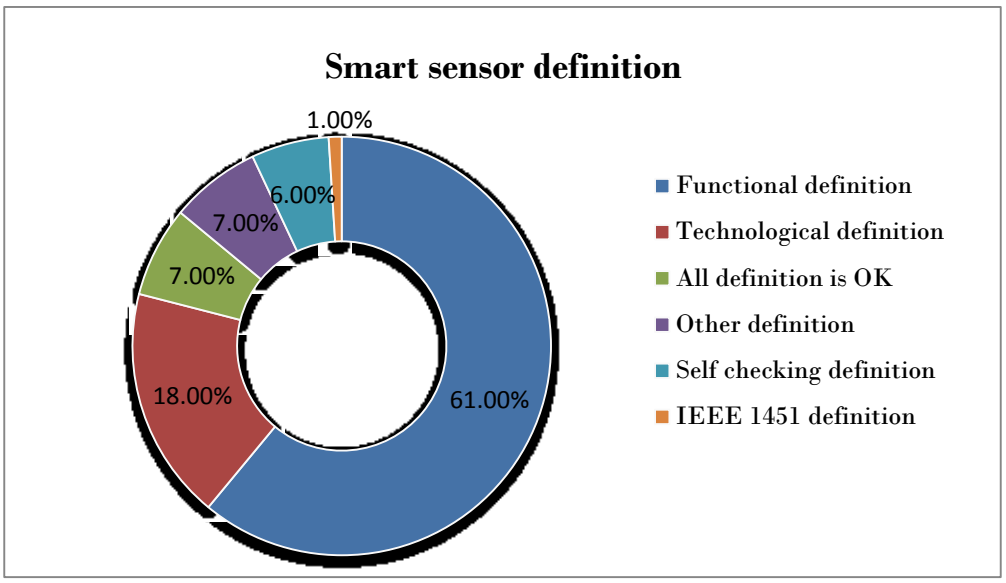

Figure 2-1: Survey results from IFSA 2009 [36].

Recent publications have shown that there are multitude approaches in designing suitable IS framework for MCM and diagnostics. Most of the proposed systems encompass 6 modular stages: data acquisition, signal conditioning, signal analysis, feature computation, data fusion, and decision making. The degree of dependency on human intervention of the intelligence level of sensing system is categorised into 4 levels as tabulated in Table 2-1.

Table 2-1 Categorised intelligent level of sensing system

Level	Signal acquisition	Signal conditioning feature	Signal processing algorithms	Artificial intelligence for classification/	Advanced AI and self-calibration
1	•				
2	•	•	•		
3	•	•	•	•	
4	•	•	•	•	•

•: Available feature

2.2.2.1 Level 1

Level 1 sensor is a basic framework to establish simple communication protocol without having any signal processing and analysis. In other words, there is no 'intelligence' on the sensor itself. For monitoring system with level 1 sensor, raw signals are sent to a central computing hub for further processing [37]–[39]. These systems have low flexibility in power and communication management, but high expandability in managing the whole resources of the RMD. Level 1 sensor does not require embedded microcomputer. Therefore, no software architecture is built on the sensing level.

2.2.2.2 Level 2

Level 2 sensor has computing functionality and device configurations for user's interaction. These include parameters from microcontroller, sensing parameters and anti-aliasing filter, such as: sleep timer, sampling frequency, number of samples, filter specifications and monitoring alarm thresholds. This type of sensor is the initial trend paving the path for decentralised system. Level 2 sensor tends to extract important information from raw signals, and thus reduces excessive data transmission. Signal processing and algorithm are internally implemented to extract important feature components during the monitoring process. For simple monitoring, conventional methods, such as simple threshold methods and statistical methods (root mean square, crest factor, kurtosis) [40] are integrated to diagnose machinery

faults. Such techniques do not require high computational environment. However, they are merely applied to RMD with simple mechanisms and operations. Therefore, the signals have to be transformed and with the frequency domain analysed using fast Fourier transform (FFT) [8]. For non-stationary vibration analysis, more advanced techniques involving time and frequency domain are utilised, such as short-time Fourier transform [14], Wigner-Ville distribution [11] and discrete wavelet transform [41]. Several publications with on-board discrete wavelet transform using microcontroller are discussed in [42], [43]. However, due to the large amount of required memory to store wavelet information, their respective system sent processed wavelet information to computer for further analysis and data logging.

Besides signal processing, conditioning or modulations techniques can be integrated based on the sensing level. Time synchronising averaging is one of the common methods used to improve signal to noise ratio [6]. Generally, a large number of feature parameters are necessary for effective RMD, causing IS to have various solution models in a single hardware unit. Hence, the feature extraction techniques are implemented to reduce the dimensions of feature parameters before sending them to the central node. To test the validity, [44] have studied the principal component analysis (PCA) based technique and have improved the method with the mean correlation statistical approach [45]. A different variation of PCA, known as kernel-PCA has also been used in [46] to select important diagnostic features from vibration, current and flux.

2.2.2.3 Level 3

Previous levels involve data collection and signal analysis. However, they do not make any further evaluation on the calculated components. Level 3 incorporate data fusion layer using AI to perform classification based upon the internal processed results. It is the current trend of development in IS technology. Level 3 sensor has the ability to carry out independent data fusion without communicating with other external computational core. The AI in a condition monitoring system encompasses

a number of technologies: support vector machine [46], fuzzy logic [40], [47] and expert system [48]. One of the examples of Level 3 sensor is revealed in [41], which have proposed a microprocessor-based monitoring system that collects, pre-processes, and analyses vibration signals for fault detection in shafts and bearings, establishing complete intelligent diagnostics system with configurable user-defined parameters. These approaches have specific aims to mimic human experts and solve problems that are difficult to be solved using predetermined algorithms or mathematical models. With limited resources on sensing node, AI techniques have to be technically miniaturised for embedded system applications. Contrary to Level 1 sensor, these systems have high flexibility in power and communication management but low expandability in managing the whole resources of RMD. Likewise, the modularity is usually difficult to be modified due to the complicated sensor's architecture.

2.2.2.4 Level 4

Level 4 sensor is the future trend in RMD. It presents the complete framework of an embedded IS, which is able to establish a full of process of RMD on sensing level itself. To simplify deployment, the IS has adaptive system ability for compensating faulty analysis. For example, computational models are artificial neural network [13] and neuro-fuzzy [25]. In addition, Level 4 bring IS to a whole new era by incorporating self-calibration and fault diagnostics approaches to a single unit.

2.3 Feasibility – Modern maintenance strategy

2.3.1 E-maintenance

Maintenance technologies have been methodically investigated and applied in many industries. Recent publications present numerous technologies and software/hardware system architectures in different directions. Maintenance has also emerged in a new generation of maintenance, namely e-maintenance [49]. It is a

future vision of maintenance concept, which integrates the strategy of modern technology (internet, micro-processor, smart transducer and wireless sensor network) and enterprise management. Researchers believe that, by integrating e-maintenance with e-manufacturing and e-business, it will be a major trend in future industries, which benefits suppliers and consumers from increased equipment and process reliability [49], [50]. Figure 2-2 highlights the integration of e-maintenance with e-manufacturing and e-business.

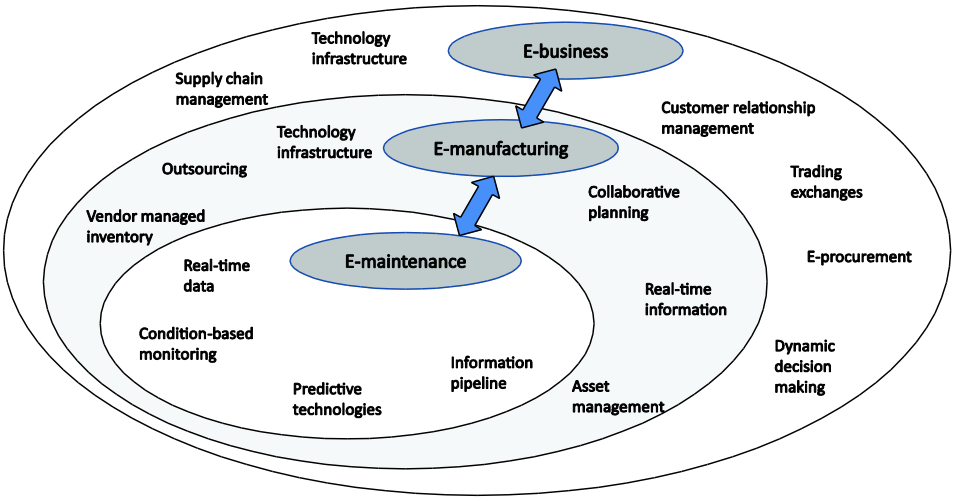

Figure 2-2 Integration of e-maintenance with e-manufacturing and e-business [49]

2.3.2 Standardisation issue

The divergence of maintenance strategies have created a massive number of research questions and ideas highlighting the need for proper standards or an emergence of dominant design is required in order to direct the development for the benefit of both customers and developers. Open system architecture for condition-based maintenance (OSA-CBM) is an open standard to facilitate the technological growth of CBM system [51]. It is becoming more popular in CBM deployment. Its standardisation issues are further discussed in [52] and [53].

2.3.2.1 Open standard architecture for condition-based maintenance

Due to limited flexibility in integrating the CBM system designs from different vendors and developers, OSA-CBM outlines a standardised system framework that aims to:

- improve the communication paradigm between the sensor platform with other maintenance modules;
- explore and identify research questions in current CBM technology;
- increase competency and rapid technology development; and
- reduce costs.

OSA-CBM can be partitioned into seven functional layers, as illustrated in Figure 2-3 [54]. Each layer has the capability of requesting data from any functional layer when needed. Data is usually transmitted between adjacent functional layers; however, it is difficult to transfer data between platforms due to the different formats and information management by various vendors and manufacturers.

In an effort to provide a unified interface for data transmission, OSA-CBM specifies how the data should circulate within the system using eXtensible Mark-up Language (XML). By using the XML schema provided by OSA-CBM, all functional modules compliant with OSA-CBM standard can easily exchange data within the monitoring system.

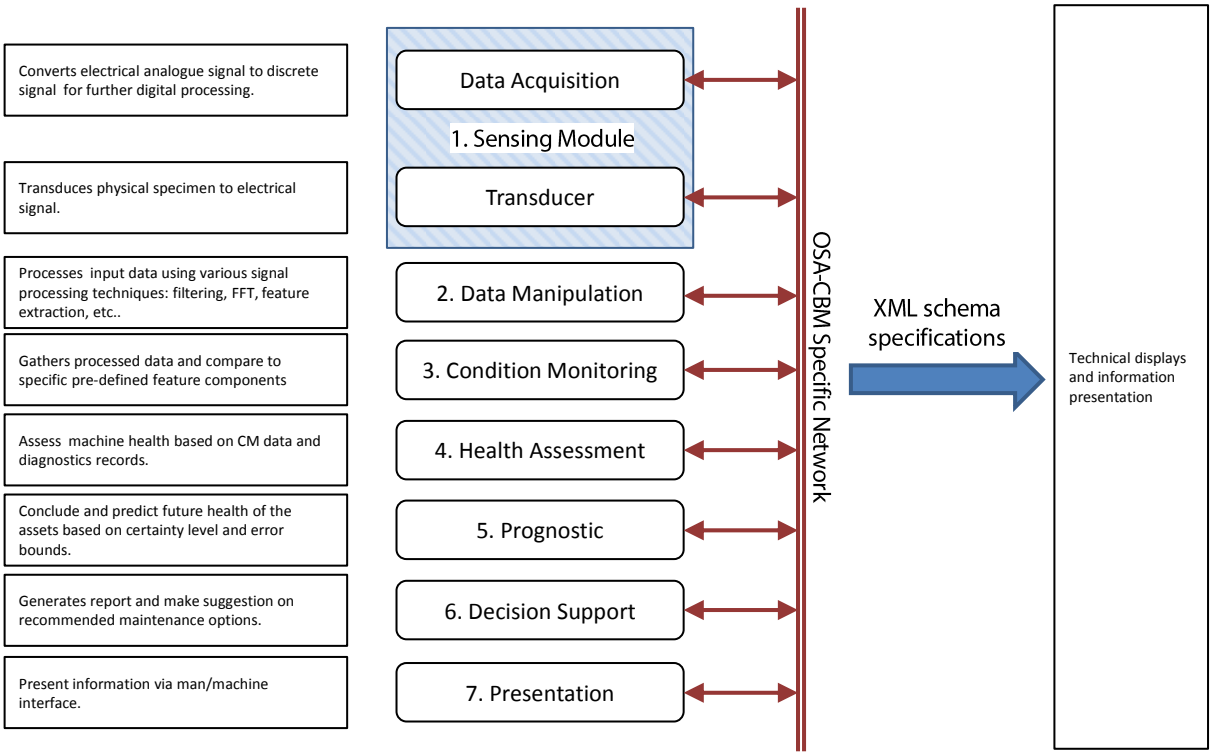

Figure 2-3 Open standard architecture of condition-based maintenance [54]

2.3.3 Defining suitable strategy for the intelligent sensor

The implementation of the IS is the current trend in MCM. Benefitting from the significant growth of microelectronic technology, it is possible to design an intelligent monitoring system for e-maintenance (IMSEM), where its structure is compatible with OSA-CBM, thus providing higher interoperability and adaptability in future deployment. Hence, it reduces redundant implementation requirements by simplifying the information circulation within the whole OSA-CBM architecture, as shown in Figure 2-4. The modular structure of IMSEM has advantages in terms of minimising the size and complexity of internal communication, thus reducing communication workload.

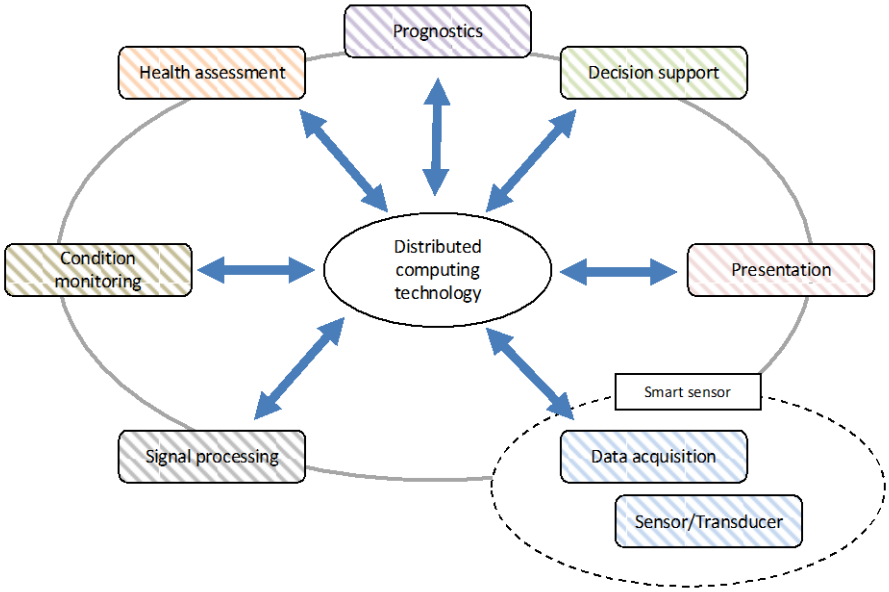

Figure 2-4 shows the data circulation within an open system CBM design. All components are established based upon distributed computing topology

A wireless module, such as XBee, is a promising communication device in terms of establishing a wireless sensor network. It has great benefits in reducing wiring costs, which is one of the critical cost components in CBM installation. Normal XBee configurations communicate in ASCII text representations; therefore, it has a compatible interface module with OSA-CBM. Relevant monitoring information can be transmitted in XML format.

2.4 Sustainability – Power management system

2.4.1 Overview

Power supply is one of the critical factors to sustain the operating time of IS. Reported in [31], the battery energy density has slowest improvement multiples compared with other computer technology development, as shown in Figure 2-5. Hence, Paradiso et al. emphasised that the research direction for power management lies on the efficient power management in sensing nodes, thus reducing required energy volume.

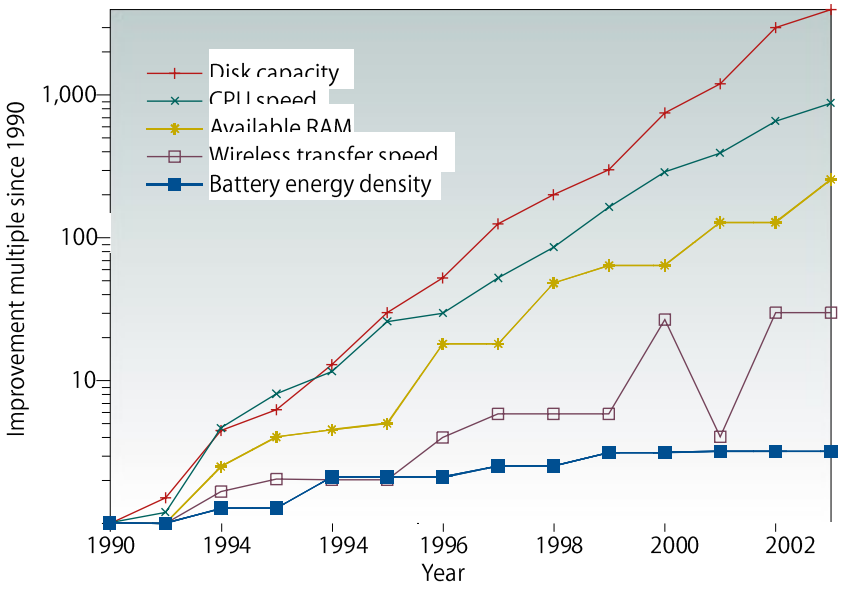

Figure 2-5 Relative improvements in laptop computing technology from 1990–2003 [31]

Various researchers classify energy devices into 3 categories: sources, storage and consumers [33], [55], [56]:

- *Energy sources:* devices that provide or generate energy. Examples include photovoltaic (PV) cell and vibration harvesters.
- *Energy storage:* devices that store energy. Examples include rechargeable batteries and supercapacitors.
- *Energy consumers:* devices that consume energy. Examples include microcontroller and other peripheral sensing modules.

2.4.1.1 Energy sources

Conventional RMD systems are powered by wired power supply. This is the easiest solution to provide electricity to a monitoring device. Wiring is expensive and is not practical for remote sensing unit when installed in complex locations. Traditional batteries have limited efficiency and needs replacement periodically. Battery and energy harvesting modules are preferable for wireless sensing unit to reduce difficult fixing and lay out. Gilbert and Harb et al. have done a concise review

on state-of-the-art of energy harvesting techniques, consisting vibrations, thermal, radio frequency radiation and solar [57], [58]. Recently, industry has growing attention in developing energy harvester to scavenge ambient energy sources, in which their respective performances are tabulated in Table 2-2.

Table 2-2 Power outputs of energy harvesters by different vendors

Ambient energy source	Reference model	Vendor	Normalised power (mW)
Vibration – Piezoelectric	V25w	MIDE [59]	9.231[*1]
Vibration – Electromagnetic	66001[*2]	Perpetuum [60]	27.5
Thermoelectric	MPG-D655	Micropelt [61]	6[*3]
Thermoelectric	–	Applied digital solutions [62]	0.05
RF Radiation	P1110	Powercast [63]	100
Solar	KS10T	SolarTec [64]	10000
Solar	MC-SP0.8-NF-GCS	Multicomp [65]	800

Vibration energy is available in most machinery-built environments. Generally, the utilisable energy can be extracted from a vibration source depends on the amplitude of the vibration and its frequency. There are 3 types of mechanism to induce vibration energy: piezoelectric, electrostatic and electromagnetic. Piezoelectric-typed system generates electric field proportional to strain with piezo electric materials. Electrostatic-typed system converts utilisable energy by introducing a parallel plate of vibration-dependent capacitors. When a mechanical energy is exerted, it separates the charged variable capacitors, thus converting into electrical energy. Electromagnetic-typed system transduced voltage resulting from relative movement between a magnetic and a coil. Recent publications emphasises

[1] Tuned to 40Hz, 15.6 gram tip mass with 1g acceleration
[2] The numbers refer to different model variations
[3] Temperature differences at 10K according to datasheet

on designing an electromagnetic vibration harvester in micro-scaled devices [66], [67]. Among the available commercial products, Perpetuum's vibration harvesters have promising vibration energy harvester unit, which has its rated power output at 27.5mW [60].

Conversion of energy derived from thermal gradients is the basis for many large-scaled power generations (For example: steam turbines). However, its mechanism is not generally scalable to the level required by embedded system [57]. Moreover the power generation of thermoelectric is low in small volume. A commercial company, Applied Digital Solution Corp provides 100µW from a 10K temperature difference with a harvester device, which has physical volume of $100mm^3$ [62].

Radio frequency (RF) radiation is commonly used to scavenge micro-scaled ambient energy to operate ultra-power electronic devices, such as ID card or smart card. A radio frequency harvester consists of receive antenna and equivalent rectifying circuit to convert RF radiation into useful electrical power. This harvesting solution has evident applications if there is a high power RF source nearby the harvesting device [68]. P1110 RF harvester unit by Powercast provides rated power at 100mW with a 50Ω receive antenna for operation in 902 to 928MHz band [63], [69]. However, RF radiation has limited power sources to be scavenged due to surrounding RF interference and safety regulations. Government regulations limits the RF power of 915MHz to 4W effective isotropic radiated power [69]. Moreover, the available power densities of RF emission are relatively low compared with other ambient energy source. Tabulated in [70], Abadal et al. have tabulated the power densities in different applications compared with solar radiation.

Table 2-3 Comparison of power densities for different application with solar radiation [70]

Applications	Power density (mW/cm^2)

Old ultra-high frequency TV band	10^{-9}
FM radio at 50km from 100kW base station	10^{-7}
Industrial, scientific and medical (ISM) radio band: ZigBee	10^{-8}
Bluetooth	10^{-7}
WIFI	10^{-6}
Global system for mobile (GSM) at 10m from base station	10^{-6} to 10^{-4}
Mobile phone at 50m from base station	10^{-4} to 10^{-2}
Wireless power transmission	10^{-1} to 10
Solar radiation in the visible range	10^{2}

Scavenging energy from solar, also known as photovoltaic (PV) cell effect is another common usage of energy harvesting. It is considered the most essential and prerequisite sustainable resource because of the ubiquity, abundance and sustainability of solar radiant energy. There are rich profiles of research and development to implement PV cell virtually and practically [71]–[73]. To simulate PV cell, a mathematical model of solar panel is simulated accurately with respective solar irradiance and ambient temperature [74], [75]. It has relatively constant power generation as in the G24 Innovations Photovoltaic Dye (233mm × 135mm) which produces 3mW with a light level of 500 lux [76].

Among the energy harvesting techniques, PV cell is considered as the mature technology with readily products and solutions. By evaluating the performance of energy harvesting techniques in terms of power generation and physical volume, Gilbert et al. have done a comprehensive survey as shown in Table 2-4. The respective harvesting performance could be evaluated as plotted in Figure 2-6. Perpetuum with vibration harvesting solution provides higher power within the physical volume range within 30000mm^3. However, its harvesting performance solely is dependent on the dominant frequency of the vibration excitation. Hence, further

study and analysis is needed to maximise the performance of vibration harvesting solution.

Table 2-4 Comparison on energy harvesting devices [57]

Device number	Operating mode/ material	Author	Output power (µW)	Frequency (Hz)	Amplitude (ms^{-2})	Normalised power (µW)	Volume (mm^3)
1	Vibration – Piezoelectric	Glynne-Jones [77]	2.1	80.1	2.3	0.5	125
2	Vibration – Piezoelectric	Marzencki et al. [78]	0.6	900	9.81	0.0007	2
3	Vibration – Piezoelectric	Mitcheson et al. [79]	3.7	30	50	0.005	750
4	Vibration – Electrostatic	Despesse [80]	1052	50	8.8	27	1800
5	Vibration – Electrostatic	Despesse [80]	70	50	9.2	1.7	32
6	Vibiration – Electromagnetic	Perpetuum et al. [60]	4000	100	0.4	27500	30000
7	Thermoelectric	Applied digital solutions [62]	–	–	–	50	41

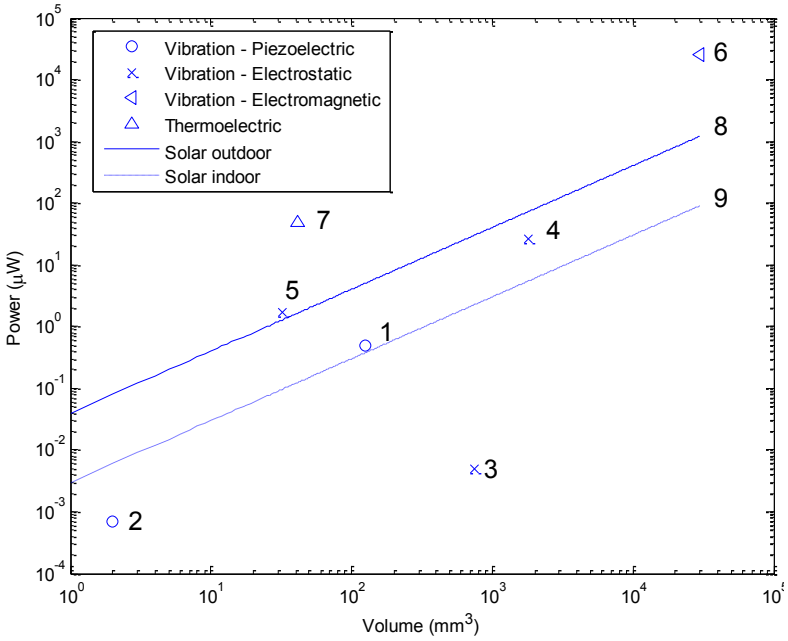

Figure 2-6 Comparison of energy harvesting solutions

Based on the surveys, solar energy harvesting is chosen as primary source for the developed system, reason being that it has mature development status compared with other harvesting solutions. Other ambient energy sources will be considered in the future design, whereby a competent energy harvesting module is envisioned for multiple harvesting roles.

2.4.1.2 Energy storage

The Ragone chart as discussed previously in Figure 1-4 shows various energy storage resources. Recent publications highlighted the attention given to the development of supercapacitor [75], [81], [82]. Reported by [83], the performance of supercapacitor is compared with conventional lead acid battery as tabulated in Table 2-5.

Table 2-5 Battery versus supercapacitor [83]

	Lead acid battery	Supercapacitor
Specific energy density (Wh/kg)	10 to 100	1 to 10
Specific power density (W/kg)	<1000	<10,000
Life cycle	1,000	>500,000
Charge/discharge efficiency	70 to 85%	85 to 98%
Fast charge time	1 to 5 hours	0.3 to 30 seconds
Discharge time	0.3 to 3 hours	0.3 to 30 seconds

Supercapacitor has many advantages over conventional batteries. One important advantage is its operating life cycle, which has longer energy storage for the sensing unit. The mathematical model have been registered and documented, simulated and published in [81], [82], [84]. However, the significant drawback is fast discharge time. Therefore, this has limited the continuous operational time for designated sensor operation.

2.4.1.3 Energy consumers

The main candidates for energy consumers are embedded microcontroller and wireless module. Embedded system-on-chip has relatively low energy consumption compared with conventional monitoring system. The high end micro-controllers (32bit) have promising energy-aware characteristic, which maintain their current draws at full operation mode at around 25mA [27]–[29]. 8-bit microcontrollers have lesser power consumption (5mA to 10mA) but their computational capabilities are limited [85]. Sleep or hibernate features are integrated as handy user modules to provide better power characteristic. For wireless communication module, XBee consumes around 50mA when transmitting or receiving remote signals [86]. In sleep mode, the energy is conserved to 1mA.

Table 2-6 Power consumption data for some monitoring sensors [87]

Sensors	Current consumption			Power consumption (mW)
	Transmission mode (mA)	Reception mode (mA)	Sleep mode (μA)	
IMOTE2 (Crossbow)	33	33	390	127.05
DataBridge wireless I/O modules	37 to 120	37 to 120	<100	116.55 to 378
Apex and Apex LT modules	170	37	5	105.45 to 484.5
Si4420 Universal ISM Band FSK Transceiver	13 to 26	5 to 11	0.3	41.8 to 98
XBee 802.15.4 modules	50	50	10	155

In energy aware features, the power budget for the energy consumer devices must be studied wisely as the ambient energy from a harvesting module is limited. The performance of the sensing unit is proportional to power consumption. Kausar et al. have tabulated the power consumption data for some common monitoring sensors, as shown in Table 2-6.

2.4.2 Photovoltaic energy storage using supercapacitors

Recent publications have emphasised integration of PV cell with supercapacitors. Experimental exercises have demonstrated positive outcomes in designing ISs for RMD systems. Logerais et al. have presented complete system architecture of PV energy storage using supercapacitors through both experimental and simulation approaches [88]. As illustrated in Figure 2-7, their experimental and practical results are identical, proving the sustainable simulation outcome in practical performance estimation. The differences between the experimental results and simulation are shown in [89], which proposed similar energy device architecture for water distribution sensing network. To provide constant voltage level, a buck-boost converter is recommended to be integrated into the circuitry [75], [90].

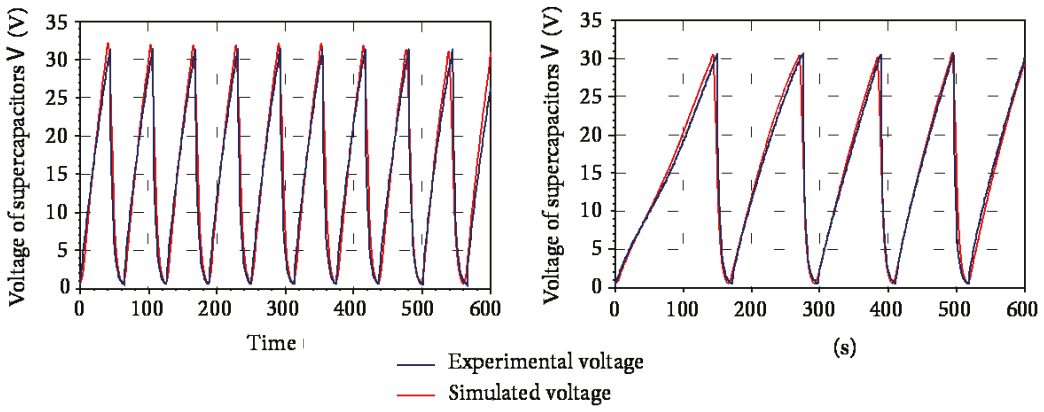

(a) (b)

Figure 2-7 Experimental voltage of the module of supercapacitors confronted to simulated results (with the transmission line capacitance corrected): a) G = 865W/m^2, b) G = 865W/m^2 [88]

2.4.3 Enhanced power management

To efficiently carry out monitoring tasks, the sensing unit shall have the ability to manage the energy budget. It is highly recommended to maintain efficiency while conserving as much energy as possible. Current power management mechanism for wireless sensors typically rely on predicted information on the amount of energy that can be harvested in the future. However, such mechanisms suffer from inevitable prediction errors, which degrade the performance in practical deployment. To

conserve enough energy within the sensor itself, [91] have proposed an energy neutral management mechanism based on sensor's average duty cycle. They analysed the energy budget of power generation and consumption by slotting the sensor's operations into different time slot, as shown in Figure 2-8. By indicating different slot of sensor's operations, the amount of harvested and dissipated energy can be accurately calibrated.

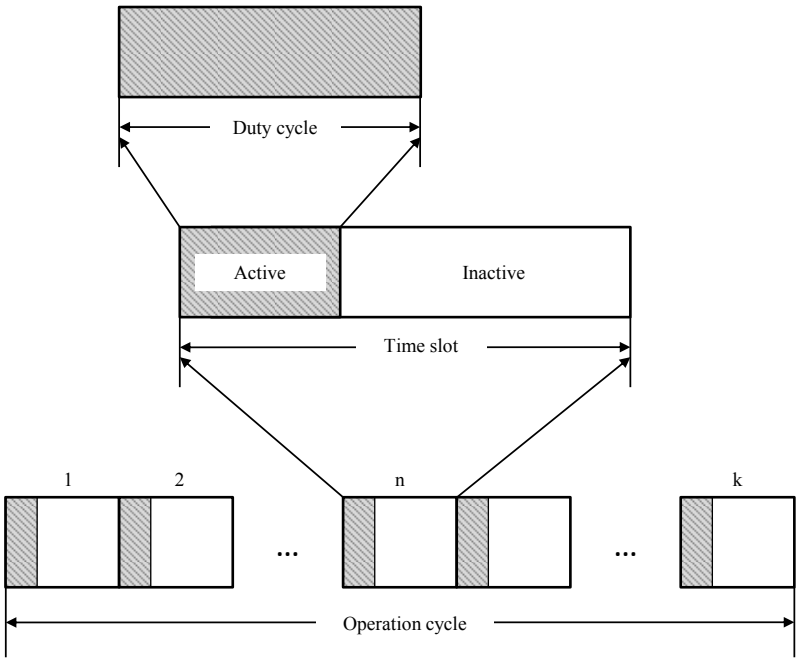

Figure 2-8 Operation cycle with time slots and duty cycles [91]

In practice, Sanchez et al. have also proposed a concise numerical energy harvesting model for sensing unit using PV cell, namely Similar I-V for energy harvesting (SIVEH). In their study, an energy neutral operation (ENO) is analysed at early stage of the design [33]. The ENO is used to determine the power characteristics of the system application suitable for the energy management policies on the sensing platform.

The above studies only cover single deployment of IS. In larger industries, multiple sensing units are required in order to exchange information from one to another, forming a sensing network. To efficiently utilise the energy within the

structure, [55] presented a game-theoretic approach to optimise energy management. The Nash equilibrium, which was initially introduced by John Forbes Nash in [92], is used to find an optimised equilibrium state of sensing network. This theory is latter applied in [93], [94].

2.5 Discussion and synthesis

By reviewing the above mentioned research works, it was noted that there are few publications concerning the integration of RMD technology in embedded system. For sensor functionality, many publications did not discuss the memory limitation and processing speed to carry out signal acquisition and processing [41], [46]. This is very crucial in embedded system as the resource for memory and computational core are strictly limited for performance and power management. On the contrary, there are publications which in fact, have developed a generic embedded AI which has yet to be validated for RMD [95]–[97]. Their extensions of capability are still unknown in MCM and diagnostics. Moreover, despite the embedded AI is predicted to be the future trend of microsystem, few works are carried out to integrate them in low memory console. Many studies on energy harvesting did not clearly address the power consumption characteristics of energy consumer modules [33], [89], [91].

Consequently, this research work will focus on developing a novel hardware and software architecture with the following considerations:

- Limited processing memory down to microsystem level (256kB to 512kB respective to different types of microcontroller).
- Enhanced software architecture, numerical algorithm and intelligent data fusion layer for MCU to assist RMD operations.
- Concise study on power characteristics which is suitable for the integration of power harvesting module.

2.6 Summary

In this chapter, literature review on designing an energy aware sensing unit for RMD system is presented. Three major fields concerning sensor's functionality, feasibility and sustainability are studied. The current status of the deployment of intelligent sensing unit is investigated. The next chapter shall cover the selection of suitable technology and novel sensor framework to carry out advanced monitoring tasks on rotating machinery.

Chapter 3

Generic hardware framework of intelligent sensor

This chapter presents the hardware architecture of the developed intelligent sensing system. The system design have been discussed and examined. The rationale and motivation of the system design is based on research review and synthesis. At the end of this Chapter 3, a summarised specification of the developed sensor is presented.

3.1 Overview

Chapter 2 has outlined the current research and development status of designing an IS for MCM, which is defined as IMSEM in section 1.3.4. In order to validate the feasibility of the project, it is necessary to develop a hardware system that fulfils the specifications of an envisioned IS system. The focus of this chapter is to discuss the rationale and motivation for the selected unit components. A proof-of-concept prototype is also presented at the end of the chapter.

The hardware architecture of IMSEM, as depicted in Figure 3-1, is partitioned into 5 submodules: sensing module, peripheral computational core unit, main processing unit, data storage module and wireless communication interface. Cost and performance characteristics of hardware components are two main design criterions.

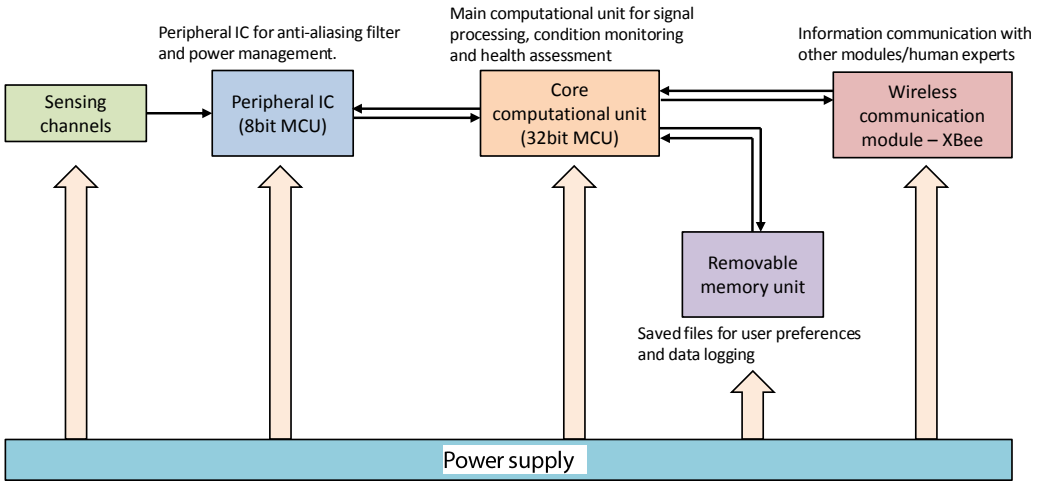

Figure 3-1 Hardware architecture of IMSEM

The sensing channels are responsible transduce physical form into electronic signals. The resulting electronic measurements are then sent to the peripheral computational unit where necessary analogue signal conditioning is carried out. The processed analogue signals are then transmitted to core computational core for signal processing, analysis and fault diagnostics. The quantised data is logged and

interrogated in removable data storage device (universal serial bus (USB) flash drive or secure digital (SD) card) through data storage module. End-result and diagnosis report is transmitted to another system platform through wireless communication module. The wireless communication module is vital to reduce cost and maintenance required for wiring installation. A respective workflow of IMSEM is illustrated in Figure 3-2.

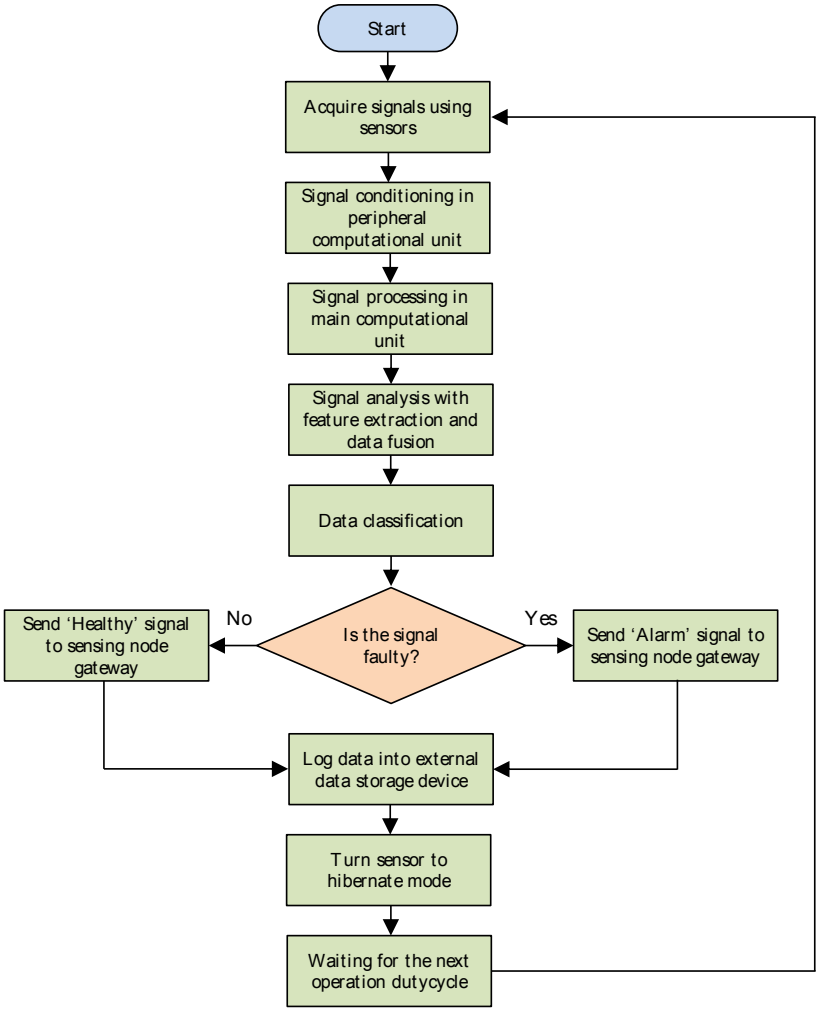

Figure 3-2 Workflow of IMSEM

An operational prototype is developed by the use of 2-layer circuit board as means of integrating the individual hardware components selected into a compact and cohesive unit. IMSEM's hardware modules are integrated on the target circuit

board for better packaging and presentation. The circuit board reserves several pins and channel for future hardware extension, providing a better modularity to integrate with new system design in the future. An external energy harvesting module is designed to serve as an extended system module to IMSEM. Its system architecture will be further discussed in Chapter 5.

Table 3-1 outlines the design criteria for the developed system. The selection criteria describe the essential functions of each module. Suitable microelectronic technology is selected to realise the developed prototype to meet the design parameters of the system. Finally, it should be noted that, except in the case of the tailored printed circuit board, the use of readily available off-the-shelf components is sought during the design process to keep fabrication efforts reasonable to maintain total unit cost low by selecting from the best embedded system technologies. The proof-of-concept prototype wireless sensing unit represents only a first step in an iterative design process that will inevitably evolve in time to keep pace with newer hardware technologies and future application requirements.

Table 3-1 Primary design criteria for designing IMSEM

Design parameter	Selection criteria
Peripheral computational unit	
Main task	Anti-aliasing, power management and peripheral processing tasks
Processor	Low-power 8-bit MCU
Power characteristic	Continuous type. Less power consumption when in sleep/hibernate to maintain minimal wake up function
Main computational unit	
Main task	Signal processing, analysis and fault diagnostics
Sensing channel	Multiple sensing channel (Analogue and digital)
Sampling frequency	Minimum 5kHz for simultaneous sampling
Power characteristic	Burst type. Minimal power consumption at sleep/hibernate mode

Data storage module	
Main task	Easy interface to save data into mass storage device
Writing/reading speed	Able to save/load data without delaying the system's operation
Power characteristic	Burst type. Minimal power consumption at sleep/hibernate mode
Wireless communication	
Interface	Direct communication interface with MCU recommended.
Open door range	More than 50m
Power characteristic	Burst type. Avoid idle mode to conserve power consumption

In the following sections, the hardware design of each sub-module is discussed in greater detail.

3.2 Sensing unit

3.2.1 Selecting suitable sensor

As discussed in Chapter 2, vibration monitoring is the most established monitoring techniques for rotating machines. It has the ability to detect several faults by analysing the vibration signal (shaft misalignment, rotating imbalance, faulty bearing and gearbox, etc.) [8], [41], [50], [98].

To effectively carry effective RMD task, rotating speed is another important parameter to be measured. For rotary machines, the vibration signals sometimes have similar characteristics between healthy and faulty datasets. Table 3-2 shows two sets of acquired vibration data with different rotor unbalance and rotating speeds. Their corresponding feature components are calculated to evaluate their component similarity. Note that even rotating under different rotating speed, both vibration data have low differences in several feature components: Mean standard deviation and peak. Such differences cause difficulty to classify condition monitoring

in data fusion layer with only vibration data. Hence, additional dimension with accurate rotational speed information is required to carry out RMD task, which will be further discussed in Chapter 6.

Table 3-2 Comparison of feature components of two vibration signals

Dataset	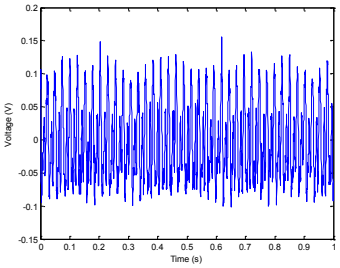	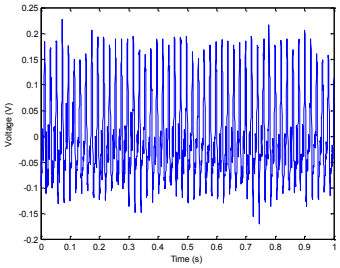
Rotating speed (rpm)	2564	2864
Rotor unbalance residual (g·mm)	65	32
Normalised mean	0.7927	0.7433
Normalised rms	0.2801	0.2664
Normalised standard deviation	0.3192	0.3157
Normalised kurtosis	0.0269	0.0001201
Normalised FFT peak	0.4881	0.3904

Besides the selection of measurement types, it is important to ensure that the sensing device to have suitable voltage measurement span for embedded system. For most commercially available MCU, the input analogue range is between 0V to 3.3V or 5V. To consider power consumption and physical size of IMSEM, it is suggested that the chosen sensor has to be power efficient.

Conventional system uses piezoelectric accelerometer to measure vibration signals. Such sensors have already been well established more than 20 years [99].

However, their production cost is high and critically affect their implementation in embedded system, especially if multiple channels are required for monitoring.

MEMS accelerometers are preferred to replace conventional accelerometer, due to their much lower cost and promising performance as verified in recent publication [24], [100], [101]. It has proven durability and ability to survive in high shock level and temperatures in harsh environments [26]. The noise characteristics of MEMS accelerometer (pink noise and white Gaussian noise) is also measured and taken into consideration to ensure better accuracy [102].

There are various techniques available to measure rotating speed. Common approaches include the measurement of infrared radiance, Hall-effect and capacitance to determine the angular position of a physical rotary checkpoint. By differentiating the angular position with time being taken, the angular velocity could be determined. The same procedure can be repeated to obtain acceleration. Therefore, speed measurement has enabled a wide range of sensor selection. In this research work, the developed IMSEM is tested based on 2 testbed: DC motor and 3-phase general induction motor. The effort to transduce angular position in short time interval is omitted as they do not have abrupt change during operation. Hence, commercially available rotary encoder (which comprises off-the-shelf proximity electronic switched to give rotating information) is filtered out from the selection list, as they have relatively high cost (ranging from £2 to £50) and high rated current (average 0.15A) [103], [104].

Proximity infrared, capacitance and Hall-effect sensors are 3 main candidates of desired transducers. Aiming to provide a single angular position in one rotating cycle, the required electronic circuitry is cheap and easy to build. Based on the available testbeds, Hall-effect sensor is chosen as the rotating speed measurand due to its proportional relation to magnetic field, causing it to be easily attached to the motor for experimental testing. Proximity infrared sensor requires physical modification of the tested whereas capacitance sensor is easily disturbed by other approaching

physical object. The simple design of digital Hall-effect sensor is discussed in the latter subsection.

3.2.2 MEMS accelerometer

To comprise cost and efficiency, MEMS accelerometer is used as the main electrical transducer in the system. Several MEMS sensors are examined in the laboratory (ADXL001-70, ADXL202AE and ADXL210). Their performance have been experimentally tested and evaluated, as reported by Albarbar et al. [100]. For MCM applications, ADXL001 is chosen due to its satisfactory performance and good agreement with reference conventional accelerometer. Manufactured by Analog Devices, ADXL001-70 is one of the most suitable MEMS for vibration monitoring. With the effective frequency band up to 22kHz, it theoretically enables to retrieve wide range of signal with unity gain. ADXL001 series MEMS is robust to areas and application with high amounts of electromagnetic interference, which is a common situation in rotating machinery [105].

ADXL001-70 is selected as a MEMS accelerometer for IMSEM. Working at 3.3V/5V operation, it has low power consumption and low noise (typical 2.5mA and 4mg/$\sqrt{\text{Hz}}$). The specifications for ADXL001-70 are tabulated in Table 3-3.

Table 3-3 Specifications of ADXL001-70 at 5V operation [105]

Parameters	ADXL001-70
Approx. Price	£40
Sensitivity (mV/g)	24.2
Measurement range (g)	-70 – 70
Offset voltage at 0g(V)	2.5
Resonance linear band (Hz)	22kHz
Power consumption	2.5mA typical

3.2.3 Hall-effect sensor

The Hall-effect sensor is able to work at 5V operation. In this research work, a normal Hall-effect switch is built upon with simple electronic RC circuit for angular speed measurement, which is illustrated in Figure 3-3. A micropower Hall-effect switch, A3213 by Allergo Microsystems has operating voltage between 2.4V to 5.5V and average current draw at 0.3mA. Other technical specifications are tabulated as shown in Table 3-4. It should be noted that, the period interval of A3213 is 240µs, which produces 4167 pulses in 1 second (4.167kHz). Such frequency is sufficient to indicate the rotary speed of rotating machines in the laboratory (maximum rotating speed at 48Hz).

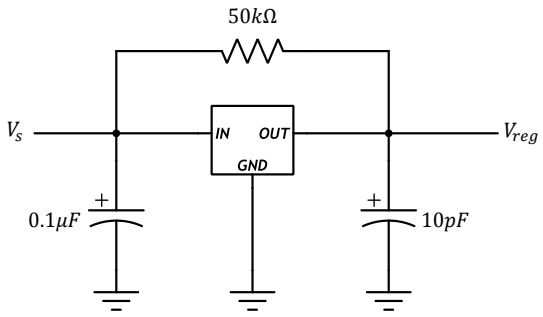

Figure 3-3 Schematic of Hall-effect switch, A3213 (Photos required)

Table 3-4 Rated specifications of A3213 Hall-effect sensor [106]

Parameters	ADXL001-70
Approx. Price	£1.60
Supply voltage (V)	2.4 – 5.5
Activation time (µs)	60
Pulse period (µs)	240
Duty cycle (%)	25
Average supply current (µA)	309

To effectively detect the magnetic object, a piece of magnetic cylinder is attached at the rotating disc of motor testbed, as shown in Figure 3-4. This serves as angular position checkpoints for speed detection. The sensing interface is a single digital

pulse wave that directly connected to the core computation unit. The simultaneous sampling frequency from 4 sensing channels is 10kHz (Will be further discussed in section 3.4.2). These have established a robust sampling environment of digital samples from A3213 Hall-effect sensor, which gives out digital pulse at 4.167kHz. The developed Hall-effect sensor module is put into experimental test. By comparing its speed detection with calibrated speed controller of DC motor. Figure 3-5 shows the digital pulse wave generated from Hall-effect sensor at different rotating speed: 280rpm, 914rpm, 1602rpm, 2281rpm and 2864rpm respectively.

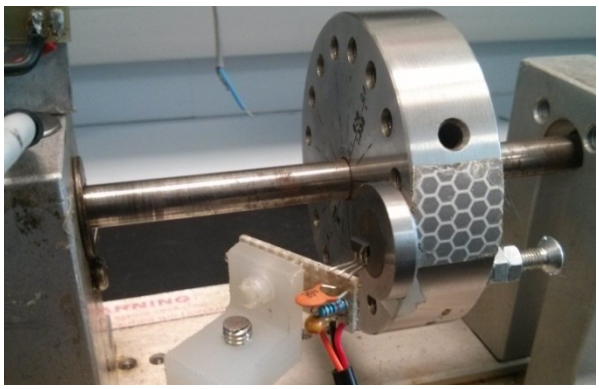

Figure 3-4 Magnetic part attached on rotating machinery testbed

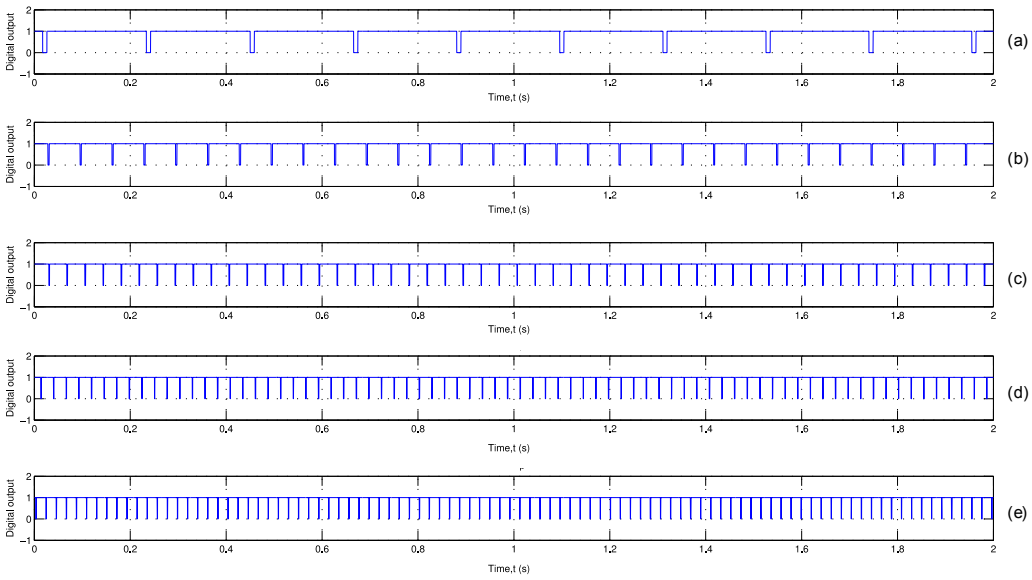

Figure 3-5 Digital pulse wave generated from Hall-effect sensor, A3213: a) 280rpm, b) 914rpm, c) 1602rpm, d) 2281rpm, e) 2864rpm.

3.3 8-bit microcontroller – Peripheral computational unit

3.3.1 Cypress CY8C29466-24PXI – Overview and rationale

In this research work, a programmable system-on-chip (PSoC), CY8C29466-24PXI is chosen as the main peripheral IC for signal conditioning and power management. Designed by Cypress under the category of PSoC1, this MCU integrates configurable analogue and digital peripheral function in a single chip, which is the suitable choice to design both hardware and software embedded system. The physical layout and pin assignment of CY8C29466-24PXI is depicted in Figure 3-6. The specifications are listed in Table 3-5 [107].

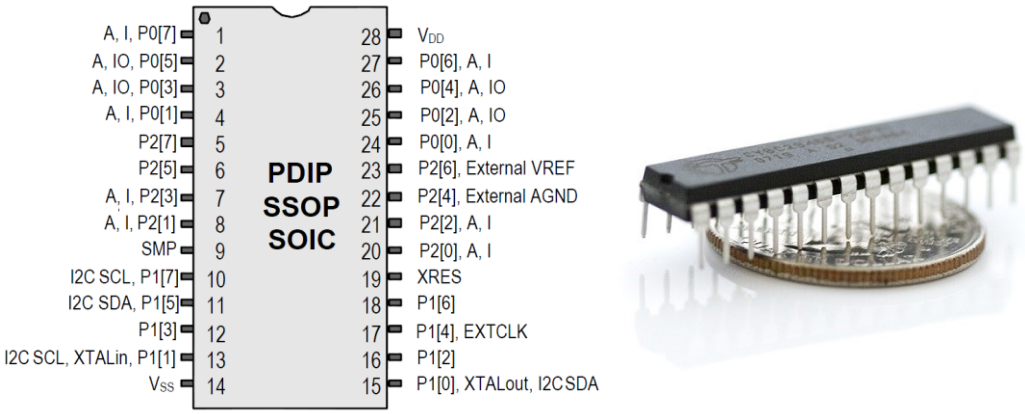

Figure 3-6 Physical layout and pin assignment of CY8C29466-24PXI

One major advantage of PSoC1 MCU is its analogue user module which is able to design an analogue programmable filter within a single MCU. This feature is much beneficial to integrate programmable analogue anti-aliasing filter into system design. In conventional embedded system, digital anti-aliasing filter is widely used to reduce additional hardware component, as many MCU do not have programmable analogue modules. Digital filter is easy to implement into the processor but, it requires high performance ADC and sampling algorithm, which increases the computation load. Analogue filter does not require ADC and digital signal processing

but, in conventional system design, it can only be built with additional component units, such as operational amplifier and RC circuits. PSoC1 has suitable niche to provide the integration of analogue filter with programmable digital user modules, becoming the first candidate to be used in the design.

PSoC Designer, the IDE for PSoC1 MCU has provided a user-friendly tool to manage the MCU resource. This IDE is available for free which could be easily downloaded from Cypress's official website. Moreover, the programmer for PSoC is available online with a free ImageCraft C compiler [108]. These have significantly reduced the development time and cost of peripheral IC for IMSEM.

Table 3-5 Specifications of MCU CY8C29466–24PXI [107]

Specification	Parameter
MCU Core	
Maximum CPU speed	24MHz
Flash ROM	32kB
SRAM	2kB
Analogue module	
Analogue-digital converter (ADC)	4 × 14-bit Delta Sigma / SAR
Digital-analogue converter	4 × 9 bit resolution
Analogue switched capacitor filter	Max 8-poles Band-pass / Low-pass / Notch
Programmable gain amplifier (PGA)	4 units
Digital module	
Universal Digital Blocks (I2C, UART, PWM, gate logics)	4 units
Input/output	
GPIO	24 units
Analogue inputs	12 units
Analogue outputs	4 units
General specifications	
Approx. price (IC only)	£7
Operating voltage	3.3V to 5V
Rated current	25mA

Minimum current at sleep mode	4µA

3.3.2 Programmable analogue anti-aliasing filter

To satisfy sampling theorem, the frequency components of sampled signal must not exceed one-half of the sampling frequency. A peripheral mixed signal microcontroller with programmable continuous low-pass filter is used in designing IMSEM. The programmable analogue filter of PSoC1 uses switched capacitor technology to alternate the impedance of the circuitry. Its respective circuitry is illustrated as shown in Figure 3-7. It works by continuously moving electrical charges in and out of capacitors by toggling the switches with respective switching frequency, f_{clk}. The relationship of capacitor, switching frequency and resistance is expressed in (3-1).

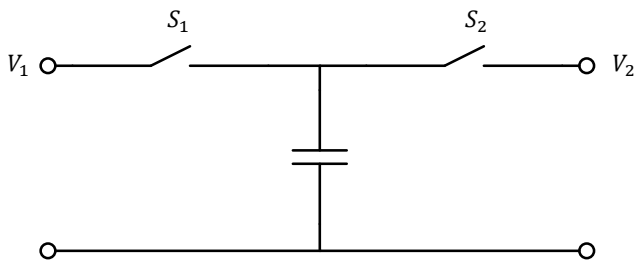

Figure 3-7 Simple switched capacitor circuit

The relationship of capacitor, switching frequency and resistance is expressed as shown:

$$\frac{V_2 - V_1}{I} = \frac{1}{C f_{clk}} = R \tag{3-1}$$

where resistance R is generated with particulate exerted frequency to the toggling switches. V_1 and V_2 are the input and output voltage of the switch capacitor circuit respectively. I is the current that flows through V_1 and V_2. C is the capacitance value of switched capacitor. R is the resistance value generated from the behaviour of switched capacitor circuit,

Up-to-date, switched capacitor has wide range of applications due to its simplicity and variability. National Semiconductor's LMF100 is one of the ICs which uses switched capacitor as programmable filter [109]. However, commercially it usually requires high voltage and external clock frequency for f_{clk}, which draws current and redundant pin for operations. Furthermore, their interfaces are difficult to communicate with computational core unit.

Currently, a 2-pole low pass filter (LPF) is used in the design. PSoC Designer has included off-the-shelf user module. This module implements a general purpose 2nd order state variable low-pass filter with different filter configurations (Butterworth, Bessel, Chebyshev), as shown in Figure 3-8. The switching frequency, $\emptyset_1$ and $\emptyset_2$ invert with each other, establishing toggling affect to the system. Their frequency is equivalent to f_{clk}.

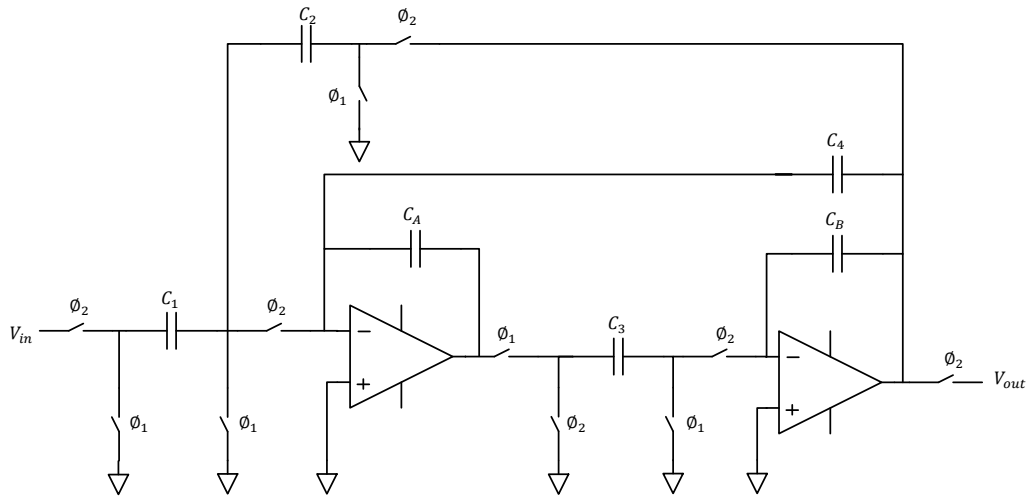

Figure 3-8 2nd order state variable low-pass filter in PSoC 1

Stated in the PSoC 1 datasheet [110], the transfer function of the LPF is expressed in (3-2)

$$\frac{V_{out}}{V_{in}} = \frac{-\frac{C_1}{C_2}\frac{\left(1-\left(\frac{s}{2f_{clk}}\right)^2\right){f_{clk}}^2}{\left(\frac{C_A C_B}{C_2 C_3}\frac{1}{4}\frac{1C_4}{2C_2}\right)}}{s^2 + \frac{C_4}{C_2}\frac{sf_{clk}}{\left(\frac{C_A C_B}{C_2 C_3}\frac{1}{4}\frac{C_1}{2C_2}\right)} + \frac{{f_{clk}}^2}{\left(\frac{C_A C_B}{C_2 C_3}\frac{1}{4}\frac{C_4}{2C_2}\right)}} \qquad (3\text{-}2)$$

where its gain, G, corner frequency, ω_c and damping ratio, ζ are derived as shown:

$$G = \frac{C_1}{C_2} \tag{3-3}$$

$$\omega_c = \frac{f_{clk}\sqrt{C_2 C_3}}{\sqrt{\left(C_A C_B - \frac{C_2 C_3}{4} - \frac{C_4 C_3}{2}\right)}} \tag{3-4}$$

$$\zeta = \frac{C_4\sqrt{\frac{C_3}{C_2}}}{\sqrt{\left(C_A C_B - \frac{C_2 C_3}{4} - \frac{C_4 C_3}{2}\right)}} \tag{3-5}$$

where $S = \{C_A, C_{B,} C_1, C_2, C_3, C_4\}$

Using the wizard provided in PSoC Designer, the capacitance values in set S could be automatically computed assigning the desired G and ω_c of the system. For the corner frequency for sampling frequencies of 2.5kHz, 5kHz, 10kHz and 20kHz, the values in set S are generated, as tabulated in Table 3-6.

Table 3-6 Capacitance values for anti-aliasing filter

Sampling frequency, f_s (Hz)	2.5k	5k	10k	20k
Corner frequency, $f_c = \frac{\omega_c}{2\pi}$ (Hz)	1.25k	2.5k	5k	10k
C_A	1	3	6	14
C_B	1	3	6	14
C_1	5	8	13	15
C_2	19	26	27	29
C_3	32	32	32	32
C_4	32	32	32	32

3.3.3 Power management module

CY8C29466-24PXI has rated current draw at 25mA, resulting an average power consumption of 125mW at 5V operation. Such power is hungry for an energy aware characteristics and it should be suppressed to minimum power level. To efficiently reduce the overall power of IMSEM, CY8C29466-24PXI serves as an internal power

manager to oversee the power rails of other components unit of IMSEM. There are 4 power rails to be considered, each of them is connected to the sensor module through electronic transistor switches. Figure 3-9 shows a simple illustration on how CY8C29466-24PXI manages the power consumption with other modules using transistor bank. A series of power transistor is used as an electronic switch to toggle power transmission from regulated voltage supply. The transistor bank gives 4 power outputs to respective IMSEM module: sensing module (V_{s_sensor}), wireless communication interface (V_{s_XBee}), data storage module (V_{s_ALFAT}) and main computational unit (V_{s_main}).

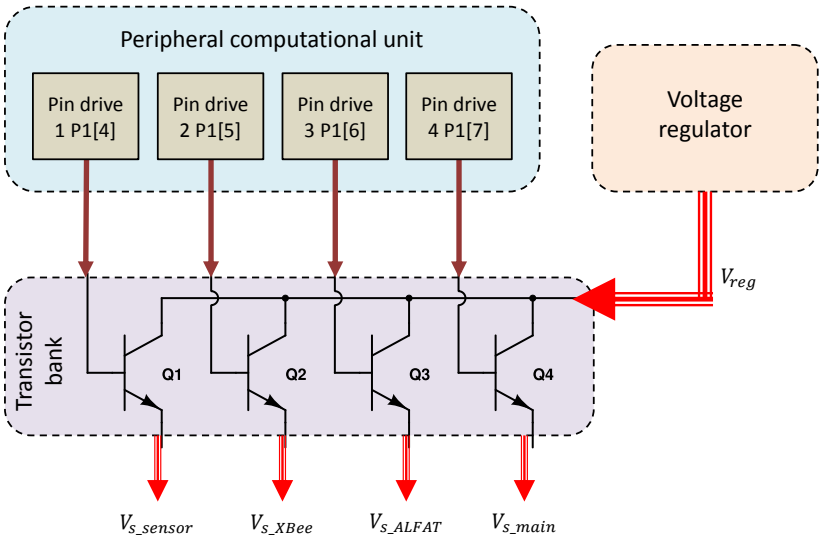

Figure 3-9 Connection of GPIO pins of CY8C29466-24PXI to transistor bank for power line management of IMSEM module

For internal power conservation purpose, CY8C29466-24PXI provides a configurable sleep mode with interrupt service routine. The interruption is important as a flag to wake-up the MCU so that it can continue its operation. There are several interrupted sources available to wake up from sleep mode: sleep timer, general purpose input output (GPIO), low voltage monitor, analogue user modules and internal low-speed oscillator. Published in an official application note, [111] has also outlined additional power configuration to turn the MCU to the lowest power

consumption. It has to be done manually by overwriting the C programming code to the MCU through provided IDE, PSoC Designer.

Due to the desired low-power sensing specified in design criterion, the IMSEM aim to carry out periodic RMD with time-driven characteristics. In this case, it is possible to modify all CY8C29466-24PXI internal resources to its minimum power level during sleep mode. During sleep mode, only one interrupt service routine is enabled: sleep timer interrupt to wake up the signal. Based on the experimental setup, the MCU has successfully put into sleep mode with the constant current draw at 4.68µA. However, the internal low-speed oscillator of CY8C29466-24PXI does not provide a very accurate sleep timing, which has 15% deviation from predetermined time interval (The system wakes after 13s with designated 15s sleep time interval). Hence, an external 32.768kHz crystal is necessary to ensure accurate sleep timer to wake up the MCU. The finalised hardware schematic design will be discussed in section 3.7.

Table 3-7 Current draw of PSoC1 MCU at different modes [111]

Mode	Current draw (mA)
Normal operation	21.7
Sleep – No sleep mode modifiers	12.9
Sleep – Only analogue references off	3.3
Sleep – Only analogue buffers off	12.5
Sleep – Only continuous time and switch capacitor blocks off	13.2
Sleep – Only different pin modes off	9.8
Sleep – All sleep mode modifiers	0.004

3.3.4 Interfacing with main computational core

The connection with main computational core unit is shown in Figure 3-10. For sensing module, two analogue channels are connected to main computational unit through peripheral computational unit (CY8C29466-24PXI), undergoing signal

conditioning process. Since there is no condition for conditioning digital measurement, two digital channels are directly connected to digital inputs of main computational unit. Eight GPIO pins are used as reading/writing information between MCUs. One of the most important usages of GPIO is to read user parameters from data storage module when in initialisation stage.

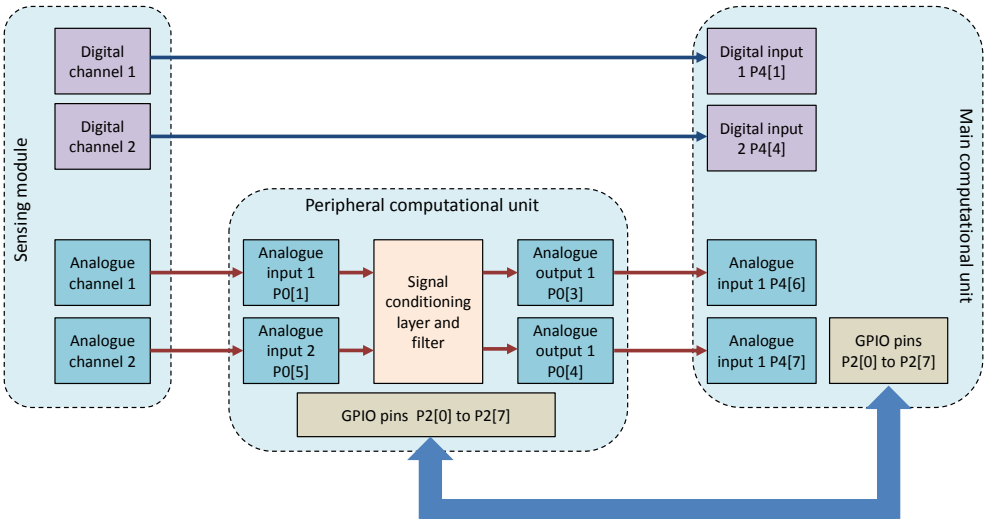

Figure 3-10 Hardware connection of peripheral computational unit (CY8C29466-24PXI) with main computational unit (CY8C5868AXI-LP032)

3.4 32-bit microcontroller – Main computational unit

3.4.1 Cypress CY8C5868AXI-LP032 – Overview and rationale

Main computational unit functions as the "brain" of IMSEM. It carries out signal calculation and makes decision based upon the accumulated signals. As illustrated in Figure 3-1, main computational unit has master interface with two other system modules: data storage and wireless communication modules. They exchange data and information using standardised embedded system interface.

In this research work, PSoC CY8C5868AXI-LP032 is used as a main computational unit for IMSEM. It is a PSoC5 series MCU designed and developed by Cypress. Similar with other 32-bit MCU, CY8C5868AXI-LP032 has relatively

large internal flash memory and static random access memory (SRAM). It has built-in floating point library and digital signal processing (DSP) processing architecture suitable for RMD purpose. The rationale of CY8C5868AXI-LP032 selection is outlined as shown:

- User-friendly IDE software: PSoC Creator, the IDE designed for PSoC5 MCU comprises neat user interface and off-the-shelf user module blocks. All these have enabled easier software integration into CY8C5868AXI-LP032.
- Cypress has integrated highly accurate ADC module in PSoC5, this has increased the system robustness and interoperability in actual RMD testing. Moreover, CY8C5868AXI-LP032 has four additional analogue blocks which are very useful in designing a synchronous sampling with multiple sensing channels. Its rationale is further discussed in section 3.4.2.
- CY8C5868AXI-LP032 can be compiled and programmed with C. It is a common programming language with rich amount of external library for digital signal processing and intelligent algorithms. Fast fourier transform (FFT) is written and its fundamental application in C is concisely discussed by [112]. The C library for intelligent algorithms such as fuzzy logic and support vector machine are widely available on the internet [96], [97]. PSoC Creator includes a GNU-license based C compiler, namely GCC compiler. It is a free compiler for C and its code optimisation is sufficient for this research project.

The physical layout and pin assignments of CY8C5868AXI-LP032 is depicted in Figure 3-11. Its respective specifications are tabulated in Table 3-8.

Table 3-8 Specifications of MCU CY8C5868AXI–LP032 [113, p. 5]

Specification	Parameter
MCU Core	
Maximum CPU speed	67MHz

Flash ROM	256kB + 32kB for error correcting code
SRAM	64kB
EEPROM	2kB
Analogue module	
8-20-bit Delta sigma ADC	1 unit
8-12-bit SAR ADC	2 units
8-bit digital-analogue converter	4 units
Programmable analogue module (PGA, TIA, Sample and hold, etc.)	4 units
Digital module	
16-bit timer, counter and PWM blocks	4 units
Universal Digital Blocks (I2C, UART, PWM, gate logics)	24 units
Input/output	
GPIO	62 pins
General specifications	
Approx. price (IC only)	£11.50
Operating voltage	1.7V to 5V
Rated current at 48MHz	15.4mA
Minimum current at sleep mode	2µA

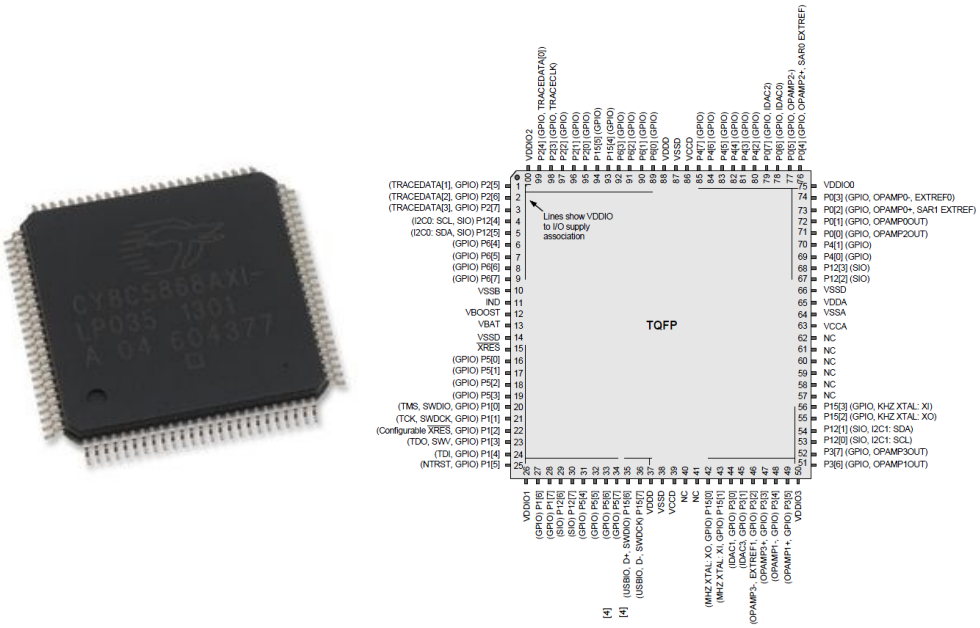

Figure 3-11 Physical layout and pin assignments of CY8C5868AXI-LP032

3.4.2 Synchronous sampling of multiple sensing channels

The IMSEM is designed to have two analogue channels and two digital channels for signal acquisition. Two analogue channels are used acquired signals from two transduced signals from accelerometer, aiming for 2-axis measurement or accelerometer's performance evaluation purpose. The digital signals are used to coordinate the vibration signals at different time interval. It is important to align the vibration data points with the angular position detected using Hall-effect sensor. Figure 3-12 shows a desired signal acquisition behaviour using multiple sensing channels. When the digital signal goes down, it indicates the magnetic object is approaching the Hall-effect sensor. This indicates the exact checkpoint of the rotating machine. The vibration data-points at the time instance could be accurately determined. In Figure 3-12, it is obvious to notice that the vibration data with 7 complete rotating cycles.

The difficulty of multiple sampling of MCU is mainly caused by the limited user ADC module available for analogue-digital conversion. Secondly, the limited SRAM of MCU set a narrow boundary of total points being digitally quantised. Despite the multiple ADC modules are available in some MCU, they cannot fully operate when other analogue module resources are utilised. It is found that with other integration of analogue resources in CY8C5868AXI-LP035 (For example: sample and hold module and analogue multiplexer module), only maximum 2 ADC modules could be used simultaneously. Moreover, the configuration with multiple ADC is not performance-efficient as the propagation delay between two ADC blocks might occur when transmitting the quantised data into SRAM. Inspired by [114], the multiple sensing channels can be realised by integrating additional 2 analogue sample and hold module which their tracking period is identified with a pulse-width-modulation (PWM) module block. Its respective functional block diagram is shown in Figure 3-13.

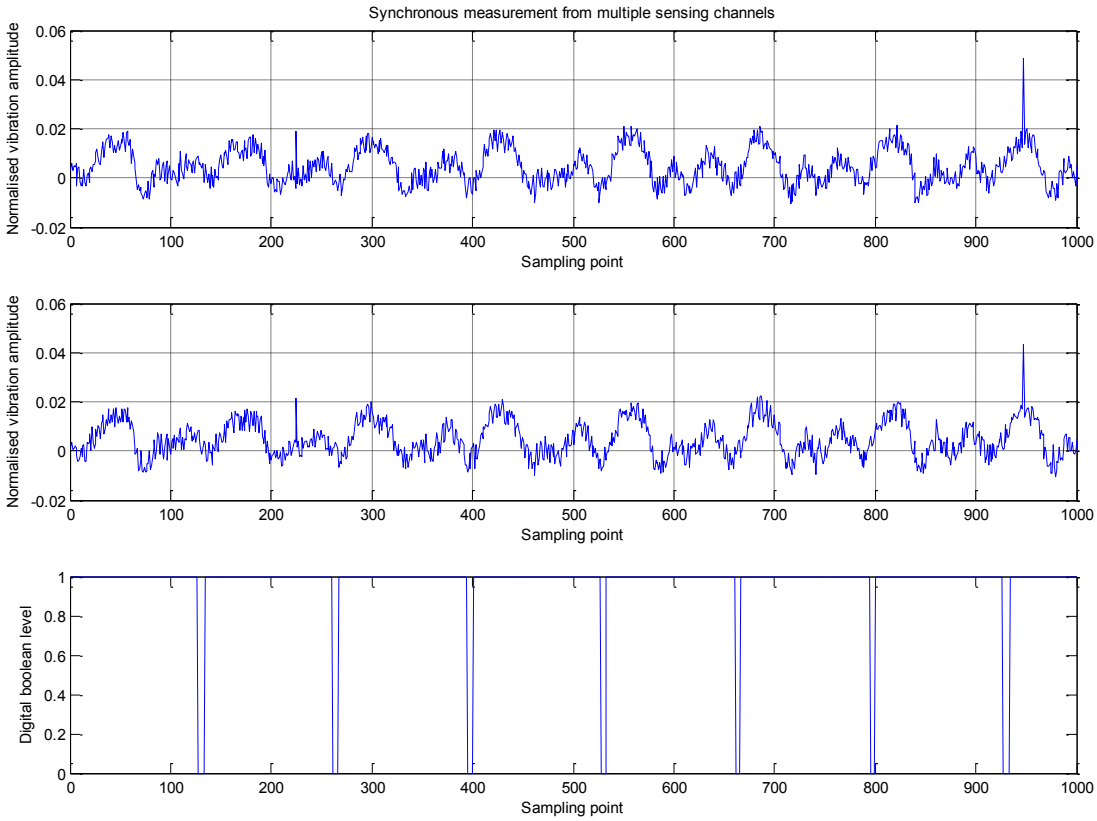

Figure 3-12 Signals waveform from 2 analogue channels and 1 digital channels

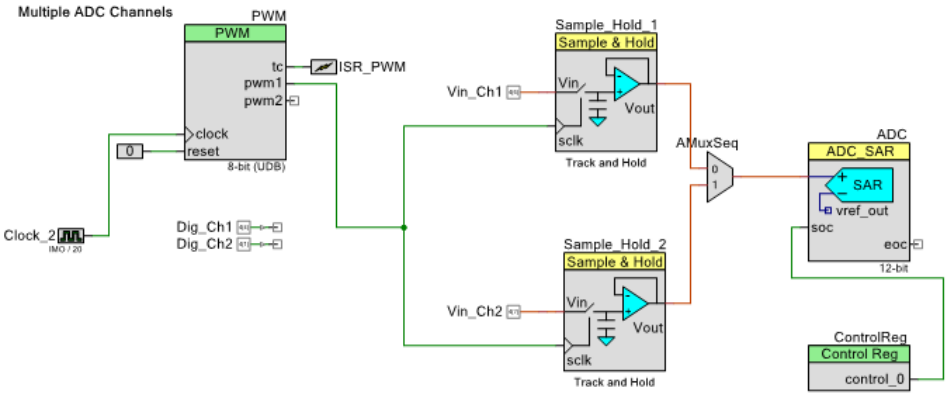

Figure 3-13 Functional block diagram of synchronous sampling from multiple sensing channels

Within the duty cycle of PWM, the tracked and hold analogue signals are multiplexed into a single ADC module, which has a condition to complete 2 sampling

cycle before the next PWM period. To realise the design, 3 main analogue modules are required for multiple synchronous sampling. Table 3-9 shows the built-in features of various MCU with their available resources for multiple sampling. Their specifications are tabulated based on the manufacturer's datasheets [27], [113, p. 8], [115]–[117].

Among the available options, there are 3 32-bit MCU meet the stated requirement: dsPIC33EP512MU814, AT32UC3C0512C and CY8C5868AXI-LP032. CY8C5868AXI-LP032 is nominated as a candidate for core computational core, which has higher analogue module block, enabling better mixed-signal embedded system environment. The software implementation of synchronous sampling is discussed in the next chapter.

CY8C5868AXI-LP035 has 3 configurable ADC modules (one 8-20-bit delta-sigma ADC and two 12-bit successive approximation (SAR) ADCs). For IMSEM, a 12-bit SAR ADC is used in the design. It has higher sampling frequency (100ksps with 12bit resolution at 60MHz processing speed) which ensures steady sampling output within the PWM period. Based on the gross power estimated provided by [118], SAR ADC has much lower power consumption compared to delta-sigma ADC (0.16mA and 4.45mA respectively).

Table 3-9 – Available features of various microcontroller unit for developing a multiple synchronous sampling system

Microcontroller	Manufacturer	Maximum flash memory (kB)	Data memory (RAM) (kB)	Maximum ADC modules	Maximum Sample and Hold (S&H) module	Maximum analogue multiplexer (MUX) module
PIC32MX575F512L	Microchip	512	64	1	1	2
dsPIC33EP512MU814	Microchip	536	52	8	2	–
AT32UC3C0512C	Atmel	512	64	1	2	–
MC56F84789	Freescale	256	32	3	–	–
CY8C5868AXI-LP032	Cypress	256	64	3	4	–

3.4.3 Memory space for integrated algorithms

Intelligent algorithms of IMSEM require multi-dimensional arrays to carry out monitoring task. To ensure sufficient memory capacity, CY8C5868AXI-LP032 has 64kB SRAM for fast reading/writing data registers. With the available datatypes in PSoC 5 compiler, each data points from analogue sensing channel is saved in a 16-bit unsigned integer datatype. By taking 4 sensing channels into account, it is suggested that CY8C5868AXI-LP032 has 3 vectors for ADC signal arrays, each with 8192 sampling points. The breakdown analysis of data lengths is tabulated in Table 3-10.

It is a must to reserve some extra SRAM for other MCU variables. Also, it should be noted that the data length has only 8192 points for a maximum 10kHz ADC sampling frequency. With 10kHz sampling frequency, it is only able to measure the signals for 0.8192 seconds (8192/10000 = 0.8192s). Such data length is too short for vibration RMD purpose. Comparing with a commercial wireless sensor node device, LXRS Wireless IEPE Sensor Node by LORD Microstrain Corporation, it has the lowest sampling period of 1.3 seconds at 104kHz and 150 seconds at 1kHz sampling frequency [119]. For the experimental test, the rotating machines has low speed configuration, which rotate at 2Hz. In other words, the sampling period could not record more than 1 periodic rotating cycle (0.5s×2s > 0.8192s). This is not advisable as it would critically limit the analysis features of IMSEM. For digital signal processing, FFT algorithm has better performance when more rotating cycles (for periodic vibration signal) is sampled.

Table 3-10 Breakdown analysis of RAM for sampled data points

Design criteria	Total
Total SRAM in CY8C5868AXI-LP032	64kB
Analogue sensing channel	
Number of channel: 2	
Number of array: 2	

Datatype: 16-bit unsigned integer	
Total sampling point: 8192	
Total memory required: 2×(16/8)×8192	32.768kB
Digital sensing channel	
Number of channel: 2	
Number of array: 1 (2 channels combined into an array)	
Datatype: 8-bit unsigned integer	
Total sampling point: 8192	
Total memory required: 1×(8/8)×8192	8.192kB
Total size for sampled signals: 32.768k + 8.192k	40.96kB
Remaining SRAM	23.04kB
Ratio by total SRAM	36%

Besides SRAM, IMSEM has built-in electrically erasable programmable read-only-memory (EEPROM) of 2kB. It is not enough for non-volatile data logging. Alternative methods shall be sought to extend the memory space of IMSEM.

To tackle the above design challenge, the IMSEM requires external memory to store sampling data. The available data arrays will be utilised as a sampling buffer to ensure all measurement data is allocated correctly after the signal acquisition process.

3.5 Data storage module

3.5.1 ALFAT system-on-chip processor – Overview and rationale

Due to limited memory a data storage module is introduced to record user configurations, measurement data, extracted computational result and fault diagnostic report. The end terminal of data storage module is removable mass storage device, such as USB thumb-drive or secure digital (SD) card. This has extended high volume of data storage, which has flash memory counted in gigabyte. Mass storage device is highly appreciated as they has direct access to computer with

appropriate file system architecture: File allocation table (FAT) or new technology file system (NTFS).

ALFAT processor by GHI Electronics offers a neat solution for data storage extension application. Integrated with internal library and file allocation system, ALFAT processor has the ability to bridge read/write process between the mass storage devices and host MCU at maximum speed of 4MB per second, as shown in Figure 3-14. Technically, the processor could be accessed through universal asynchronous receiver/transmitter (UART) or serial-peripheral interface (SPI), which are two common system interface of embedded system, readily applicable with most MCU. The technical specification of ALFAT processor is tabulated in Table 3-11 [120].

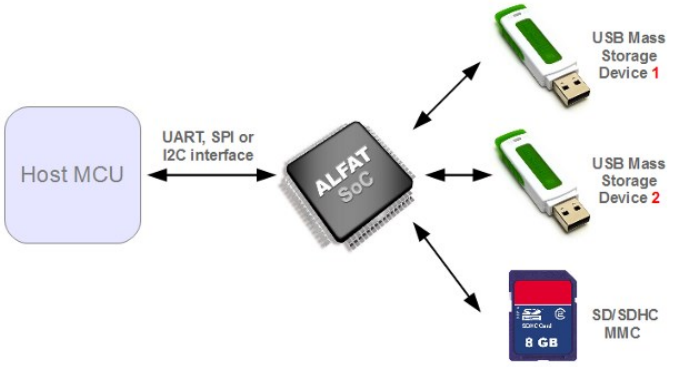

Figure 3-14 Accessing mass storage device from main MCU through ALFAT processor [120]

It should be noted that CY8C5868AXI-LP032 has SPI interface which provides direct accessibility to SD card device. However, it requires SRAM and flash memory to access the SD card interface. Moreover, Cypress PSoC does not provide a concise library for writing data in FAT format. A series of application programming interface (API) is required to enable file accurately access SD card. Despite ALFAT processor is hungry for power during operation mode (38mA), it could be turned to hibernate or off mode after the period activation of IMSEM.

Table 3-11 Technical specification of ALFAT processor [120]

Specification	Parameter
UART module	1
SPI module	1
SD card storage interface	1
USB mass storage device interface	2
File access speed on SD card	4MBps
File access speed on USB storage storage device	4MBps
Accessible file system	FAT16, FAT32
Supply voltage	3.3V
Current draw	38mA
Minimum current at hibernate	2.5µA

3.5.2 Integrating into sensing architecture

To validate ALFAT processor, the ALFAT OEM module is implemented into the working prototype. The top layout and user interface of ALFAT OEM module is illustrated in Figure 3-15. For the working prototype, CY8C5868AXI-LP032 communicates with ALFAT OEM using universal asynchronous receiver transmitter (UART) interface.

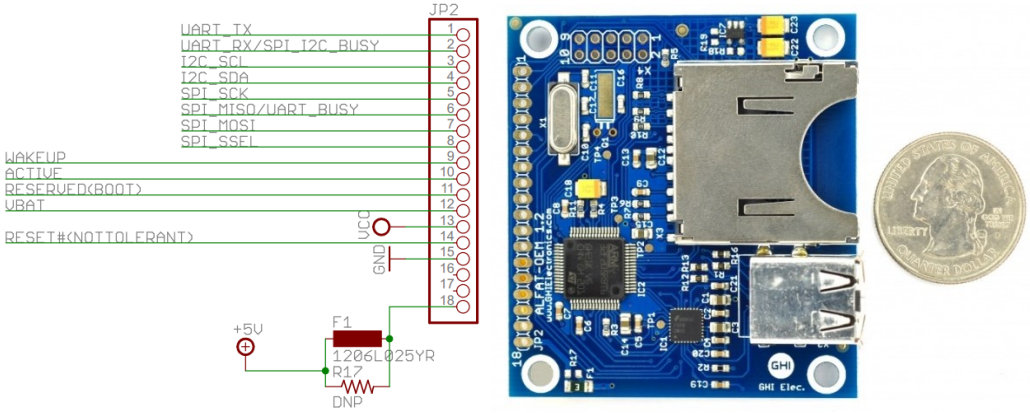

Figure 3-15 Top layout and user interface of ALFAT OEM module

The hardware connection between CY8C5868AXI-LP032 and ALFAT OEM module is illustrated in Figure 3-16. 3 pins is used to connect with the GPIO pins

of main computational unit: UART_TX [Pin 1] to P5[5], UART_RX [Pin 2] to P5[4] and UART_BUSY [Pin 6] to P5[2]. An UART module is applied in CY8C5868AXI-LP032 with the clock speed of 923.076kHz, generating a UART baudrate of 115.384kBaud. ALFAT OEM module requires an initial baudrate of 115.2kBaud before being configured to higher clock speed. It has 0.16% error with the actual generated baudrate. According to the technical article of PSoC, this error is tolerable as it is below the rated benchmark error, 2.6% [121]. Once the initialisation is completed, CY8C5868AXI-LP032 sends a command to ALFAT processor to increase transmission speed to 3MBps. The internal clock for the UART module is switched to 24MHz, generating 3MBaud for data reading/writing. Experiment shows that the SAR ADC module takes 47.052µs to completely sample 4 sensing channels (21.253kHz), while it takes 35.724µs to write 15 8-bit characters through ALFAT OEM module (28kHz). This results that the complete cycle for ADC conversion and data writing is 20.81% faster than the designated 10kHz sampling frequency. However, ALFAT OEM requires a short propagation delay to load data into data storage module when it is loaded to 30kB data. Hence, the SRAM buffer as mentioned in 3.4.3 is require to reserve sampled data at this time instance.

An experiment is carried out to investigate the data circulation within the buffer. The positive values indicate extra data signals are stored into the buffer while negative values indicate the data clearance from buffer to ALFAT OEM module. The IMSEM is set with 5kHz sampling frequency so the complete cycle for ADC conversion and data writing is 141.62% faster than the 5kHz sampling frequency, allowing 2 set of data samples to be recorded within a sampling period. This can be concluded that, the IMSEM is able to carry out continuous data logging with any sampling frequency that below 5kHz. By comparing the buffered data (requiring 83 buffer points at every propagation delay) with total buffer size, the IMSEM has

maximum burst period sampling period of 19 seconds at 10kHz, which is sufficient to accumulate useful measurements.

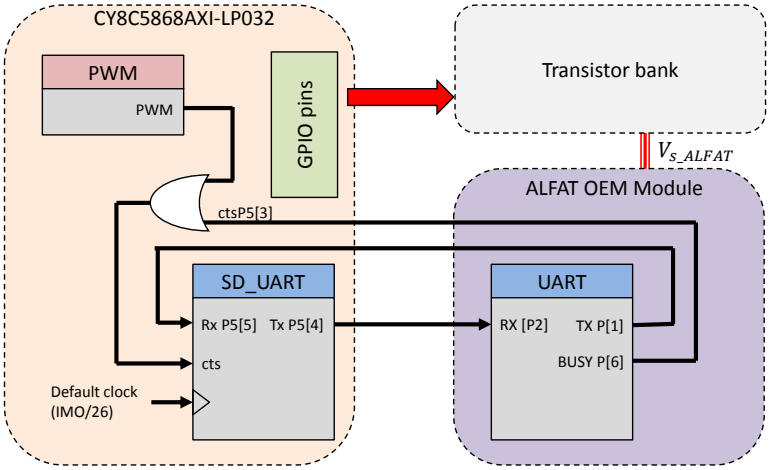

Figure 3-16 Hardware connection of ALFAT OEM module with CY8C5868AXI-LP032

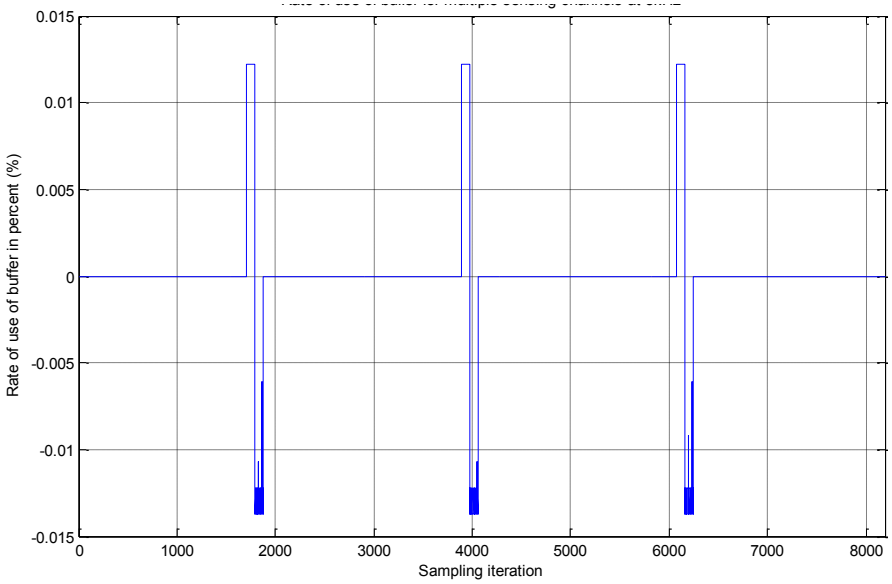

Figure 3-17 Rate of use of buffer for multiple sensing channel at 5kHz sampling frequency

The software integration of ALFAT processor will be further discussed compliant with the OSA-CBM data format, outlining in section 4.3.2.

3.6 Wireless module

3.6.1 Digi XBee – Overview and rationale

XBee-typed RF device with IEEE 802.15.4 standard is used to develop the wireless module of IMSEM. It consists of state-of-art RF frequency protocol and complete interface command in several embedded interfaces. It is simple and easy to use compared with other wireless technology, such as Wi-Fi and Bluetooth. Also, XBee modules are configured to operate within a peer-to-peer (P2P) network topology, which is independent from master/slave network relations [86]. This is advantageous to establish a flexible wireless sensing network topology for future deployment. Digi has released several types of XBee to suit different deployment criteria. Two types of XBee products, XBee 802.15.4 and XBee-Pro are compared as tabulated in Table 3-10. Both types have the similar physical layout and pin assignments, as shown in Figure 3-18.

Table 3-12 Basic specifications of XBee 802.15.4 and XBee-Pro [86]

Specification	XBee 802.15.4	XBee-Pro
Indoor/Urban Range	Up to 30m	Up to 90m, up to 60m for international variant
Outdoor Range	Up to 90m	Up to 1600m, up to 750m for international variant
RF Data Rate	250kbps	250kbps
Frequency Range	2.4GHz	2.4GHz
Transmit current (Typical)	45mA at 3.3V	250mA at 3.3V (150mA for international variant)
Idle/Receive current (Typical)	50mA at 3.3V	55mA at 3.3V
Sleep mode with external hardware interrupt	10µA at 3V	10µA at 3V

In this research work, XBee is used instead of XBee Pro due to its lower power consumption. Through a series of experiment in laboratory, the IMSEM has the ability to send diagnostic report within the range of 15m, which 50% shorter than

the range stated on the datasheet. Such limitations might be due to the signal's obstacle between the transceivers' network.

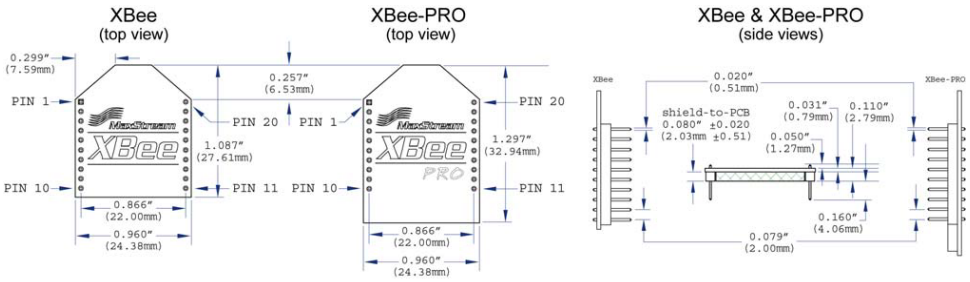

Figure 3-18 Physical layout of XBee 802.15.4 and XBee Pro [86]

3.6.2 Interfacing with main computational unit

Like ALFAT processor, the XBee 802.15.4 has host MCU connection with CY8C5868AXI-LP032. For UART communication interface, there are only 2 data transmission lines to be routed to MCU, as shown in Figure 3-19. CY8C5868AXI-LP032 uses 115.2kBaud speed to communicate with XBee, achieving a writing speed of 86.81µs for one 8bit character data. It is enough for low volume data transmission between IMSEM with other platform devices.

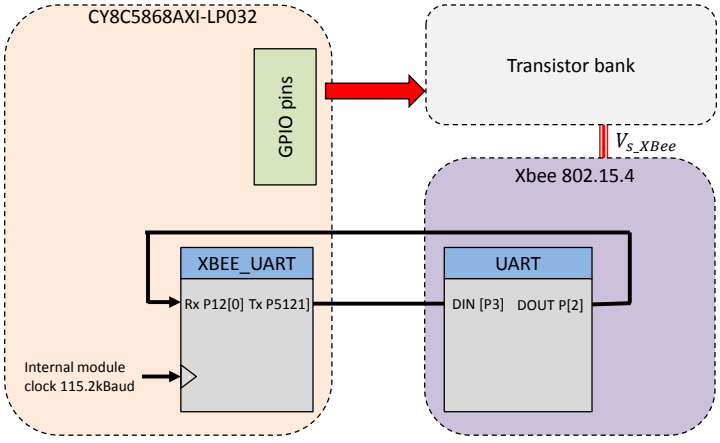

Figure 3-19 Hardware connection of ALFAT OEM module with CY8C5868AXI-LP032

Several customised commands are implemented to access IMSEM through computer user interface, as tabulated in Table 3-13. They are coded in 8-bit ASCII character data-type, which provide good readability for the user to monitor the console.

Table 3-13 Commands to communicate with IMSEM through XBee module

Commands	Description
menu	Shows menu of the IS
initialise	Reset or initialise the IS together with the SD card module
read	Read data that has been stored in the SD card of IMSEM
auto	Start monitoring process with time-driven mode
calculate	Calculate feature components of target signals in SD card
debug	Reserved for debugging purpose

3.7 Unit packaging

To accommodate all the individual component units into the preliminarily system, a two-layer printed circuit board (152.4mm×101.6mm) is fabricated for efficient means of packaging the system. This process provides a two-sided sheet of stable insulating material to a coat thin plated circuit paths to create a high quality circuit of reliable fabrication technique [122]. Normally industrial production of an identical unit would require a four-layer printed circuit board design with separate power and grounding planes for the digital circuitry. The mixed signal (analogue and digital) of the system enables the two signal types to be isolated from each other, to prevent digital switching from causing analogue degradation. The two-layer board design isolates the analogue and digital circuit components whereas the four-layer design does not.

In industry standard the design of two-layered circuit board is achieved by using CAD tools to assist. The all-in-one software "DesignSpark" featuring schematic design, auto-routing and PCB design checker is specifically used in IMSEM's circuit board.

Layers in the circuit board are output as Gerber and drill files to recognise the information of all electrical traces and pads through holes provided on the board drill file. Figure 3-20 illustrates the design of the circuit's top and bottom layers, the top silkscreen is also included to provide exact component's location.

After the design of the wireless sensing circuit board is completed, the Gerber and drilled files is sent to manufacturer for fabrication, subsequently, the various electrical components are soldered to the board. Figure 3-21 shows the key components of the finished circuit and are labelled for reference.

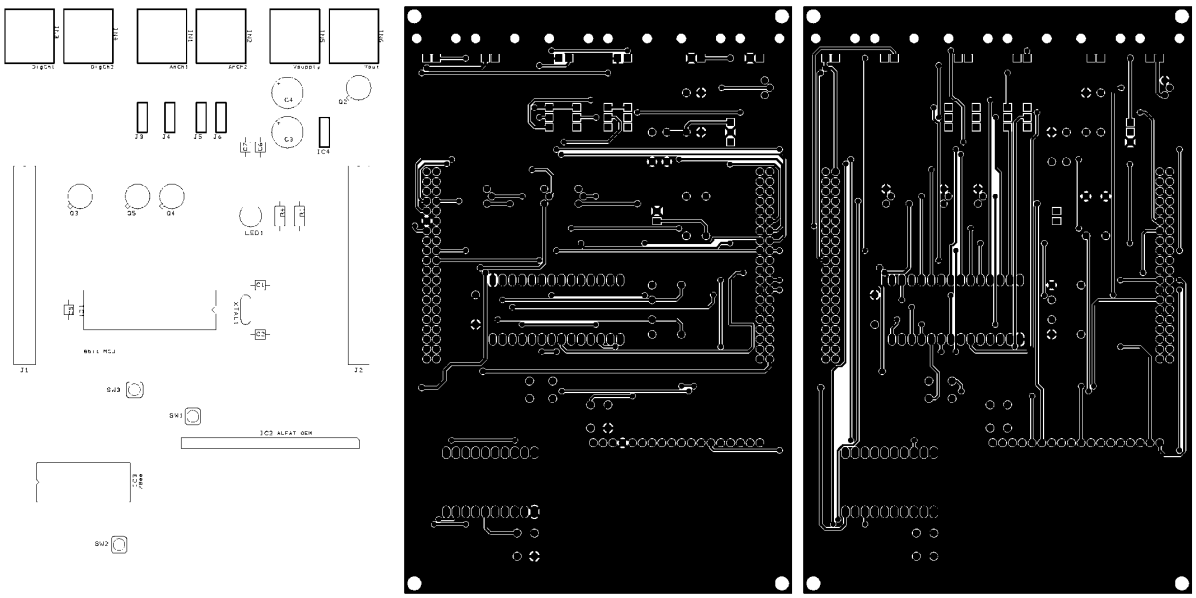

Top silkscreen Top copper layer Bottom copper layer

Figure 3-20 Printed circuit board layout (silkscreen, top and bottom layer)

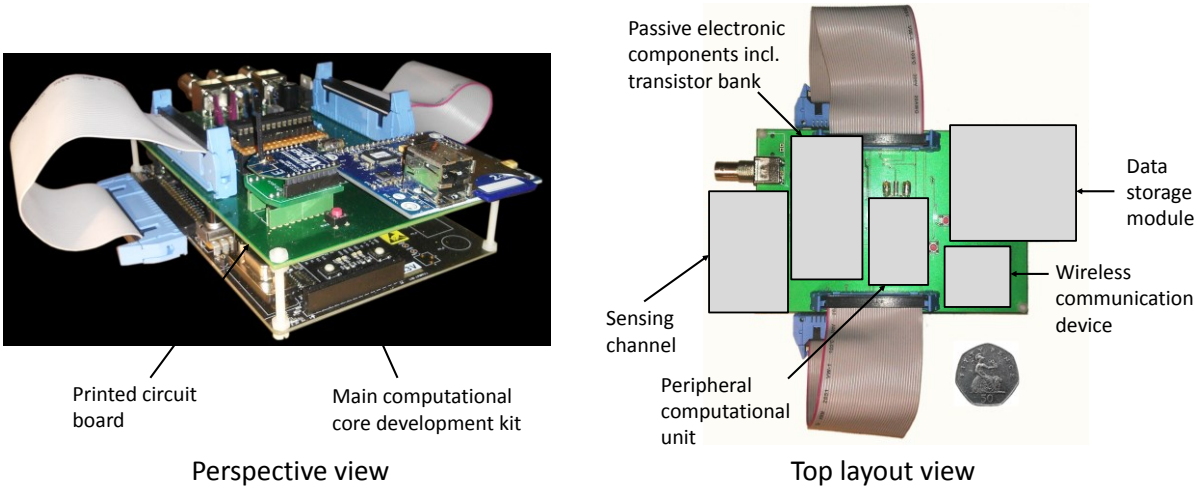

Figure 3-21 Complete printed circuit board mounted with CY8CKIT-050

3.8 Summary

In this chapter, complete hardware architecture of IMSEM is presented. Fabricated from current technology in embedded system market, the hardware design is realised with low power and low cost components. With combined component units, the IMSEM has the ability to carry out a complete decentralised RMD, featuring signal acquisition, signal conditioning, signal processing, intelligent algorithms and remote data transmission.

Two analogue and two digital sensing channels are available for different transducer measurements. In this research work, vibration signal and rotating speed are chosen as main measurand units. They are transduced with ADXL001-070 MEMS accelerometer and A2313 digital Hall-effect switch respectively. A peripheral 8-bit MCU, CY8C29466-24PXI is integrated for signal conditioning and power management purposes. A 32-bit MCU, CY8C5869AXI-LP032 is utilised as main computational core which overall manages the data circulation within IMSEM. Data storage module, ALFAT processor communicate mass storage device to extended possible memory space for data calculation and logging. Wireless communication device, XBee 802.15.4 sends summarised RMD to other system platform.

In future design work, it is envisioned that some additional design criteria shall be explored further. Firstly, the use of a 4-layer printed circuit board to minimise mixed signal interference. Secondly, a breakdown circuit design for CY8C5868AXI-LP032 to remove redundant hardware components on the off-the-shelf development kit, thus reducing power consumption at operation mode. The external modular energy harvesting circuit is integrated into the circuit board. Its respective design will be further discussed in chapter 5.

Chapter 4
Embedded software design

This chapter presents the embedded software of developed intelligent sensing system. Two sections are elaborated to discuss the software architecture of the system: Software module and embedded software applications. The software algorithm for signal analysis and standardised information managements are two main discussion topics in this chapter.

4.1 Overview

In chapter 3, the selected hardware component units of IMSEM are compiled as a single unit. The incorporated software architecture is a necessity to manage the operation flow of IMSEM. The embedded software is -defined as: "to control hardware interface in managing resource and designated workflow". Good software architecture is the key to harness the full potential of the hardware system. This chapter aims to elaborate greater details of the software framework embedded in the working prototype of IMSEM.

In Figure 2-3 discussed previously, the complete RMD architecture contains 7 functional layers, ranging from: sensing module, data manipulation, condition monitoring, health assessment, prognostic, decision support and presentation. With the advantages of the embedded technology of IMSEM, there are 5 functional layers which can be applied into the sensing architecture, reducing installation cost and human interference on RMD operations. The upgraded Figure 2-3 compliant with IMSEM is depicted in Figure 4-1.

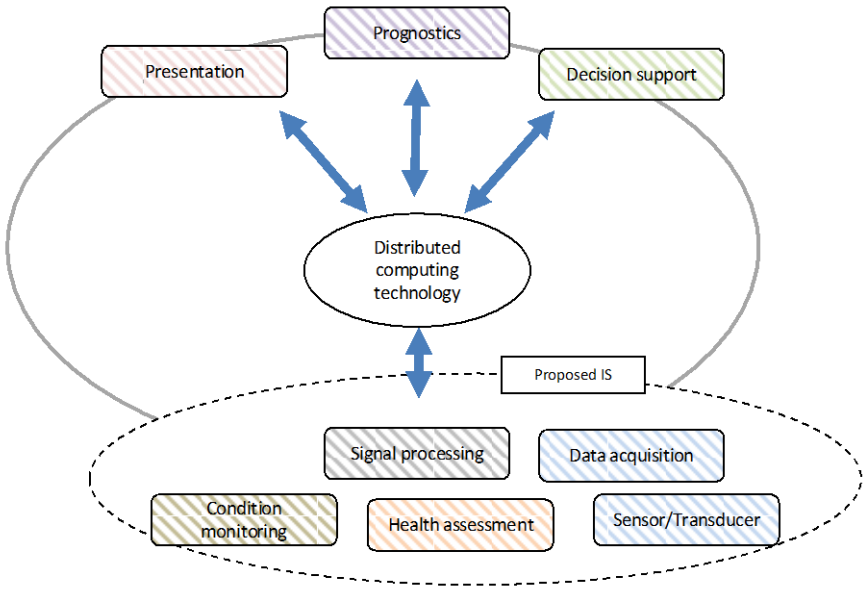

Figure 4-1 The compliant feature of IMSEM with open system CBM design

As discussed in chapter 3, the sensors being used in this research are the MEMS accelerometer (ADXL001-070) and the Hall-effect sensor (A3213). They do not have any embedded electronic to interface with. With other system modules (peripheral computational unit, main computational unit, data storage module and wireless module) they require embedded software architecture to realise their functionality. A complete software development toolchain is required to assign suitable software application onto the IMSEM.

4.2 Software development toolchain

Programming of MCU is a very challenging task for embedded software application as it involves several layers of computer language or machine language. Computer language is an elemental language of computers, comprising a long sequence of binary digits of zeros and ones (bits). It is the only language understood by computers. Generally, there are two categories of low-level languages: machine language and assembly language. A machine language or an assembly language are low-level languages that are machine oriented and are closer to the computer hardware and its configuration than high-level programming languages which are closer to human languages. Humans write in so-called high-level languages that are far more comprehensible than machine codes, and that require fewer characters to represent the task at hand. Therefore, binary notations are very difficult for humans to understand and are almost impossible for humans to use because they consist mostly of numbers or symbols.

The first step to improve the programming structure readable by humans is to translate the high-level language to assembly language by a compiler. The assembly language instructions consist of a set of symbols and letters instead of being just numbers or codes. In computer programming, compilers are tools used to convert written source code to a binary object file in machine language without referencing to the target programming devices. A linker is introduced to assign the generated

binary object file into the target devices, by replacing its relative memory address with the device memory stacks. This program is called an 'assembler'. In computer programming the whole process is known as software development chain and is widely known in a MCU programming environment.

The vendor of the chosen 8-bit MCU, CY8C29466-24PXI is programmed with C language. Cypress Semiconductor has released the IDE for their programming environment, namely Cypress PSoC Designer. At the workspace for C programming, PSoC Designer has also integrated friendly user interface for managing its analogue module resources. This has eased the development process for the user in choosing the desired features of 8-bit MCU.

The main computational unit of the IMSEM, the CY8C5868AXI-LP032 is also embedded with C language. Cypress Semiconductor Corporation has released a different software package for the PSoC5 series MCU, namely the PSoC Creator. It provides a complicated development environment due to the much sophisticated structure of the 32-bit MCU. Similarly with the PSoC Designer, a GNU-licensed compiler is included in the software package to enable excessive MCU features within the C environment.

Cypress has an advantage that it has included a programming toolkit for both the PSoC1 and PSoC5 series MCUs, namely the PSoC Programmer. It has an user-friendly interface to download desired codes onto target devices with several simple mouse clicks. In all, the selected embedded systems have included the necessary software development toolchain covering IDE, compiler, assembler and linker in a single hardware/software package.

4.2.1 User modules on computational cores

The hardware architecture represents the essential platform of the IMSEM. To adequately operate the hardware system, a comprehensive software layer is required to manage responsible resource and operations of various hardware subsystems. In

this research work, the PSoC Designer and PSoC Creator have numerous user modules to manage the hardware and analogue resources of the MCUs. To ensure an efficient development process that provides high feasibility and interoperability, the analogue software modules are designed in a modular approach as each module has independent data registers and source codes. Such an approach is well-structured and provides good encapsulation and portability.

In this research, the proposed IMSEM has respective software layers as presented in Figure 4-2. The application software comprises the top-level components that define operations and numeric parameters of respective software modules. To transmit successful information from the application software, a series of software modules serve as intermediate kernels to translate application software instructions to drive the hardware systems. The information of application software is stored in both MCUs. The main computational unit, the CY8C5868AXI-LP032 contains large-array computational algorithms, comprised of digital signal processing techniques and embedded intelligent algorithms. The user-defined application programming interface (API) is pre-programmed coding prototypes to manage software and hardware operations of the IMSEM.

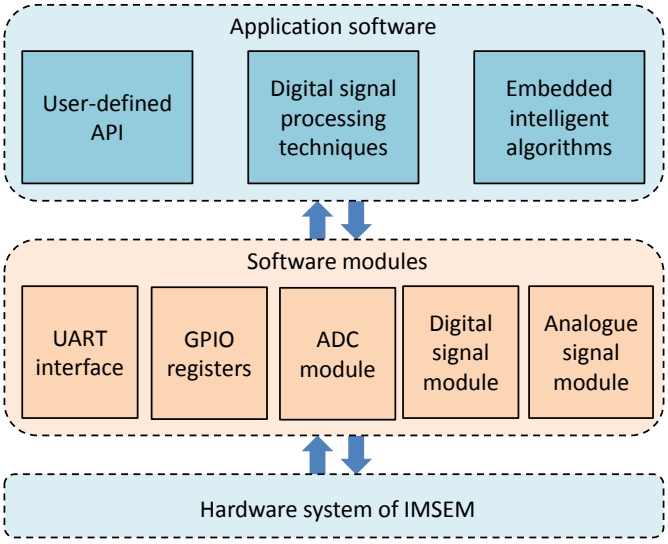

Figure 4-2 Software layers of IMSEM interfacing with respective hardware system

The software module layer of IMSEM can be partitioned into 5 parts: universal UART interface, GPIO data registers, ADC module, digital signal module and analogue signal module. The UART interface serves as the main receiver/transmitter agent to exchange information between the computational units with data storage module (ALFAT SoC processor) and wireless device (XBee 802.15.4). GPIO data registers control the data flow between two MCUs. The GPIO pins are also used to control the power rails of each hardware module as discussed in section 3.3.3. ADC module is responsible to collect measurement data from the sensing channels. By integrating analogue (Sample and hold) and digital signal (PWM) modules, it achieves simultaneous sampling within a designated sampling frequency. All integrated software modules of MCUs will be discussed in detail in the following sections.

4.2.1.1 Cypress CY8C29466-24PXI

The IDE of PSoC Designer provides a comprehensive layout representing the software modules of CY8C29466-24PXI, as shown in Figure 4-3. There are 2 types of software modules integrated in peripheral MCU: programmable gain amplifier (PGA) and low pass filter (LPF). The implementation of PGA module is to provide a high input impedance to the signal and to give more flexibility to input signal routing [123]. The gain of PGA is set at 1 to provide a unity gain from the input pins. Referring to Table 3-5, the LPF module requires 6 capacitance values as switched capacitor to operate a 2-pole LPF. The capacitance values can be either integrated on software application layer or the design wizard, which is presented in Figure 4-4. In this research work, the capacitance value of LPF module is assigned with the LPF API library: `LPF_Set1`, `LPF_Set2`, `LPF_Set3`, `LPF_Set4`, `LPF_SetA` and `LPF_SetB`. This is due to that the peripheral computational unit has to read user parameters from data storage module, which their values are not constant.

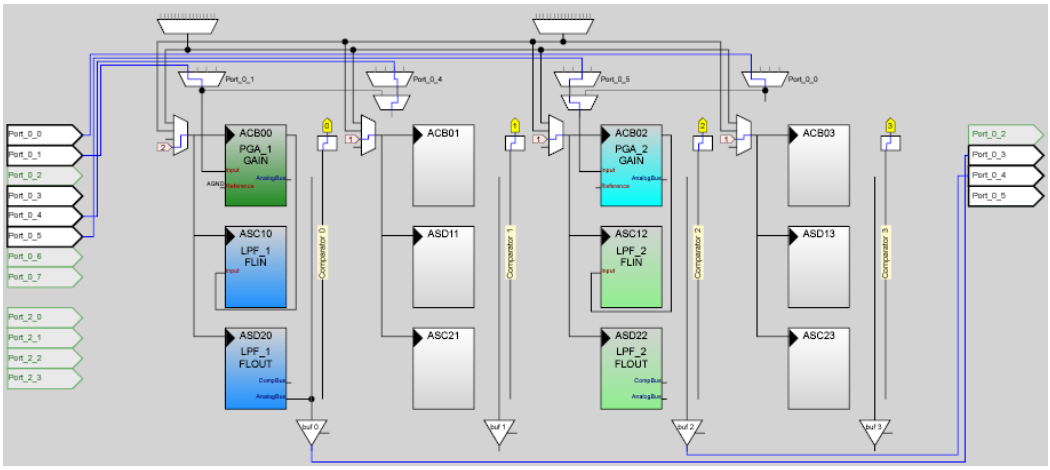

Figure 4-3 Analogue software module of peripheral computational unit in PSoC Designer

Bitwise operations are integrated on software layer to control the GPIO pins of peripheral computational unit. These programming operations run at 24MHz at normal condition. To conserve energy in sleep mode, it is advisable to turn all redundant modules into off mode. Hence, a hidden user module, SleepTimer module is integrated in peripheral computing unit. By clocking at 1Hz speed with external oscillator, the SleepTimer user module is able to provide an interrupt service routine (ISR) to check the system status at every one second. With this feature, a real time counter can be designed within peripheral computer to wake up IMSEM after a particular time interval.

There are eight GPIO pins connected to the main computational unit, CY8C5868AXI-LP032. Pin 6 and pin 7 are used as handshake checker to ensure complete data transmission between the computers, while other six pins (Pin 0 to pin 5) are used transmit/receive binary data. It is a simple protocol which can be established without occupying many resources of MCUs.

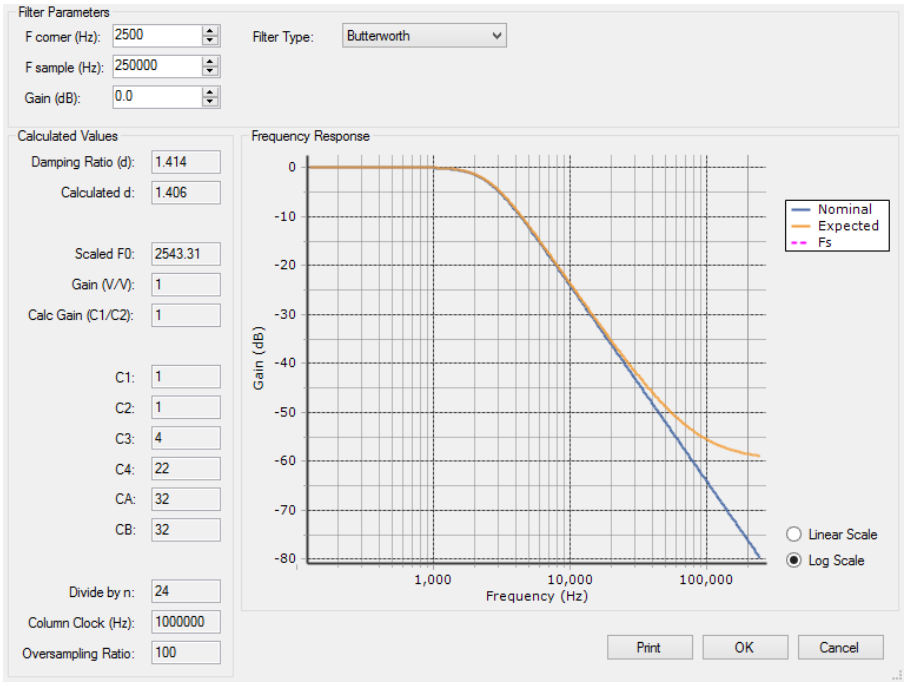

Figure 4-4 Design window of 2-pole low pass filter

4.2.1.2 Cypress CY8C5868AXI-LP032

Main computational unit with CY8C5868AXI-LP032 has more integrated software modules compared with peripheral computational unit with CY8C29466-24PXI. Figure 4-5 presents the software module routing of CY8C5868AXI-LP032.

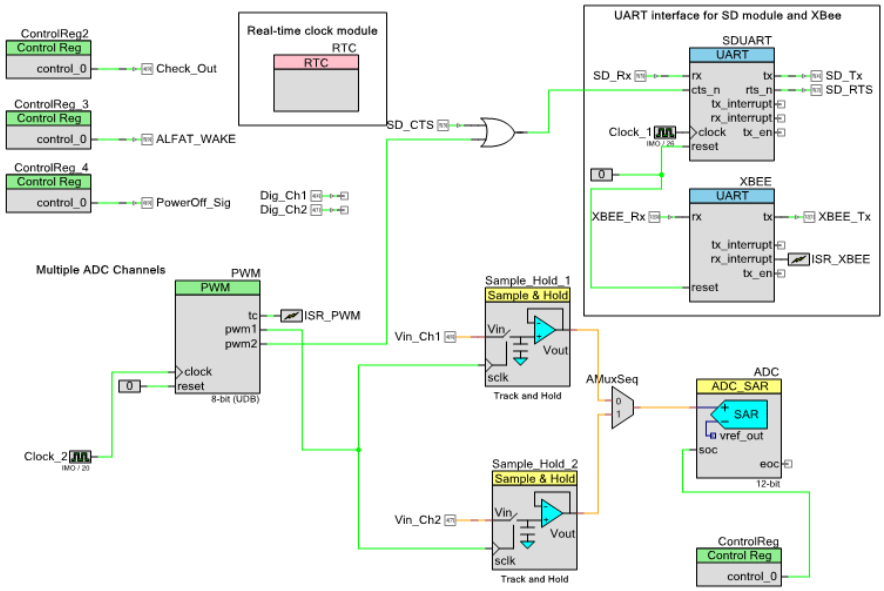

Figure 4-5 Schematic design of analogue software modules in CY8C5868AXI-LP032

Three control registers are implemented to control the software and hardware modules of IMSEM. Real time clock module (RTC) is integrated to enable independent time recording feature during experimental test of IMSEM. Two UART modules are implemented to communicate system interface of data storage module (ALFAT processor) and wireless device (XBee 802.15.4).

The software schematic routing for multiple synchronous ADC sampling is briefly discussed in section 3.4.2. The internal PWM generates 2 digital signals to toggle the operation of SDUART (UART for data storage module) module and sample and hold modules: `pwm1` and `pwm2`. Both PWM waveforms are configured based in Figure 4-6. By clocking with a 2MHz oscillator, the PWM generate a digital signal with the period of 200µs. This represents a complete sampling cycle of 5kHz. For 10kHz, the period is set to 119 segments, with the period of 100µs. The high output of pwm1 enables the sample and hold modules to track the signals until the low transition of pulse width. On the other hand, pwm2 has inversed simultaneous digital waveform which its low signal enables SDUART module to read/write data. The low transition of pwm1 after the pulse width indicates the reset of sample and hold modules, thus waiting for the next tracked signals for ADC sampling. At this time instance, pwm2 toggles high pulse to set BUSY pin on SDUART module, to avoid information loss when saving data into IMSEM data buffer.

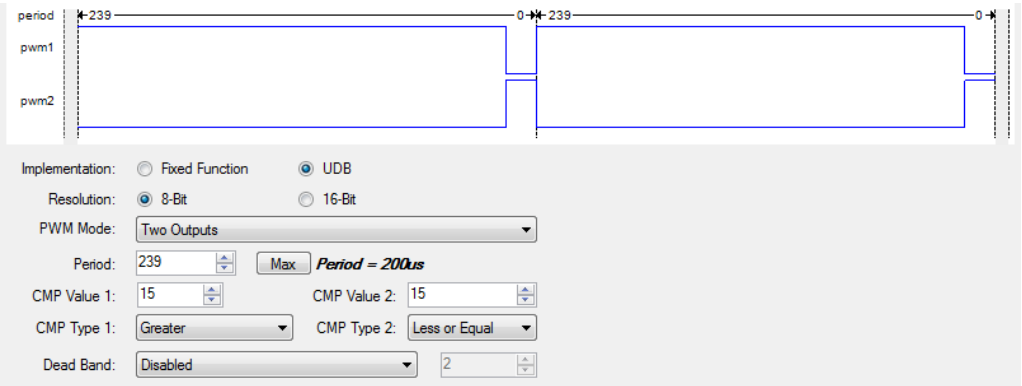

Figure 4-6 PWM waveform patterns in CY8C5868AXI-LP032

4.2.2 Programming data storage module

With UART interface, ALFAT processor requires 8-bit character command with host controller to carry out task. Table 4-1 defines simple commands to communicate with ALFAT processor. It should be noted that when ALFAT processor receives valid commands, it returns three 3-bit characters as good acknowledgement: !00. It is important to receive the acknowledgement sign before further data processing. In Table 4-1, the header [W] and [R] indicate the read and write procedure from the host controller. In this research work, it would be the main computational unit, CY8C5868AXI-LP032. The commands "Initialise" is the first compulsory instruction to mount the connected mass storage device. Once the "initialise" command is successfully executed, ALFAT processor provides 16 file handler to organise different operations.

Table 4-1 Simple commands to communicate with ALFAT processor

Commands	Format	Description
Initialise and mount MMC/SD data storage	[W] I{SP}X:{LF} [R] !00{LF}	X: Drive name: • M: SD card • U0: USB port 0 • U1; USB port 1
Open file for Read, Write of Append	[W] O{SP}>nM>{full path}{LF} [R] !00{LF}	Open file name followed full path and associate it with handle n and access mode M. n is the handle number based in hexadecimal (1 to F). M: ALFAT tasks: • R: Read • W: Write • A: Append
Read data from file	[W] R{SP}nM>ssssssss{LF} [R] !00{LF} [R] [Reading data specified with the length ssssssss bytes] [R] $aaaaaaaa{LF} [R] !00{LF}	n file handle in hexadecimal (1 to F). M: Filler character ssssssss: Data length to be read in bytes aaaaaaaa: Actual read data size in bytes
Write data to file	[W] W{SP}n>ssssssss{LF} [R] !00{LF}	n file handle in hexadecimal (1 to F).

	[W] [Write data into the chip in ssssssss bytes] [R] $aaaaaaaa{LF} [R] !00{LF}	ssssssss: Data length to be writen in bytes aaaaaaaa: Actual written data size in bytes
Flush file data	[W] F{SP}n{LF} [R] !00{LF}	Flush file handle n in hexadecimal (1 to F).
Close file	[W] C{SP}n{LF} [R] !00{LF}	Close file handle n in hexadecimal (1 to F).

4.3 Application software

Application software is defined as the device software driver which hierarchically manages the resources of software modules and thus actuating hardware system to carry out tasks. The application software, by utilizing the computational power of the core, is designed to fulfil the data analysis goals of the system owner.

In this research work, 2 main partitions are included in the application software layer: embedded intelligent algorithms for RMD fault detection and standardised format of data information. The embedded intelligent algorithms play important roles in performing modal analyses on the rotating MCM. Whereas, a proper format of data saving and logging is proposed to provide better platform integration within the data exchange format compliant with the OSA-CBM standard.

4.3.1 Embedded intelligent algorithm

In the IMSEM, the embedded algorithms comprise digital signal processing, feature extraction and data fusion. In dynamic signal analysis, computation on time domain is always limited with various vibration components lying on the same time response. Thus, the transformation of time domain into frequency power spectrum using FFT is crucial and should be first carried out to extract important feature components in the frequency domain. Secondly, feature components extraction from dynamic signal arrays defines the importance and numeric contribution to evaluate the efficiency of the RMD. Thirdly, the extracted feature components are evaluated

together with their respective contribution and weight with a previous healthy profile, which is assessed with the supervised learning algorithm, namely a support vector machine. Lastly, fault detection algorithms carry out the reasonable benchmark set by the system owner, completing a full cycle of RMD health assessment.

4.3.1.1 Fast Fourier transform

Power spectrum is an alternative method to represent signal into dimension of frequency. In discrete computation, discrete Fourier transform (DFT) is common technique to be used to do conversions. Its mathematical model can be expressed in (4-1):

$$H_n = \sum_{k=0}^{N-1} h_k e^{j2\pi kn/N} \tag{4-1}$$

Where:

- N represents total number of discrete time samples
- n represents the index of samples
- k represent the cycles per samples
- h_k represents function of discrete signal in discrete time domain
- H_n is a complex number containing amplitude and phase of Fourier component

The sampling frequency, f_s is important to determine the discrete time of the signal. Its relations with discrete frequency domain can be expressed in (4-2):

$$f_n = \frac{n}{N} f_s \tag{4-2}$$

Therefore, the frequency resolution can be altered respective to N and f_s.

Conventional DFT has very low speed in computation, which is infeasible for real-time computation. Assuming function O to be the execution time for a

mathematical instruction, the performance of $O(N^2)$. The DFT algorithm has later been evolved to FFT. Among various FFT techniques, Cooley-Tukey FFT is chosen which its performance can be expressed in $O(N \log_2 N)$ [112]. The improvement is fabulous. Assuming function O is linear, FFT is 342 times faster than DFT with $N = 1024$ points. Considering $W = e^{j2\pi/N}$, the FFT can be expressed as:

$$\begin{aligned} H_n &= \sum_{k=0}^{N/2-1} h_{2k} e^{j2\pi n(2k)/N} + \sum_{k=0}^{N/2-1} h_{2k+1} e^{j2\pi n(2k+1)/N} \\ &= \sum_{k=0}^{N/2-1} h_{2k} e^{j2\pi nk/(N/2)} + W^n \sum_{k=0}^{N/2-1} h_{2k+1} e^{j2\pi nk/(N/2)} \\ &= {H_n}^e + W^n {H_n}^o \end{aligned} \tag{4-3}$$

FFT separates DFT into two transform, ${H_n}^e$ and ${H_n}^o$, denoting the Fourier series in even and odd components respectively. Assuming set H has 1024 points, the length of N/2 at both ${H_n}^e$ and ${H_n}^e$ are 512 points. The series can be further simplified into ${H_n}^{ee}$, ${H_n}^{ee}$, ${H_n}^{oe}$ and ${H_n}^{oo}$ with the size of N/4 (256 points). Using equation (4-3), the series H_n can be further reduced to only single component and hence, ${H_n}^{eooeoo\ldots eoe} = h_k$. Using the advantages of odd/even characteristics, some repetitive summations of Fourier components can be neglected and hence improve the processing speed of Fourier calculation.

The IMSEM is capable to calculate 2048 points FFT with sampling frequency of 2.5kHz, 5kHz, 10kHz and 20kHz, with bandwidth of anti-aliasing filter of 1.25kHz, 2.5kHz, 5kHz and 10kHz respectively. This has enabled the MCM system in monitoring the machines at wide range of operational speed. Currently, two components are extracted from the power spectrum as feature components: harmonic frequency and peak amplitude. Together with statistical parameters from time domain analysis, data fusion and classification is carried out using support vector machine.

4.3.1.2 Feature extractions

Feature extractions with IMSEM involve with statistical analysis from quantised signal arrays. With available memory, the main computational unit is able to analyse a signal array with 32768 values at one time. The calculated parameters are then stored in single-floating point format in SRAM for temporary health assessment. After a single RMD operation cycles, the feature components are then written to mass storage device through data storage module.

Five feature components are extracted from the time-domain and frequency domain, as detailed in Table 4-2.

Table 4-2 Feature components extracted from core computational unit

Feature component	Source	Domain	Formula
Mean average	Vibration	Time	$\bar{x} = \frac{1}{k}\sum_{i=1}^{k} x_i$
RMS	Vibration	Time	$x_{rms} = \sqrt{\frac{1}{k}\sum_{i=1}^{k} x_i^2}$
Standard deviation	Vibration	Time	$x_\sigma = \sqrt{\frac{1}{k-1}\sum_{i=1}^{k} (x_i - \bar{x})^2}$
Kurtosis	Vibration	Time	$x_{kur} = \frac{1}{k}\sum_{i=1}^{k} \left(\frac{x_i - \bar{x}}{x_\sigma}\right)^4$
Peak	Vibration	Frequency	$x_{max} = \max(FFT(X))$

where x is the input signal. k and the total number of samples of x. i is the index of samples.

4.3.1.3 Support vector machine

The IMSEM has the ability to extract five feature components, mapping them into multi-dimensional space. These feature components need to be concluded in the data fusion layers. Support vector machine (SVM), a supervised learning model, is integrated into the data fusion layer of IMSEM. SVM was originally formulated by

Vladimir N. Vapnik in [124]. Since then, SVM has drawn attention from various research fields. It is widely implemented as a supervised learning classifier for MCM. By giving a set of training examples with classified categories, SVM builds a generalisation model that assigns new examples into a suitable category. Figure 4-7 shows an example of mapped samples on a two-dimensional feature space. The mapped data points are represented in squares and circles, which are respectively classified as negative and positive. The main idea of SVM is to establish the separating region as classification boundary between the two different classes. Ideally, the hyperplane of boundary is placed at the maximum distance of two nearest supporting data points.

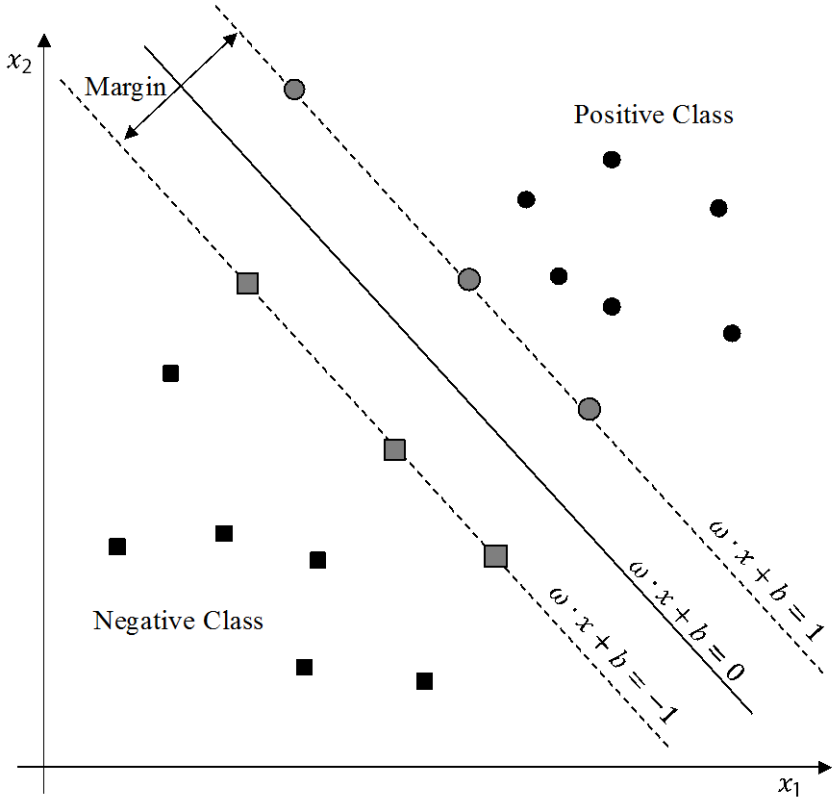

Figure 4-7 An example of 2-class classifier with two-dimensional feature vectors using SVM.

With the given number n of feature component, the input x can be expressed in vector form, $\boldsymbol{x}_i, (i = 1,2, \dots N)$. In this application, the $\boldsymbol{x}_i$ represents the calculated feature parameters of a vibration signal based on equations in Table 4-2. Two output classes are taken into account, denoted as $y_i \in \{-1, +1\}$. The outputs of $\{-1, +1\}$ represents the classification result of condition monitoring respectively: alarm and healthy. The formula of hyperplane, separating data, can be expressed as follows:

$$f(x) = \boldsymbol{w}^T \boldsymbol{x} + b = \sum_{i=1}^{N} \boldsymbol{w}_i \boldsymbol{x}_i + b = 0 \tag{4-4}$$

where $\boldsymbol{w}$ is M-dimensional vector and b is a threshold to separate hyperplane. In linearly separable margin as shown in Figure 4-7, the main objective of the SVM is to maximise the margin distance between the hyperplanes. Whereby, the nearest sample that close to the margin hyperplane can be mathematically expressed as:

$$\boldsymbol{w} \cdot \boldsymbol{x} + b = -1$$

and

$$\boldsymbol{w} \cdot \boldsymbol{x} + b = 1$$

The objective of SVM is to determine the suitable w vector. In training process, $\boldsymbol{w}$ serves as the prediction model of classification, based on the training datasets. By using geometry, the distance between margin hyperplanes can be expressed as $2/\|\boldsymbol{w}\|$, where $\|\boldsymbol{w}\|$ is the magnitude of vector $\boldsymbol{w}$. To optimise the margin distance, $\|\boldsymbol{w}\|$ should be minimised. In mathematical optimisation, Langrange multiplier is used to determine the loxal maxima of the function, which the calculation can be transformed to:

$$\min_{w,b} \frac{1}{2} \boldsymbol{w}^T \boldsymbol{w} - \sum_{i=1}^{N} \alpha_i y_i \left(\boldsymbol{w} \cdot \boldsymbol{x}_i + b\right) + \sum_{i=1}^{N} \alpha_i \tag{4-5}$$

where a is the equaivalent space of Langrangian variables, $\alpha = [\alpha_i, \dots, \alpha_n]^T$. Based on equation (4-8), the mathematical variables α, $\boldsymbol{w}$ and b can be resolved with quadratic programming. In embedded system, quadratic programming could be a hectic programming workload when calculating the variables with huge amount of training samples and feature components. For IMSEM, only 5 feature components are taken into account, which make quadratic programming to be applicable in MCU device.

Once the variables α, $\boldsymbol{w}$ and b are determined, the IMSEM is ready for classification purpose. The classification process is based on the generalised parameters α_i. Simplifying with Kuhn-Tucker condition, the the vector $\boldsymbol{w}$ can be rearranged to:

$$\boldsymbol{w} = \sum_{i=1}^{N} \alpha_i y_i \boldsymbol{x}_i \tag{4-6}$$

By rearranging equation (4-6) with equation (4-4), yields,

$$\hat{y} = \sum_{i=1}^{N} \alpha_i y_i (\boldsymbol{x}_i \cdot \boldsymbol{x}) + b \tag{4-7}$$

Where $(\boldsymbol{x}_i \cdot \boldsymbol{x})$ is the dot product of the input samples. $\boldsymbol{x}$ is the input sample vector at prediction stage. The function of $sgn(\cdot)$ could be added in to provide 2-class classification result:

$$\hat{y} = \text{sgn}\left(\sum_{i=1}^{N} \alpha_i y_i (\boldsymbol{x}_i \cdot \boldsymbol{x}) + b \right) \tag{4-8}$$

Which satisfy the following rules:When $\sum_{i=1}^{N} \alpha_i y_i (\boldsymbol{x}_i \cdot \boldsymbol{x}) + b \geq 1$, then $\hat{y} = 1$

When $\sum_{i=1}^{N} \alpha_i y_i (\boldsymbol{x}_i \cdot \boldsymbol{x}) + b \leq 1$, then $\hat{y} = -1$In equation (4-7), there is only one feature input taken into account. In the data fusion layer of IMSEM, multiple feature components are required as feature vectors for the classification function. The multi-

dimensional feature vectors can be projected into a higher dimensional feature space using kernel function $K(\boldsymbol{x}_i, \boldsymbol{x}_j)$, where j defines the number of feature components. Moreover, by substituting kernel function into equation (4-7), equation (4-9) is yielded. There are several kernel functions that are common in SVM classification. To test the validity of SVM, linear kernel function, $K(\boldsymbol{x}_i, \boldsymbol{x}_j) = (\boldsymbol{x}_i^T \cdot \boldsymbol{x}_j)$ is used and integrated into the IMSEM.

$$\hat{y} = sgn\left(\sum_{i=1}^{N} \alpha_i y_i K(\boldsymbol{x}_i, \boldsymbol{x}_j) + b\right) \tag{4-9}$$

With linear kernel:

$$\hat{y} = sgn\left(\sum_{i=1}^{N} \alpha_i y_i (\boldsymbol{x}_i^T \cdot \boldsymbol{x}_j) + b\right) \tag{4-10}$$

There are various tools available for solving the SVM classification. An open source library for support vector machines (LIBSVM) is chosen as the main source code for developing the SVM algorithms for IMSEM. Written by Lin et al. and published in [96], this provides an efficient library for SVM classification and regression. The implementation of LIBSVM on embedded systems is proven in [126]. Linear kernel is chosen as a testing kernel function for the experiment.

4.3.2 OSA-CBM data format for information exchange

The saved data format in a mass storage device is in 8-bit characters. With the compliant file system in a normal computer, it is advisable to save the data in ASCII text representation with text format. Hence, the data format for information exchange proposed in the OSA-CBM document is able to apply for better data and information exchange for future expansion and industrial deployment.

By considering the limited memory and operation time for energy saving, there are 5 main parameters to be saved in the OSA-CBM compliant data format: user configurations, raw data signals, power spectrum, extracted feature components and health assessment result. All the information in the data storage module is saved in

ASCII text representations, in which the information can be easily retrieved or edited on an end-user interface. To build an OSA-CBM-compatible system, a compliant XML schema is predefined in the SD card. The IMSEM saves five outputs in ASCII text formats: vibration signal, rotating speed, feature components, real frequency spectrums and sensor configurations. Their respective XML schemas with OSA-CBM standards are tabulated in Table 4-3.

Table 4-3 XML document type for IMSEM output respective to their XML schema

Output	XML Schema	Root element	XML filename
Vibration signal	DataAcquisition.xsd	DAWaveform	DAVibration.xml
Rotating speed	DataAcquisition.xsd	DAWaveform	DASpeed.xml
Frequency spectrum	DataManipulation.xsd	RealFrqSpect	DMfft.xml
Feature components	DataManipulation.xsd	DMDataSeq	DMData.xml
Configurations	Configuration.xsd	Configuration	ISConfig.xml

Vibration and rotating speed are retrieved from the accelerometer and Hall-effect sensor, in which the information is extracted from the data acquisition module. A frequency spectrum and computed feature components are the processed data from the data manipulation module. In order to avoid confusion, the OSA-CBM outlines namespaces for different functional layers. For example, 'DAWaveform' under 'DataAcquisition.xsd' is used for waveform information from the data acquisition layer, whilst the 'DMDataSeq' under 'DataManipulation' is used for saving the sequence of data information in the data manipulation layer. With pre-programmed algorithms, the IMSEM has the ability to arrange information in OSA-CBM based XML documents, ready for future implementation with other devices.

4.4 Graphical user interface

A graphical user interface is developed under .NET Framework 4 with C# language. The interface serves a main communication platform to arrange ASCII

data formatted information from XBee and project them onto user screen. The interface gathers condition related data from IMSEM, and save them into appropriate format with user configurations. Figure 4-8 shows the developed graphical user interface with various features to read and write data with IMSEM.

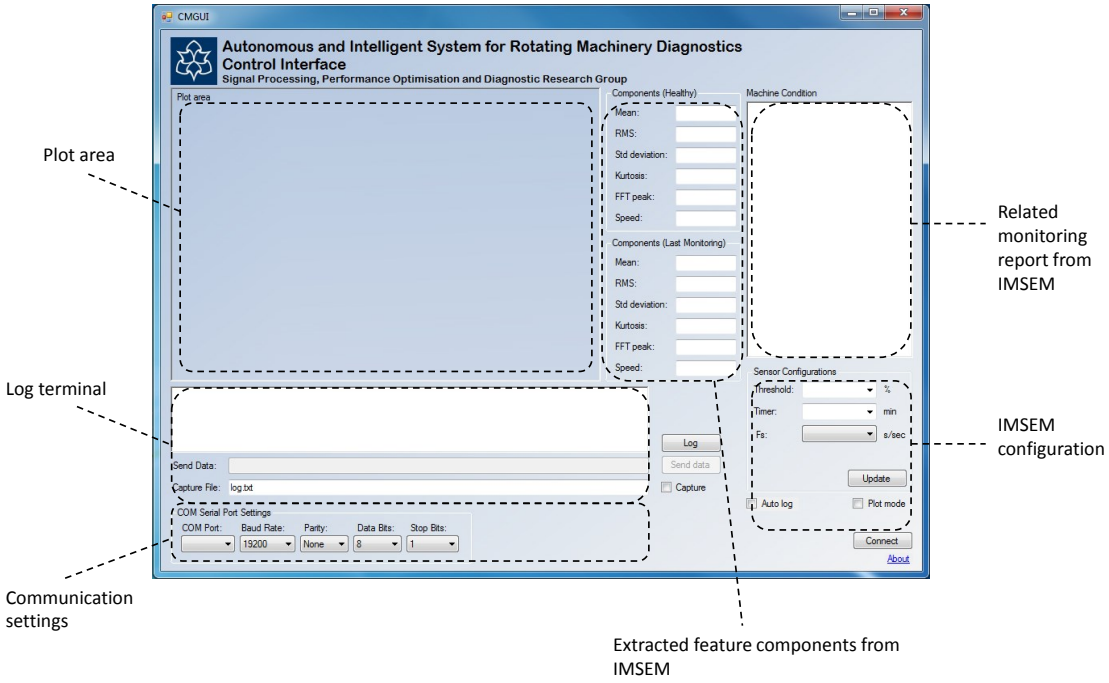

Figure 4-8 Graphical user interface communicating with IMSEM

The interface has several configurable options for users to change IMSEM's setting: time interval of monitoring, sampling frequency and monitoring thresholds. The latter two options are implemented for future expansion as they are not in used in the experiments elaborated in Chapter 6. When IMSEM finish calculating the feature parameters, the respective values will be sent to computing hub, projecting on feature components panel. The plot area displays the graphical trending data of extracted parameters. To effectively monitor the operation of IMSEM, the log terminal receives and logs IMSEM's ASCII data information. Interfacing with UART protocol, the communication settings allow user to change UART interface option of IMSEM, thus changing the speed of information transmission between IMSEM and computer platform.

The current graphical user interface is built based on establishing the monitoring system between the sensing level and computer. Similar system could be established by developing a mobile application for smartphones with various standard development kit available online, creating a mobile monitoring system for RMD. However, the communication protocol of smartphone has different frequency than XBee frequency band. To resolve this, addition hardware equipment such as IOIO-OTG by SeeedStudio and Sparkfun Electronics serves as the communication input/output agent, this bridges the gap between the mobile application and UART interface.

4.5 Summary

In this chapter, a complete software architecture of the IMSEM is addressed. There are 2 main software layers in the IMSEM: the software module and application software. The software modules include all the necessary software features to establish a complete functioning IMSEM system for RMD purpose. To efficiently utilise the resources of the software module, an application software layer is introduced. In this research work, the application software contains embedded intelligent algorithms for modal signal analysis and RMD health assessment. A standardised data format for data storage module is implemented for compatible data storage exchange within an OSA-CBM compliant system platform.

To effectively monitor the activities carried out on sensing level, a graphical user interface is developed to arrange and log the data information from IMSEM. This graphical user interface includes some simple user configurations (alarm threshold, sampling frequency, and time interval for monitoring), allowing user to alternate the sensor's settings. The extracted feature components and monitoring result are presented in numeric and trending plot. This graphical user interface serves as the main monitoring and debug when developing the IMSEM. In future designs, a more effective application software layer will be further investigated. Firstly, for the

supervised learning algorithm, the SVM should be further studied to reduce its memory and computing usage. Currently, the IMSEM sends XML data in ASCII format, which involves massive communication workload. To minimise the communication overhead, it is possible to send a compliant information structure to the target device, as specified in Open Standard Architecture—Enterprise Application Integration (OSA-EAI) [127]. This can be further investigated in future research.

Chapter 5
Design of an energy-aware module for intelligent sensor

This chapter discusses the design of an energy-aware module for an intelligent sensor. This covers one of the major scopes of the project objectives which is energy sustainability. The major sections are outlined as follows: energy harvesting, energy storage and energy consumer. Throughout the chapter, the energy budget demanded by developed IMSEM is analysed. Simulation and experimental tests prove that the working prototype is able to perform the monitoring tasks with low energy supply from the energy harvesting module.

5.1 Overview

Power source is one of the major challenges in providing indefinite long term operation of sensor network. Two main approaches are proposed to prolong the sensor's operating lifespan: power harvesting and power saving management. Power harvesting device receives growing attention due to its potential at providing external electricity to wireless sensor networks from different forms of environmental energy. However, such system has limited power generation. Therefore, power saving management has to be considered to reduce energy usage at sensing node. This chapter aims to discuss the efficient power management characteristic and power harvesting system for a wireless IS for MCM.

As discussed in section 2.4.1.1, solar energy harvesting is selected as primary energy source to power up IMSEM. Firstly, a technical specification of a photovoltaic (PV) cell is studied. Secondly, energy storage module is addressed to store ambient energy from PV cell is analysed. Then, power budget of a working IMSEM is investigated. This budget shall form the possible framework and structure of the power harvesting module for the proposed working sensor technology. An equivalent simulation model is established which its performance is validated with series of experiments.

5.2 Energy-aware system module

To enhance the energy efficiency of the IMSEM, the sensor device can be adapted into 3 system modules: energy harvesting module (source), energy storage (store) and intelligent sensing interface (consumer) [56], [82]. Each module plays important roles to establish an indefinite energy lifetime for the IMSEM. The performance of PV array is studied and analysed. Its applicability with the energy storage and energy consumer is further discussed in sections 5.4 and 5.5.

5.3 Energy source: Modelling and simulation of photovoltaic array

5.3.1 Mathematical model of photovoltaic array

Solar power harvesting is considered as one of the practical candidates to provide pre-defined charge and recharge for a remote sensing units. An equivalent circuit of PV cell can be illustrated in Figure 5-1.

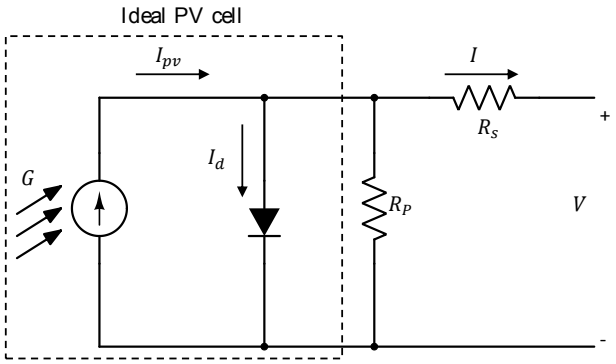

Figure 5-1 Single PV cell equivalent circuit.

Whereas, the mathematical model of an ideal PV cell can be expressed as [71]:

$$I = I_{pv,cell} - I_{0,cell}\left[\exp\left(\frac{qV}{akT}\right) - 1\right] \tag{5-1}$$

Where $I_{pv,cell}$ is the current generated by a PV cell, which is theoretically proportional to the solar irradiance, G. $I_{0,cell}$ is the reverse saturation or leakage current of the Shockley diode. q is the electron charge (1.60217646×10^{-19}C), k is the Boltzmann constant (1.3806503×10^{-23}J/K), T is the temperature of the p-n junction, and a is the diode ideality constant. The Shockley diode equation, $I_{d,cell}$ can be expressed as:

$$I_{d,cell} = I_{0,cell}\left[\exp\left(\frac{qV}{akT}\right) - 1\right] \tag{5-2}$$

However, the equation (5-1) does not represent the practical model of PV array. Practical PV array comprises equivalent series and parallel resistors. The equation (5-1) can be rearranged to:

$$I = I_{pv} - I_0 \left[\exp\left(\frac{V + R_s I}{V_t a}\right) - 1\right] - \frac{V + R_s I}{R_p} \tag{5-3}$$

Where R_s is equivalent series resistance of the PV array, R_p is equivalent parallel resistance. V_t is the thermal voltage of the array, which can be formulated as:

$$V_t = \frac{N_s k T}{q} \tag{5-4}$$

Where N_s is the number of cells connected in series. I_{pv} and I_0 are the PV and saturation currents of the array corresponding with the number of PV cells connected in parallel, N_p. Note that the cells connected in series provide higher voltage, while cells connected in parallel provide higher current. The mathematical expression of PV cells and array can be expressed in:

$$I_{pv} = I_{pv,cell} \cdot N_p \tag{5-5}$$

$$I_0 = I_{0,cell} \cdot N_p \tag{5-6}$$

Practical PV device has general *I-V* curves to represent their solar energy scavenging characteristics. Figure 5-2 shows the *I-V* curve of a practical PV device with 3 remarkable points. I_{sc} and V_{oc} is short-circuit current and open-circuit voltage of PV cells respectively. Maximum power point, which is located at (V_{mp}, I_{mp}), represents the highest power generated by PV device. It is the desirable power point to maximise the performance of PV device.

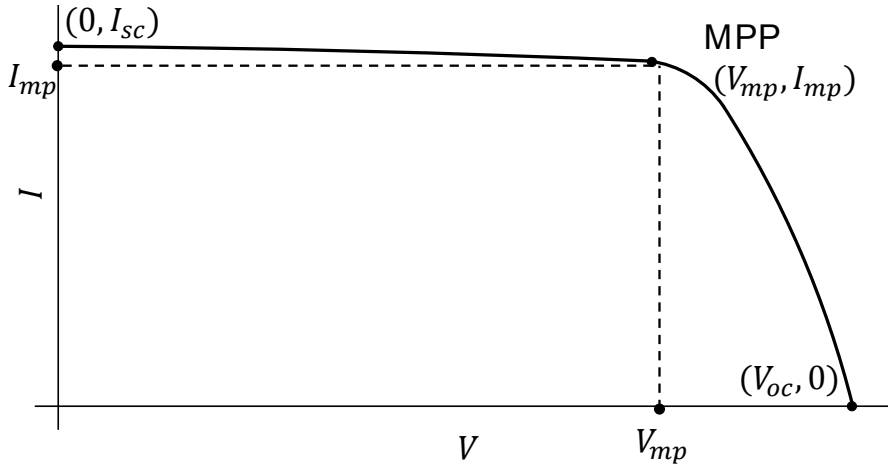

Figure 5-2 I-V curve of a practical PV array with 3 remarkable points: short circuit current $(0, I_{sc})$, maximum power point (V_{mp}, I_{mp}), and open circuit voltage $(V_{oc}, 0)$.

The PV generated current, I_{pv} is proportional to the solar irradiance. Its performance is critically dependant on the cell temperature. Discussed in [72], the mathematical equation of I_{pv} can expressed as:

$$I_{pv} = (I_{pv,n} + K_I \Delta T) \frac{G}{G_n} \tag{5-7}$$

Where $I_{pv,n}$ is the nominal PV generated current, K_I is the temperature coefficient on generated, ΔT is the relative temperature difference $(\Delta T = T - T_n)$, G is the solar irradiance on the PV device surface and G_n is the solar irradiance at nominal condition. Equation (5-7) can be easily established with the specifications provided in the datasheet of PV device. The fraction G/G_n represents the ratio of solar irradiance to nominal solar irradiance. In general, the nominal condition of PV device is: $T_n = 25°C$ and $G_n = 1000W/m^2$. The dependence of diode saturation current at nominal condition, $I_{0,n}$ with temperature can be expressed as shown:

$$I_{0,n} = \frac{I_{sc,n}}{\exp\left(\frac{V_{oc,n}}{aV_t}\right) - 1} \tag{5-8}$$

Where $I_{sc,n}$ is the short circuit current at nominal condition and $V_{oc,n}$ is the open circuit voltage at nominal condition. However, equation (5-8) does not take the

temperature coefficients into account. Developed in [73], equation (5-8) can be improved to:

$$I_0 = \frac{I_{sc,n} + K_I \Delta T}{\exp\left(\frac{V_{oc,n} + K_V \Delta T}{a V_t}\right) - 1} \tag{5-9}$$

Equation (5-9) comprises both temperature related parameters, K_I and K_V. This ensures its accuracy to express the dependence of I_0 on the temperature so that the net effect of the temperature is the linear variation of the open-circuit voltage according to the practical temperature coefficients.

5.3.2 Determining photovoltaic array parameters

For most commercial available solar panels, the vendors have provided general specifications of PV device. Most devices are tested in nominal condition ($T_n = 25°C$ and $G_n = 1000W/m^2$). A solar panel KS10T by SolarTec provides its technical specification as tabulated in Table 5-1 [128].

Table 5-1 Technical specifications of solar panel KS10T by SolarTec

Parameter	Value
Current at maximum power point, I_{mp}	0.58A
Voltage at maximum power point, V_{mp}	17.4V
Maximum power, $P_{mp} = V_{mp} \cdot I_{mp}$	10.092W
Open circuit voltage, V_{oc}	21.7
Short circuit current, I_{sc}	0.63

The datasheet of KS10T does not provide the temperature coefficients in percent. Hence, its respective temperature coefficients are estimated from similar model of other solar panel. Equations (5-7) and (5-9) can be rearranged to:

$$I_{pv} = I_{pv,n}(1 + K_i \Delta T)\frac{G}{G_n} \tag{5-10}$$

and

$$I_0 = \frac{I_{sc,n}(1 + K_i \Delta T)}{\exp\left(\frac{V_{oc,n}(1+K_v \Delta T}{aV_t}\right) - 1} \tag{5-11}$$

Concluding all equations and parameters, there are 3 unknowns to determine: a, R_s and R_p. In [73], Marcelo et al. have suggested that the value of a may be arbitrarily chosen and is totally empirical. However, this method is not analytical and the authors did not discuss it in details. Discussed in [129], I_{mp}, I_{pv} and I_0 can be expressed alternatively as:

$$I_{mp} = I_{pv} - I_0 \cdot \exp\left(\frac{I_{sc}R_s}{aV_t}\right) - \frac{I_{sc}R_s}{R_p} \tag{5-12}$$

$$I_{pv} = I_0 \cdot \exp\left(\frac{V_{oc}}{aV_t}\right) + \frac{V_{oc}}{R_p} \tag{5-13}$$

$$I_0 = \left(I_{sc} - \frac{V_{oc} - I_{sc}R_s}{R_p}\right) \exp\left(\frac{-V_{oc}}{aV_t}\right) \tag{5-14}$$

Equation (5-13) and (5-14) can be inserted into (5-12), yields,

$$I_{mp} = I_{sc} - \frac{V_{mp} + I_{mp}R_s - I_{sc}R_s}{R_p} - \left(I_{sc} - \frac{V_{oc} - I_{sc}R_s}{R_p}\right) \cdot \exp\left(\frac{V_{mp} + I_{mp}R_s - V_{oc}}{aV_t}\right) \tag{5-15}$$

To solve three unknown parameters, another 2 equations are needed. Illustrating in Figure 5-3, the maximum power point has reached to a vertex point.

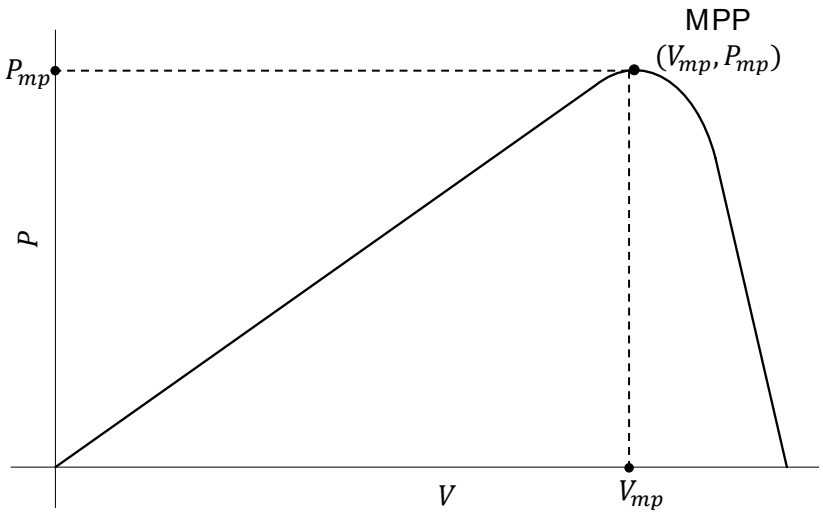

Figure 5-3 P-V curve of a practical PV array with respective maximum power point (V_{mp}, P_{mp}).

Mathematically, the derivative of power with voltage can be expressed as:

$$\frac{dP}{dV} = 0, \begin{matrix} V = V_{mp} \\ I = I_{mp} \end{matrix} \tag{5-16}$$

Any derivative of I_{sc} can also be related with parallel resistor, yields:

$$\frac{dI}{dV} = -\frac{1}{R_p}, I = I_{sc} \tag{5-17}$$

Equation (5-16) can be rewritten as:

$$\frac{dP}{dV} = \frac{d(IV)}{dV} = I + \frac{dI}{dV}V, \begin{matrix} V = V_{mp} \\ I = I_{mp} \end{matrix} \tag{5-18}$$

Since equation (5-18) can be established when $I = I_{mp}$. Equation (5-15) can be rewritten in function format as shown:

$$I = f(I, V) \tag{5-19}$$

By differentiating equation (5-19), yields:

$$dI = dI\frac{\delta f(I,V)}{\delta I} + dV\frac{\delta f(I,V)}{\delta V} \tag{5-20}$$

The derivative of equation (5-20) with voltage gives:

$$\frac{dI}{dV} = \frac{\frac{\delta}{\delta V}f(I,V)}{1-\frac{\delta}{\delta I}f(I,V)} \tag{5-21}$$

By substituting equation (5-21) into equation (5-18), with $V = V_{mp}$ and $I = I_{mp}$, gives:

$$\frac{dP}{dV} = I_{mp} + \frac{V_{mp}\frac{\delta}{\delta V}f(I,V)}{1-\frac{\delta}{\delta I}f(I,V)} \tag{5-22}$$

By expanding $f(I,V)$ with equation (5-15) in (5-22), results:

$$\frac{dP}{dV} = I_{mp} + V_{mp}\frac{-\frac{(I_{sc}R_p - V_{oc} + I_{sc}R_s)\exp\left(\frac{V_{mp}+I_{mp}R_s-V_{oc}}{aV_t}\right)}{aV_tR_p} - \frac{1}{R_p}}{1+\frac{(I_{sc}R_p - V_{oc} + I_{sc}R_s)\exp\left(\frac{V_{mp}+I_{mp}R_s-V_{oc}}{aV_t}\right)}{aV_tR_p} - \frac{R_s}{R_p}}, I = I_{mp} \tag{5-23}$$

Another equation can be expressed can be expressed as:

$$\frac{1}{R_p} = \frac{dI}{dV} = \frac{-\frac{(I_{sc}R_p - V_{oc} + I_{sc}R_s)\exp\left(\frac{I_{sc}R_s-V_{oc}}{aV_t}\right)}{aV_tR_p} - \frac{1}{R_p}}{1+\frac{(I_{sc}R_p - V_{oc} + I_{sc}R_s)\exp\left(\frac{I_{sc}R_s-V_{oc}}{aV_t}\right)}{aV_tR_p} - \frac{R_s}{R_p}}, I = I_{sc} \tag{5-24}$$

Equations (5-15), (5-23) and (5-24) can be used to determine 3 unknown parameters. Figure 5-4 presents the sequential flowchart to determine the parameters. Note that these equations are transcendental equations, which can be solved using numerical analysis methods.

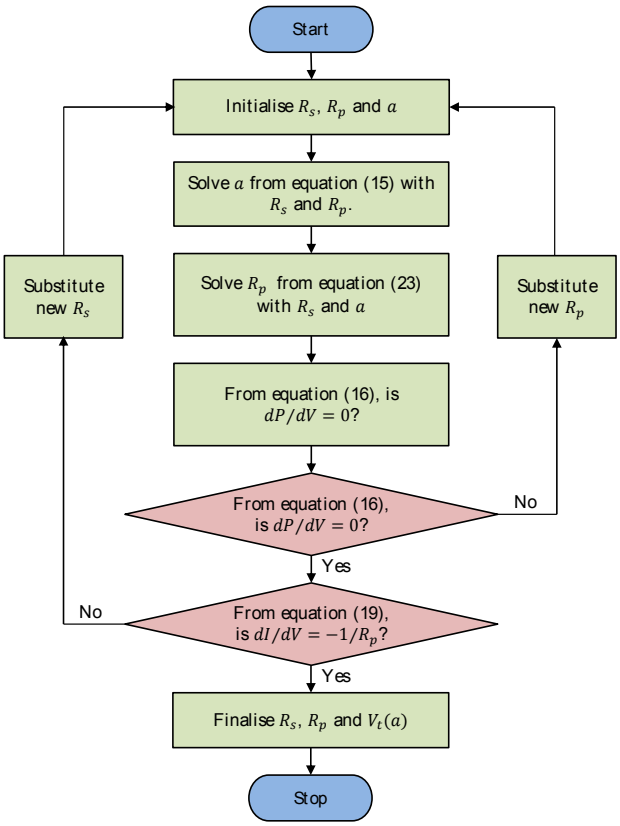

Figure 5-4 Flowchart to determine 3 unknowns: $R_s, R_p, V_t(a)$ of PV panel [129].

5.3.3 Simulation of photovoltaic array

The mathematical flowchart presented in Figure 5-4 consists complicated numerical analysis which occasionally, does not provide convergent results. Presented in [73], R_p and R_p are solved at the point where $dP/dV \neq 0$. Hence, equation (5-23) has been omitted at the last phase of numerical analysis. The calculated parameters of KS10T are tabulated a shown:

Table 5-2 Calculated parameters of solar panel KS10T at nominal conditions

Parameter	Value
Current at maximum power point, I_{mp}	0.58A
Voltage at maximum power point, V_{mp}	17.4V
Maximum power, $P_{mp} = V_{mp} \cdot I_{mp}$	10.092W
Open circuit voltage, V_{oc}	21.7V
Short circuit current, I_{sc}	0.63A

Temperature coefficient of current, K_i	0.06%/K
Temperature coefficient of voltage, K_v	-0.36%/K
Saturation current at nominal condition, $I_{0,n}$	3.8557×10^{-8}
PV array current, I_{pv}	0.63A
a	1.3715
R_s	0.0035 Ω
R_p	1200Ω

Note that $I_{pv,n}$ is the deduced current from I_{sc}. The mathematical relation of $I_{pv,n}$ and I_{sc} can be expressed as:

$$I_{pv,n} = \frac{R_p + R_s}{R_p} I_{sc} \tag{5-25}$$

A simulation model of PV arrays is built with MATLAB Simulink, as shown in Figure 5-5. The subsystem of the Simulink model is shown in Figure 5-6.

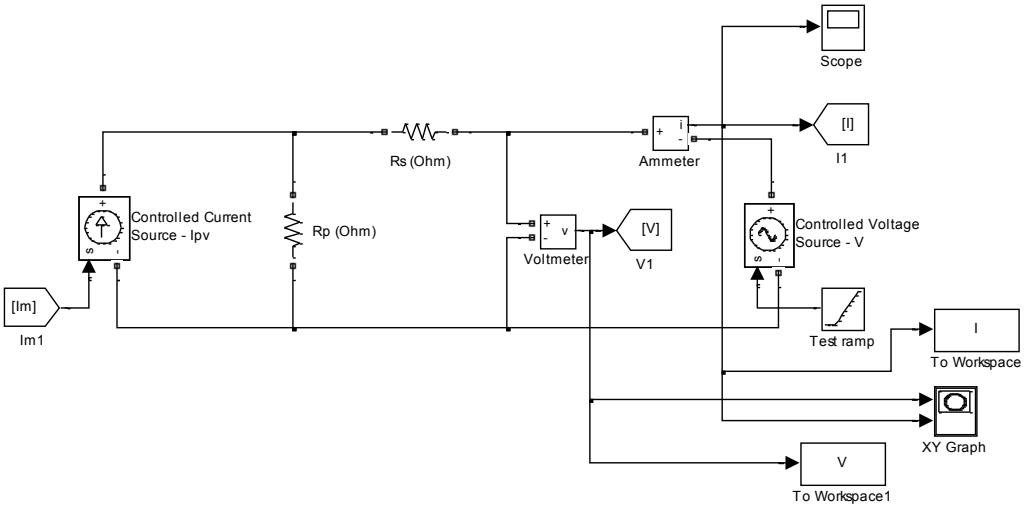

Figure 5-5 Simulink model of PV array.

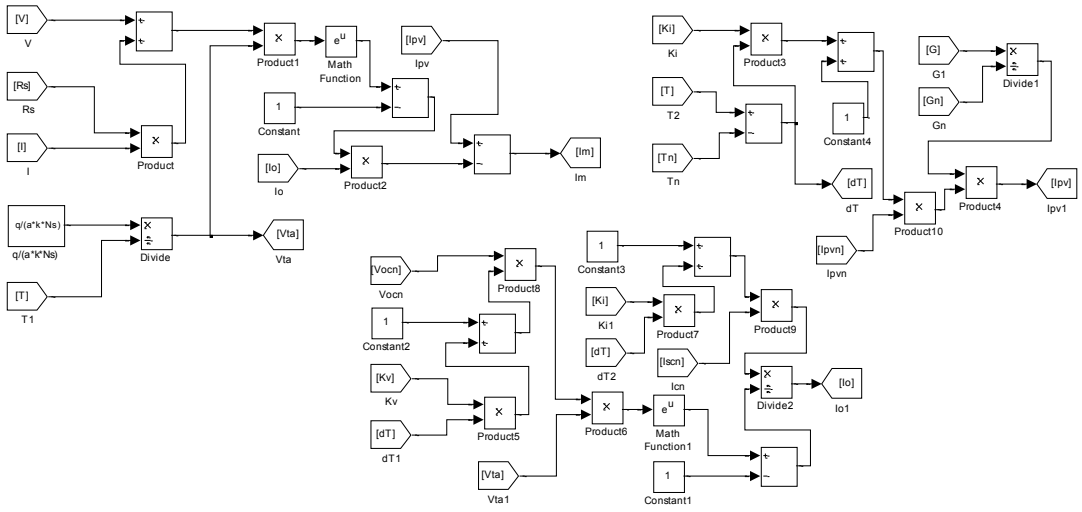

Figure 5-6 Subsystem of PV Simulink model

The function of the model is well discussed in [73]. The simulated I-V curves of KS10T are then compared with the experimental results in 3 different solar irradiance input. The calculated values of R_s and R_p are finely tuned to match the actual performance of KS10T. It is a trial-and-error process to improve the Simulink model. In Figure 5-7, the end results show simulated results show that the Simulink model has similar performance as actual model. With the obtained results, it is found that the Simulink PV model could produce accurate results for further simulation and analysis.

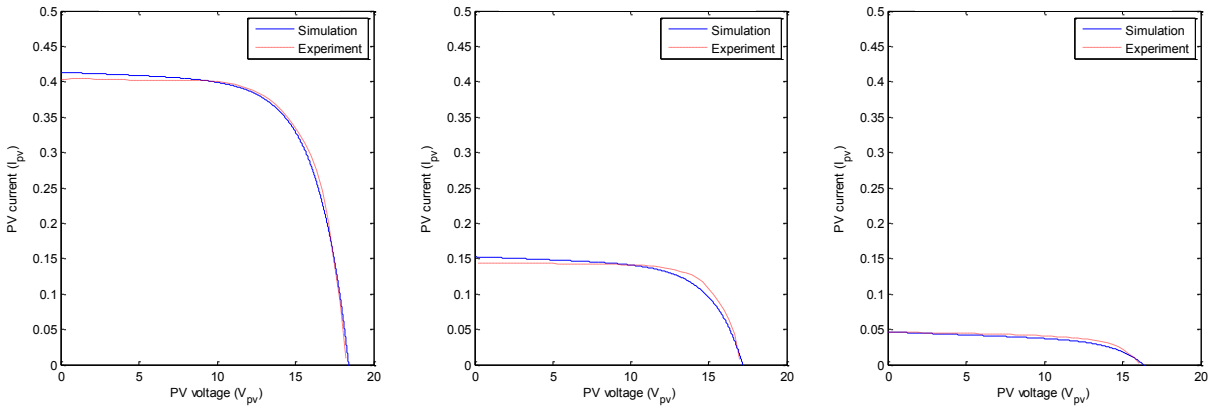

(a) (b) (c)

Figure 5-7 I-V curves of SolarTec KS10T – comparison of simulation and experimental result: (a) G = 700W/m^2, (b) G = 260W/m^2, (c) 80W/m^2

5.4 Energy storage: Supercapacitor array

5.4.1 Basic model of supercapacitor

Supercapacitor, by its definition, is a capacitor which has tremendous high capacity to store energy. Common supercapacitor has capacitance of 0.1F and above. The schematic of supercapacitor can be illustrated as shown in Figure 5-8 [84]. There are various approaches to build equivalent supercapacitor model. Stated in [84], supercapacitor has voltage-dependency capacitance. Hence, to accurately build a simulation model, it is necessary to obtain the non-linear capacitance values by carrying out supercapacitor state of charge (SoC) and state of discharge (SoDC) experiment. Based on Figure 5-8, there are 6 unknown variables to be determined: R_1, R_2, R_3, R_p, C and C_p. Each unknown components represents the actual electrical properties which could be observed from the SoC and SoDC of supercapacitors.

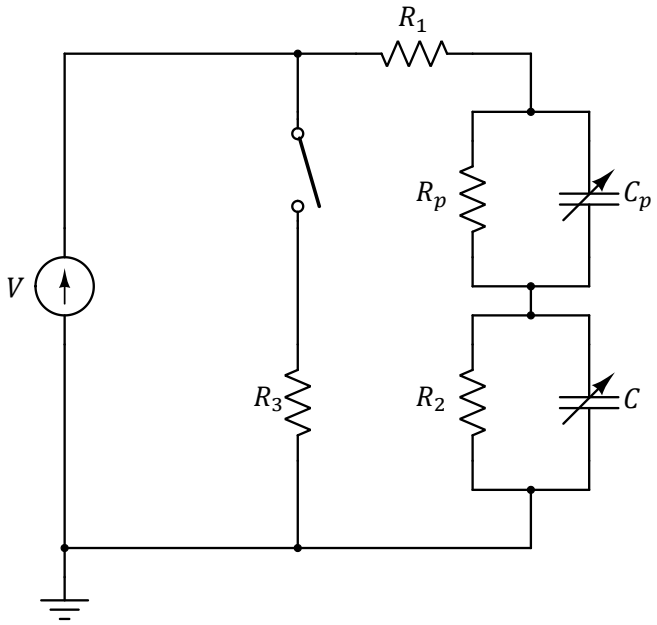

Figure 5-8 Basic equivalent schematic model of supercapacitor.

The unknown variable C represents the non-linear capacitance of supercapacitor. Despite its rated value could be easily determined in any capacitor datasheets, it is

voltage-dependent parameter which its non-linear behaviour should be determined for accurate analysis. The capacitance value C_p could be expressed as:

$$i_{scap}(t) = C\frac{d}{dt}V_{scap}(t) \tag{5-26}$$

Where i_{scap} is the current induced by the supercapacitor and $V_{scap}(t)$ as voltage level of superapacitor respective to time. This equation could be used to calculate voltage-dependent capacitance at different level of voltage level. To calculate V_{scap}(t), equation (5-26) could be rearranged to:

$$V_{scap}(t) = \int \frac{i_{scap}(t)}{C} dt \tag{5-27}$$

Another equation to express the electrical charge could be expressed as:

$$Q = \int i_{scap}(t)dt \tag{5-28}$$

Where Q represents the electrical charge in supercapacitor, which its electrical characteristic can be expressed using the integration of current with time. To calculate C, equations (5-26) and (5-27) could be rearranged, yields:

$$C = \frac{\Delta Q}{\Delta V_{scap}} \tag{5-29}$$

The capacitance value can be calculated by determining the ratio between the rate of changes of charge and voltage. Figure 5-9 shows the required parameters to obtain C. For other unknown variables, the value of capacitance C_p is chosen to be one thirteenth of C with reasonable discussion in [84] and [81]. R_1 representing equivalent series resistance (ESR) could be determined by observing manufacture's datasheet or by a rapid change in charging current and measuring the initial voltage variation. Wheareas R_3 can be calculated by measuring the voltage drop after charging current has been turned off. The values of R_2 and R_p are difficult to acquire from SoC and SoDC measurements. Therefore, their respective values are

determined by tuning the parameters of the simulation to match experimental results.

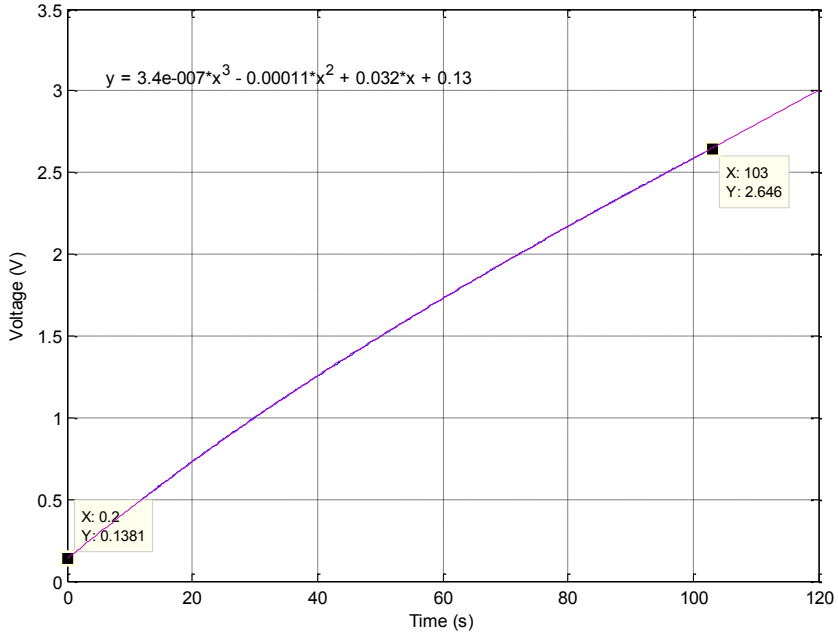

Figure 5-9 State of charge of supercapacitor with constant 2.5A supply

In this research work, Cooper Bussmann HV100F supercapacitor is used as the main energy buffer unit for the IMSEM. Its technical specifications from datasheet are listed in Table 5-3.

Table 5-3 Technical specifications of Cooper Bussman HV100F supercapacitor

Parameter	Value
Rated capacitance	100F
Rated voltage	2.7V
Maximum leakage current at nominal condition	0.26mA
Equivalent series resistance (ESR)	0.012Ω

The HV100F is then taken into test to determine the unknown variables for accurate simulation model. By applying polynomial fitting to the behaviour of state of charge of supercapacitor, a polynomial equation could be determined: $y(x) = V_{scap}(t) = 3.4 \times 10^{-7}t^3 - 1.1 \times 10^{-4}t^2 + 3.2 \times 10^{-2}t + 0.13$. This could be used to

calculate respective capacitor voltage at different time instances. Note that the capacitor voltage changes according to the charge current, as shown in Figure 5-10.

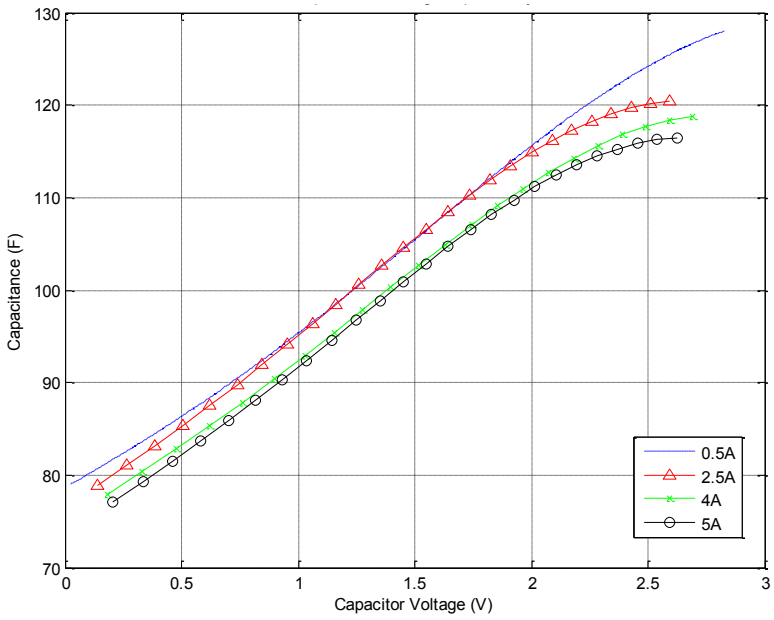

Figure 5-10 Capacitance voltage dependency of HV100F supercapacitor

This clearly shows that in practice, the function of voltage-dependent capacitance is non-linearly related to two independent components: V_{scap} and I_{scap}. Similar average capacitance values of HV100F are also tabulated in Table 5-4. Their respective capacitance value is 100F, which satisfies the capacitance value stated in the datasheet [130]. Since the main power supply is from PV power source, the function of voltage-dependent capacitance, $C(V)$ at low charge current is taken into account. Whereby, the nominated PV current is rated at average 0.63A.

Table 5-4 Experimental test to calculate the capacitance value of HV100F supercapacitor

Test number	Supply current (A)	Δt (s)	V_0 (V)	V_1 (V)	Q (C)	C (F)
1	0.5	585.4	0.02423	2.829	292.7	104.3579
1	2.5	103	0.1381	2.646	257.5	102.6755

2	4	66	0.1805	2.781	264	101.5189
3	5	49.2	0.2058	2.665	246	100.0325

By applying equations (5-26) to (5-28). The respective specification parameters of HV100F supercapacitor could be determined, as tabulated in Table 5-5.

Table 5-5 Calculated variables of HV100F supercapacitor

Parameter	Value
C	$(7.078 \times 10^{-7}V^5 - 9.3161 \times 10^{-1}V^4 + 2.1196V^3 + 0.89595V^2 + 14.521V + 78.623)$F at $i = 0.5$A
C_p	$(C/13)$F
R_1	0.0144Ω
R_2	10000Ω
R_3	391.6755Ω
R_p	0.003Ω

5.4.2 Simulation model of supercapacitor

With all calculated parameters of HV100F, an equivalent model circuit can be built using Simulink, as shown in Figure 5-11. The model block C contains a subsystem which generate respective capacitance voltage using a lookup table (with the $C(V)$ determined in Table 5-5). This forms a model equation expressed in (5-27). The saturation block emulates the maximum voltage could be supplied into a single HV100F supercapacitor. Note that the rated voltage of single capacitor is insufficient voltage level for energy consumer (The experimental energy consumer requires approximate 4.8V at full operation mode, which will be discussed in the section 5.5). A supercapacitor bank consisting several supercapacitor connected in series is necessary to be implemented into the system. 2 HV100F supercapacitors are connected in series to provide a stable voltage supply at 5.6V.

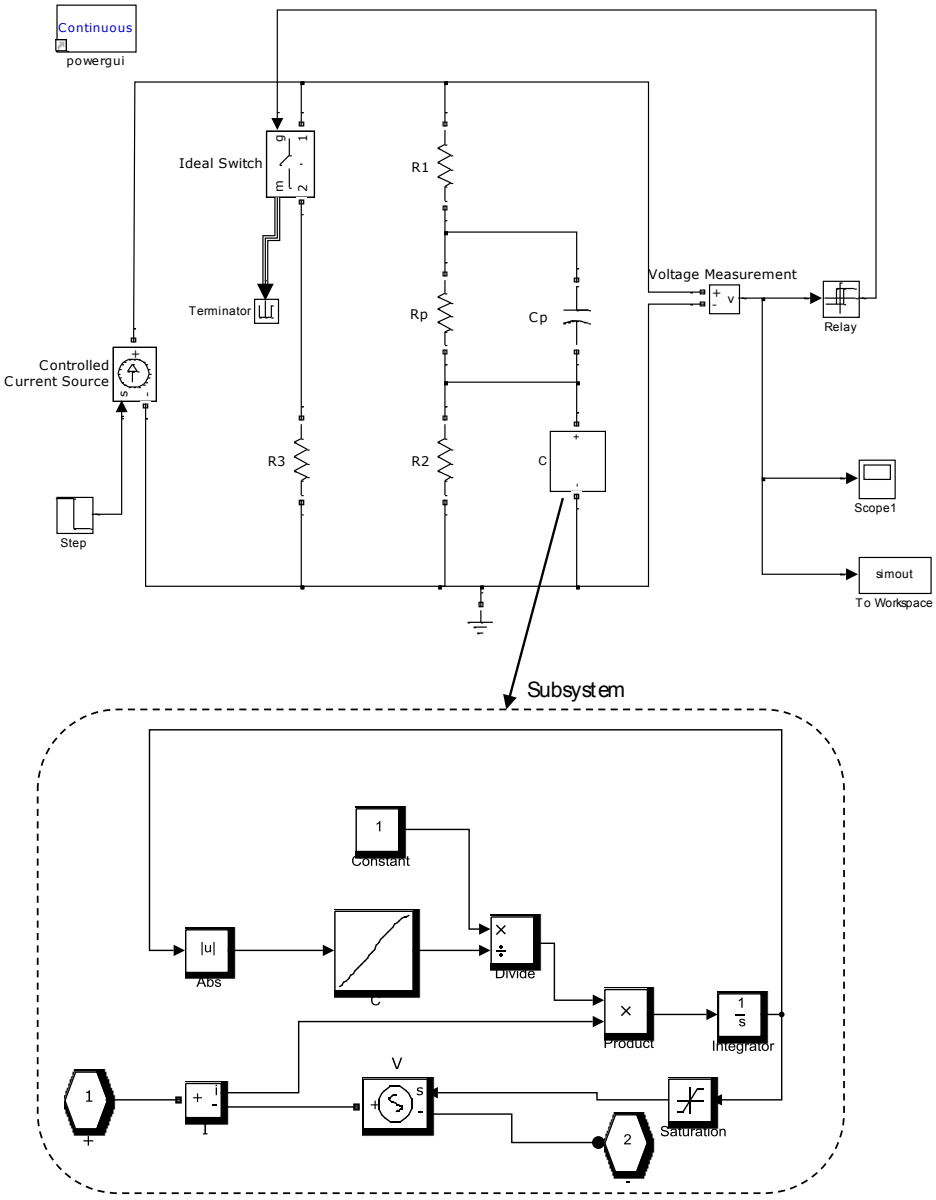

Figure 5-11 Model circuit in Simulink with nonlinear capacitance

The simulation results are then compared with experimental results with 4 different levels of current sources: 0.5A, 2.5A, 4A and 5A, as shown in Figure 5-12. Note that the supercapacitor has linear charging characteristics and it takes 600s, 105s, 72s and 50.6s to reach rate voltage with the charge current of 0.5A, 2.5A, 4A and 5A respectively. The simulated results are identical with experimental results

in terms of SoC behaviour and sudden voltage drop when the current supply is disconnected. The SoDC behaviour of HV100F supercapacitor is carried out in the next section, where the power budget of IMSEM is formulated.

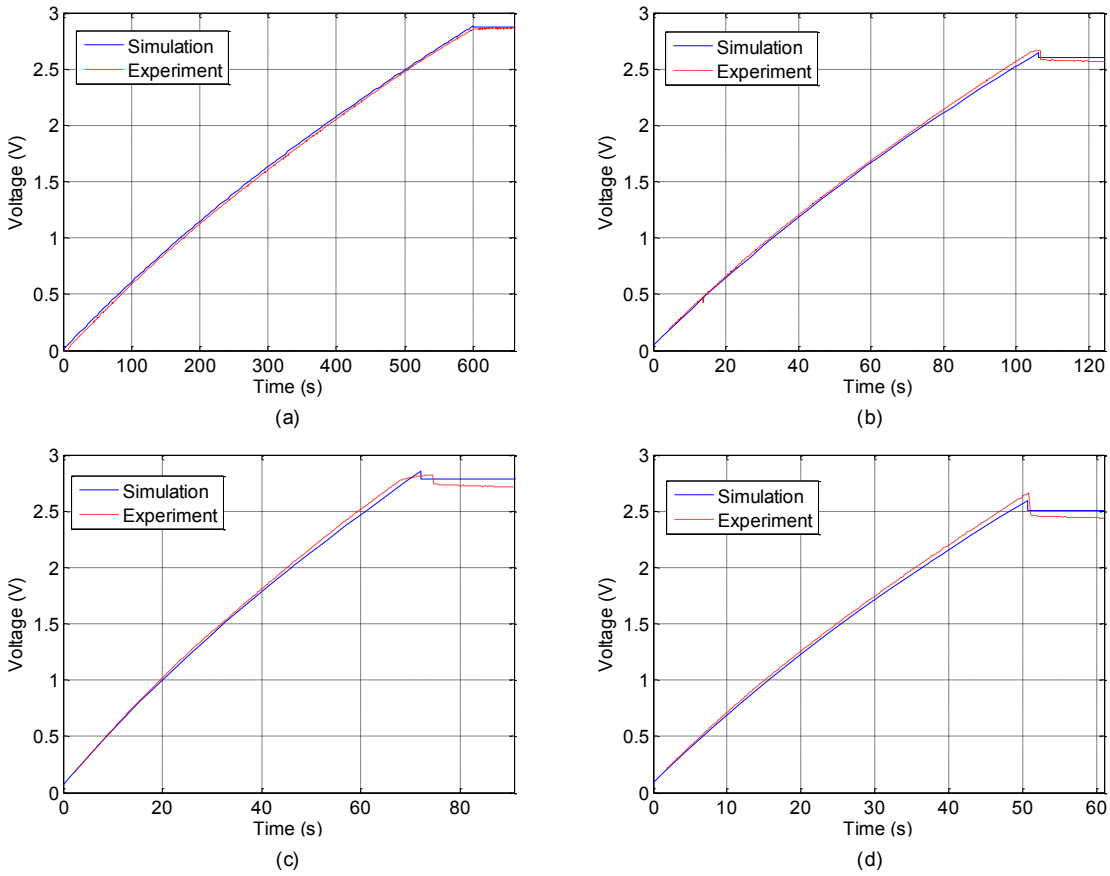

Figure 5-12 Comparison of simulation and experimental result of supercapacitor on state of charge with different charge current: (a) 0.5A, (b) 2.5A, (c) 4A, (d) 5A

5.5 Energy consumer: Power budget of IMSEM

5.5.1 Operation characteristic

The proposed IMSEM is designed to carry out periodic (off-line) monitoring scheme, in which that the fault diagnosis is carried out at selected time interval in the field. Therefore, the IMSEM operation cycle can be divided into different time slots$n = 1, \ldots k$, where n is the number of time slots for a day. Figure 5-13 gives a clear illustration on operation cycle, time slots and duty cycle. Operation cycle

denotes the full operation time of a device in a day. Its subset contains two activity slots: active and inactive period. This allows easier and accurate calculation for energy budget. To estimate the total energy of each time slot n, the power consumption can be integrated, within time period T, yields:

$$E_c(n) = E_{c1}(n) + E_{c2}(n) = \int_t^{t+T} P_c(n)dt\,, T = T_1 + T_2 \tag{5-30}$$

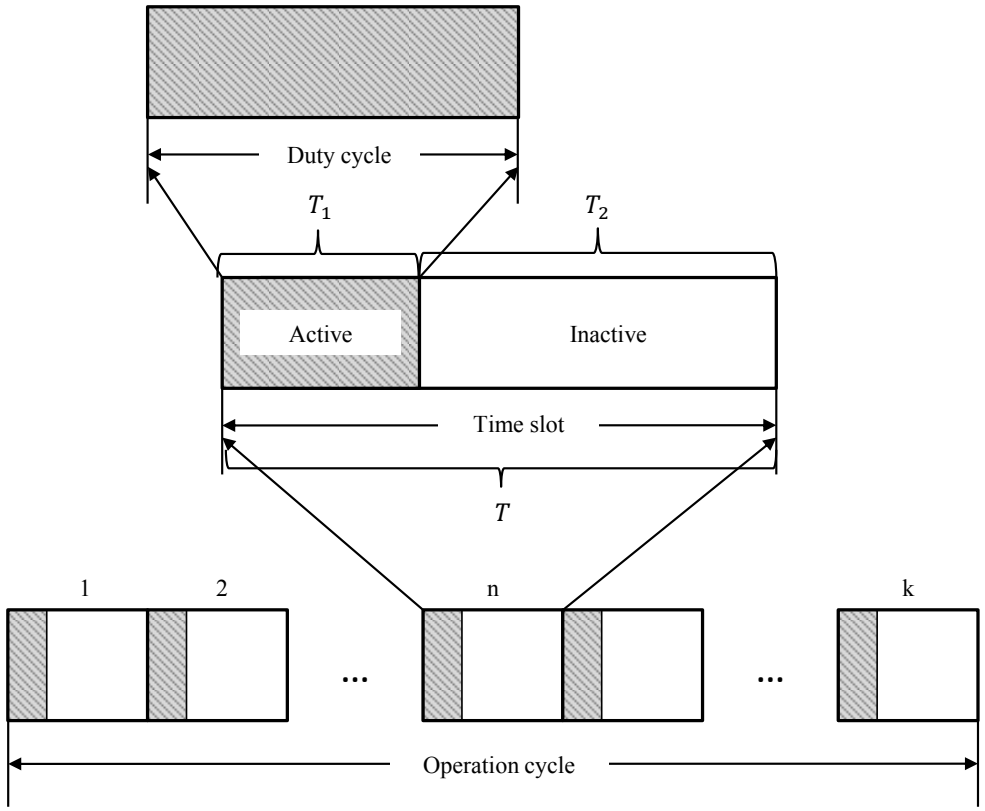

Figure 5-13 Operation cycle with time slots and duty cycles

E_c denotes the energy consumption within the time period T. T is the time slot duration for a complete duty cycle. E_{c1} and E_{c2} are portioned energy consumption within active and inactive mode. T_1 and T_2 represents the time duration of active and inactive mode respectively.

IMSEM needs external power management module to monitor the energy usage across the whole system platform. To avoid excessive energy consumption, high power consumption module such as core computational unit, data storage module

and wireless communication is put into low-power state when IMSEM switches to inactive mode. An energy consumer module of IMSEM can be illustrated in block diagrams as shown in Figure 5-14.

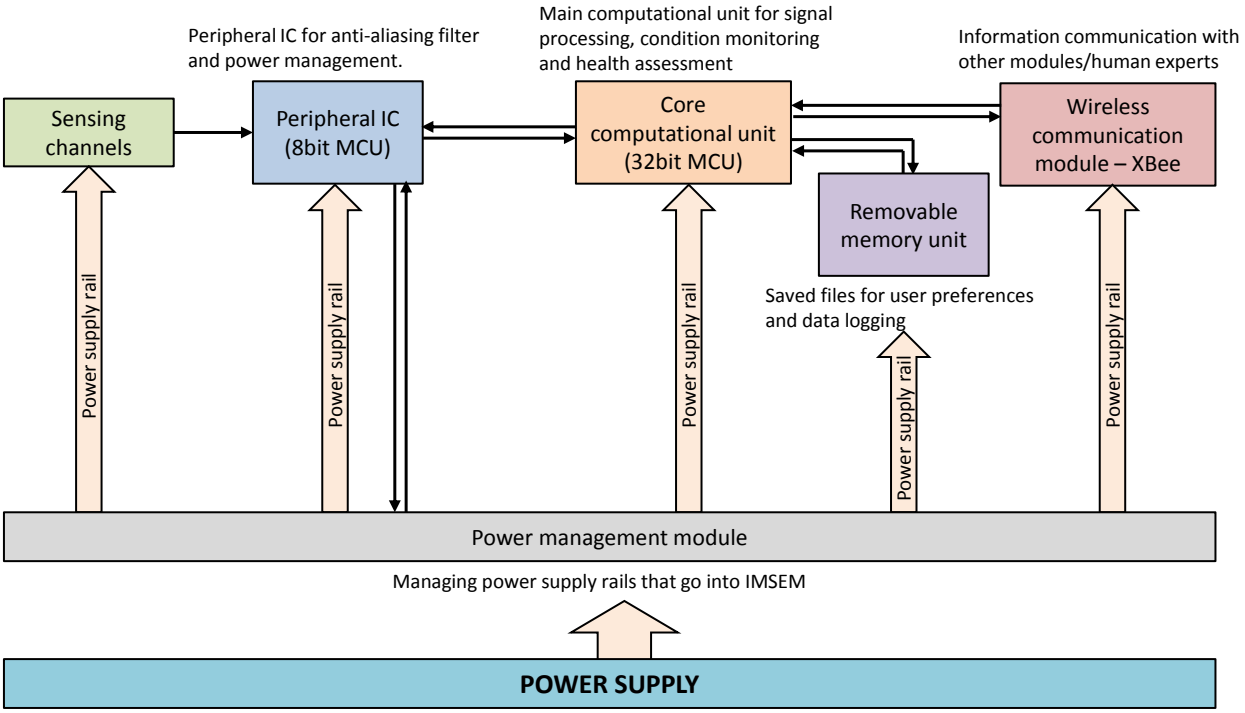

Figure 5-14 Structure of IMSEM as energy consumer module

The respective working prototype of IMSEM is shown in Figure 3-21. There are 6 sub-modules in IMSEM: sensing channels, peripheral MCU, core computational unit, removable memory unit, wireless communication module and power management module. Among them, 5 sub-modules have their power supply being monitored by power management module. To minimise the power consumption, the best option is to completely turn off the sub-modules. However, at least one conventional monitoring should remain at active or partial inactive mode to manage the power rails of sub-modules. Hence, a low-power microcontroller is needed to navigate the power rail to each system modules. The 8-bit MCU plays important role in managing analogue signal conditioning and controlling power rails of other hardware modules, thus turning IMSEM in inactive mode. The 8-bit peripheral

MCU is synced with a 32.768kHz external oscillator, which provides an interrupt signal at every one second. This enables the peripheral MCU to wake up IMSEM at target time period to carry out monitoring task.

5.5.2 Power budget

With developed working prototype, the practical energy budget required by IMSEM could be determined by measuring power consumption in different operation modes. To accurately obtain the power budget profile, the IMSEM is programmed to carry out monitoring task and put into inactive mode. The whole dutycycle will be completed in 1 minute. IMSEM takes 20 seconds to complete signal acquisition, signal conditioning and analysis, fault diagnosis and data logging for 14 seconds. The IMSEM turns into idle mode to check any pending commands to be executed until 20 seconds. If there are no other commands being received, the IMSEM turns into inactive mode for 40 seconds. By integrating HV100F supercapacitor array into the system, the current and voltage characteristics of IMSEM could be illustrated as shown in Figure 5-15. The IMSEM requires average 0.22A when it is in operation mode and only requires 8µA when it is in inactive mode. Such low current consumption could be achieved by turning off all system module and only reserve minimal hardware resources and information in peripheral MCU for time-drive wake up module. The peripheral MCU only consumes 4 µA when it is in sleep mode. Hence, it is expected that most current consumption is contributed by other possible power leakage from the circuit board or electronic component (transistor bank, capacitor, etc.).

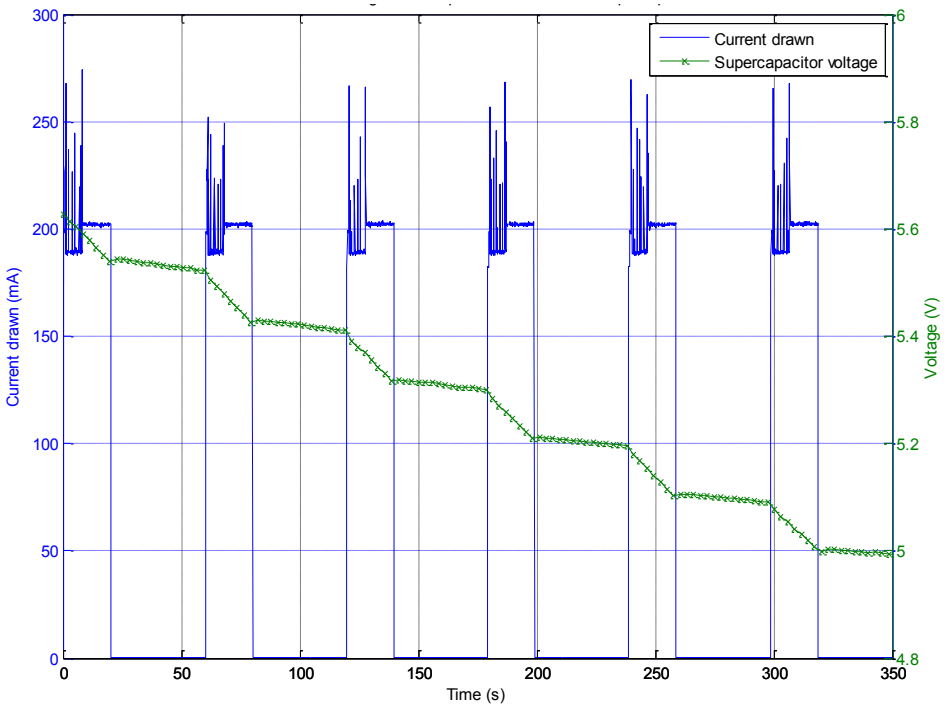

Figure 5-15 Current and voltage characteristics of IMSEM with supercapacitor arrays

The characteristic of current consumption of IMSEM at different modes is illustrated in Figure 5-16. Note that the inactive mode of IMSEM has similar SoDC gradient compared with no supercapacitor voltage with no load. Theoretically, it satisfies the inactive mode of IMSEM and has the ability to conserve most energy storage in supercapacitor, providing longer duration of IMSEM operation cycle. In operation mode, the IMSEM consumes average voltage drop at the gradient of 6.25×10^{-3} V/s. In other words, the supercapacitor has voltage drop of 0.125V during IMSEM's operation mode for 20 seconds.

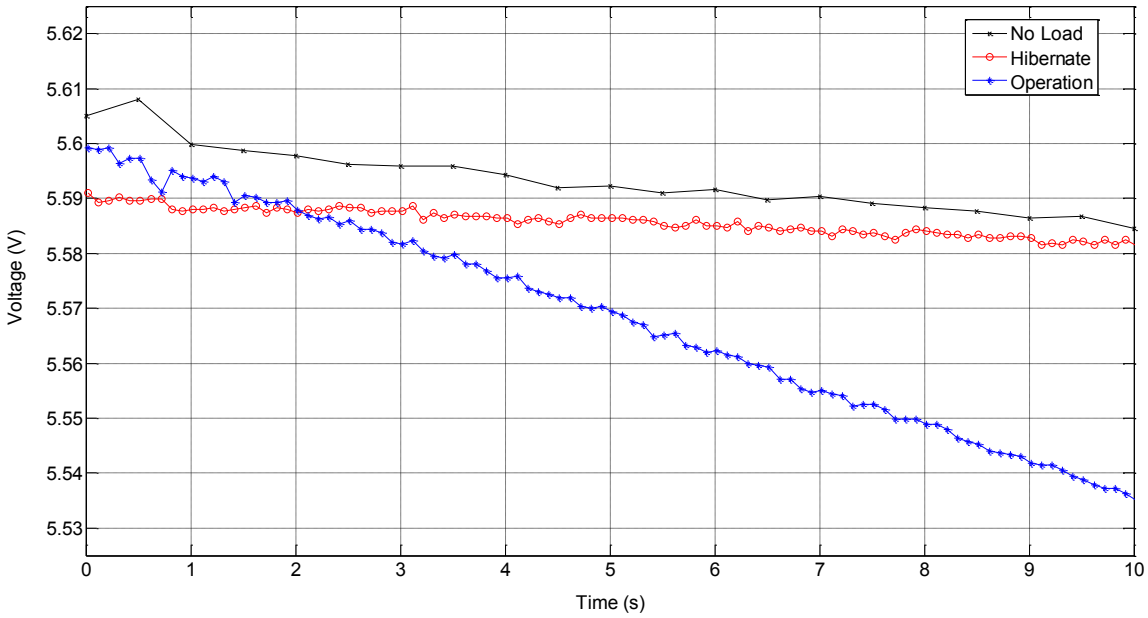

Figure 5-16 Voltage drop characteristics of supercapacitor with IMSEM in different modes

IMSEM requires minimum 4.8V to operate. It stops working when it is below 4.8V. The power budget of IMSEM could be tabulated as shown in Table 5-6.

Table 5-6 Power budget of IMSEM's consumer module

Parameter	Value
Maximum rated voltage (Identified from the system modules' datasheet)	7.5V
Rated voltage	5.6V
Minimum voltage	4.8V
Current drawn (Operation mode)	Average 0.22A
Current drawn (Idle mode)	Average 0.2A
Current drawn (Inactive mode)	8μA
Rated power consumption (Operation mode)	1.232W
Rated power consumption (Idle mode)	1.12W
Rated power consumption (Inactive mode)	44.8μW

5.5.3 IMSEM as active load

The IMSEM acts as a dynamic consumer that functions as a current-stable non-linear load. It draws constant rate current from the power source when the power output is above 1.232W in operation mode. Moreover, the drawn current varies at different stage of dutycycle. Figure 5-15 shows current and voltage characteristics of IMSEM when it is connected to the supercapacitor arrays. The IMSEM starts acquiring signals, save data and send information through wireless module. At this stage, the IMSEM has a stochastic behaviour for its current consumption. To accurately model the power characteristic, a profile of IMSEM's current consumption is extracted from the experimental result. This profile could be used as repetitive signal to emulate the power characteristic of IMSEM in the simulation model. Figure 5-17 shows comparison of simulation and experimental result of current drawn by IMSEM. Their respective behaviours are identical. Experimental result has slight delay which is believed to be caused by the phase error from the 32.768kHz clock oscillator (which controls the service interrupt handler of peripheral MCU). The voltage drop of IMSEM is then simulated and compared with the experimental result, as shown in Figure 5-18. The similar behaviour in voltage drop has proven the accuracy of the simulation model.

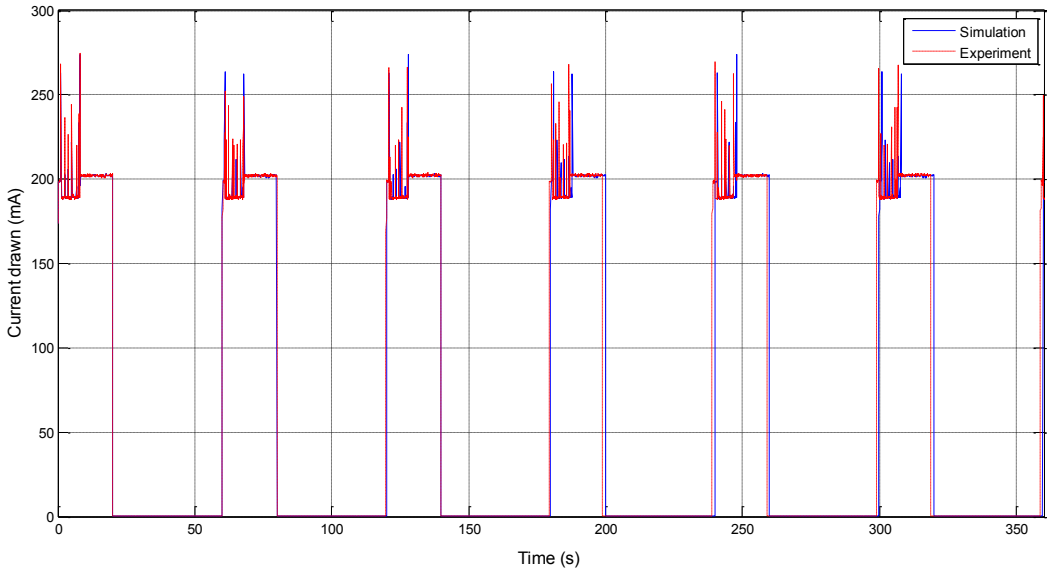

Figure 5-17 Comparison of simulation and experimental result of current drawn by IMSEM

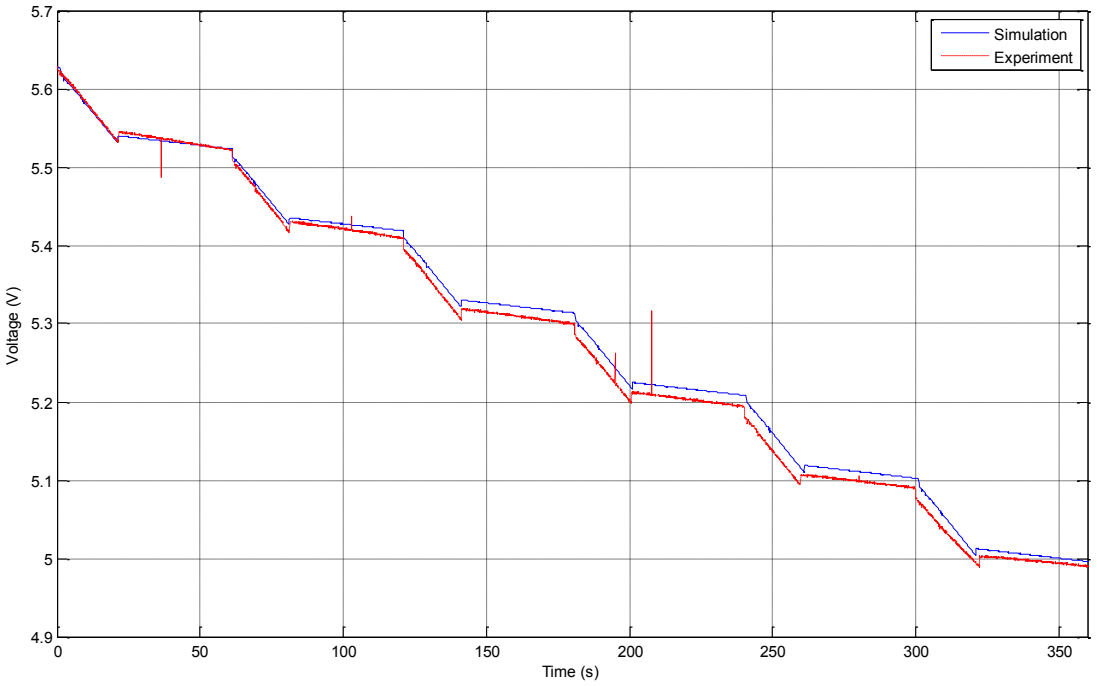

Figure 5-18 Comparison of simulation and experimental result of voltage drop of IMSEM

5.6 Summary

This chapter has presented an intelligent system for MCM with integrated energy-aware module. The system architecture is partitioned into 3 modules: energy harvesting, energy storage and energy consumer module to establish an energy aware IS. The performance of the system is evaluated through simulations and experimental tests. To preserve maximum energy, a periodic monitoring approach is presented to carry out monitoring task within assigned time interval. The performance of energy harvesting (PV cell), energy storage (Supercapacitor array) and energy consumer (IMSEM's computation core) are analysed in detail. From the analysis, the PV cell has the capability to generate sufficient current for the energy storage module. With high energy storage efficiency of supercapacitor array, it is able to store current for energy consumer module. Experiment and simulation results show that it requires at least 4.8V to power up IMSEM. For energy consumer, it draws average 0.22A and 8µA during active and inactive mode respectively. The low current consumption in inactive mode provides spare time to charge up the IMSEM.

IMSEM has the ability to perform at such low PV current, where 10mA could be easily harvested from the light irradiance on the ceiling. The IMSEM has the potential to scavenge energy from outdoor global solar irradiance, where its voltage level could be maintained above 4.8V to prevent system's shut down. However, the energy storage module has insufficient power to maintain the IMSEM at night time. Hence, alternative or secondary energy buffer module, such as the implementation of back-up battery should be taken into account in the future design.

Chapter 6
Results and discussion

This chapter discusses the practical deployment of working prototype to carry out machinery condition monitoring on rotating machines. Two test-beds are used in the research work: DC motor test rig to simulate rotor unbalance fault and 1.1kW 3-phase induction motor test rig to simulate phase imbalance. With the developed intelligent algorithm within core computational unit, the intelligent sensor has the ability to detect faulty signals after undergoing a series of training datasets. The energy efficiency of developed system is also discussed. The result illustrates the developed system has the ability to undergo harsh energy harvesting condition.

6.1 Overview

This chapter elaborates the practical deployment of IMSEM in autonomous MCM. There are experimental test-beds being carried out: rotor unbalance on DC motor and phase imbalance on 1.1kW 3-phase induction motor. To carry out proper experimental test, the performance of MEMS sensor for vibration monitoring is firstly evaluated. Its respective signals are then evaluated and compared with conventional accelerometer. Secondly, the data acquisition module of IMSEM is then compared with the commercial data acquisition system by National Instruments, namely NiDAQ. After the system validation with conventional system, IMSEM is then implemented on DC motor test rig and 1.1kW 3-phase induction motor test rig to carry out MCM task. Diagnostic results are then compared with the reference data result to evaluate the robustness of the intelligence of IMSEM.

To evaluate the energy efficiency, a complete simulation model is developed to analyse the charge and discharge characteristics of IMSEM. With simulation result being validated with series of experiments, the feasibility of IMSEM with energy harvesting module is discussed based on two energy harvesting environment: scavenging energy from constant source and global solar irradiance.

6.2 Performance validation of MEMS sensor

6.2.1 Calibration of MEMS accelerometer

The first step for critical evaluation of the developed system is to calibrate its main vibration transducer, the ADXL001-70 MEMS accelerometer. An accelerometer calibrator type-4291 by Brüel & Kjær is used to excite a reference mechanical vibration at 10.0ms^{-2} peak ±2% with 79.6Hz. Figure 6-1 shows the actual experimental setup of ADXL001-70 being attached on the accelerometer calibrator type-4291. The approximate mass of ADXL001-70 with mounting stud is 27.5g. The calibration result is tabulated in Table 6-1. The acquired signals are plotted in

Figure 6-2. Figure 6-2(a) shows the acquired vibration signal when it is at 0g. Due the single polarity of voltage characteristic, ADXL001-70 has a DC offset at average 2.5V, which is agreed with the datasheet. Such DC offset shall be eliminated when converting signals into FFT to avoid high peak at 0Hz. Figure 6-2(b) shows a constant mechanical excitation at $10ms^{-2}$ with 79.6Hz. The power band at frequency domain lies at 80Hz, satisfying the frequency response of ADXL001-70. Based on the calibrated results, the ADXL001-70 gives relatively good response at the referenced mechanical excitation, which deviates at only 1%.

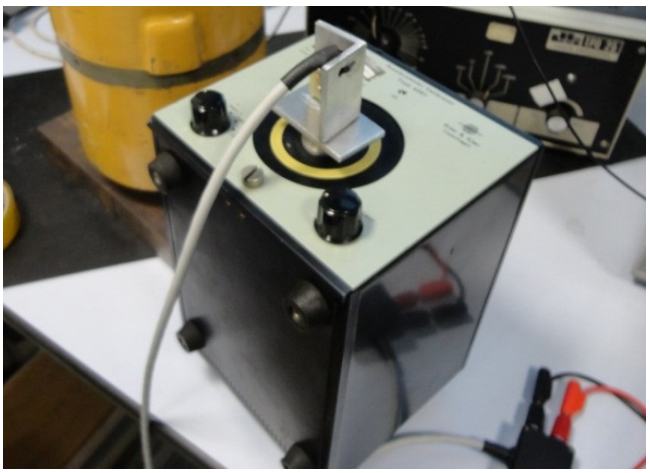

Figure 6-1 Accelerometer Calibrator with mounted ADXL001-70

Table 6-1 Calibrated result of ADXL001-70

Specification	Parameter	
	0Hz, $0ms^{-2}$ peak	79.6Hz, $10ms^{-2}$ peak
Average voltage, V_{avg}	2.62V	2.64V
Peak-peak voltage, V_{pp}	200mV	800mV
RMS voltage, V_{rmsA}	2.66V	2.62V
Dominant frequency, f_A	0Hz	80.4Hz (1% deviation)

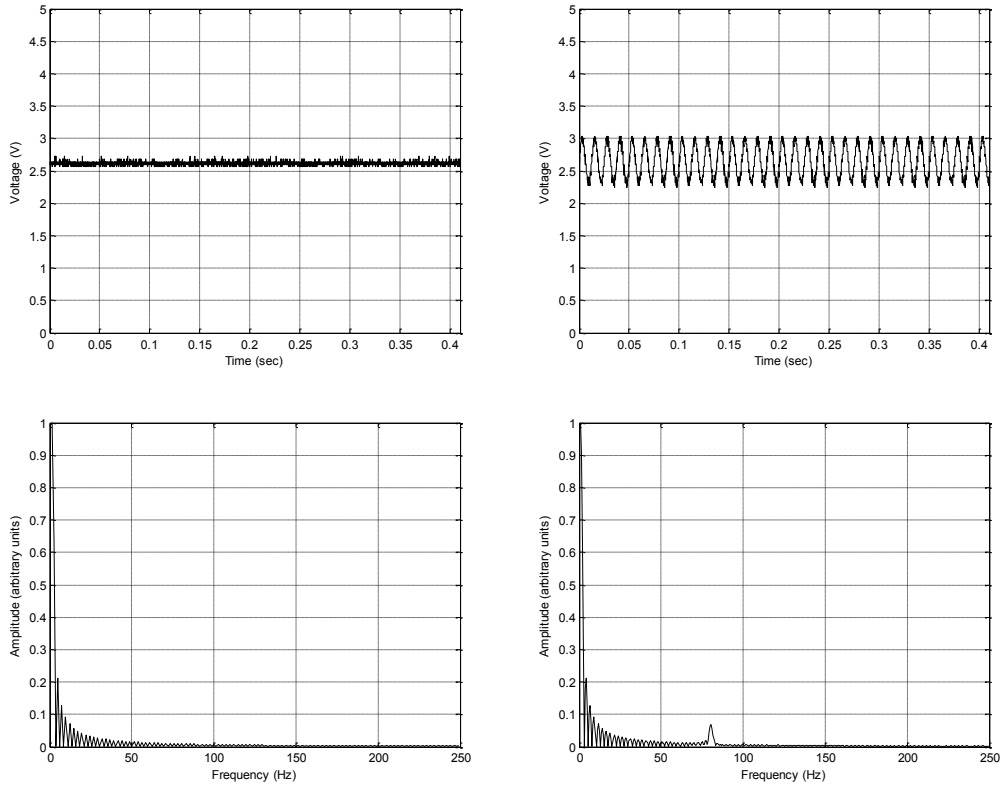

(a) (b)

Figure 6-2 Calibrated vibration waveform of ADXL001-70: (a) 0Hz, 0ms^{-2}, (b) 79.6Hz, 10ms^{-2}

6.2.2 Validation with conventional data acquisition system

In this section, a conventional Brüel & Kjær piezoelectric accelerometer and NiDAQ is used as a reference system to validate the performance of ADXL-001-70 connected with IMSEM. Figure 6-3 shows the experimental setup of the IMSEM validation system. Both accelerometers are attached on the mechanical shaker, which excites at different frequency and amplitude. The mechanical shaker is set to oscillate at 50Hz. For IMSEM and NiDAQ, their respective sampling frequencies are set to 5kHz. To analyse their similarities, both signals are transformed into power spectral density as depicted in Figure 6-4. Note that both the power spectrums have their peak values at 50Hz, which comply with the dominant mechanical frequency

from the shaker. For further analysis, the coherence, $C_{xy}(f)$ between two vibration signals could be established as [131]:

$$C_{xy}(f) = \frac{|G_{xy}(f)|^2}{G_{xx}(f)G_{yy}(f)} \tag{6-1}$$

Where $G_{xy}(f)$ is the cross-spectral density between signal x and y. $G_{xx}(f)$ and $G_{yy}(f)$ are the auto-spectral density of signal x and y respectively. Coherence is used to quantify the degree of correlation of two input signals. It is a normalised coefficient value between 0 to 1 whereby the closer the value to 1, the more identical of two signals at particular frequency instance. The coherence of the measured signals using both ADXL001-70 and conventional accelerometer is shown in Figure 6-5. It has the highest correlated coefficient when the frequency is close to 50Hz. This shows that both sensors have successfully obtained the important dominant frequency information. The magnitude for harmonic frequencies between the two signals deviates when the frequency is getting larger (100Hz and 150Hz). It could be due to the position of attachment of the sensors. The high coherence values at several important frequencies (dominant and harmonic frequencies of mechanical shaker) have proven the feasibility of ADXL001-70 in providing robust measurement for MCM.

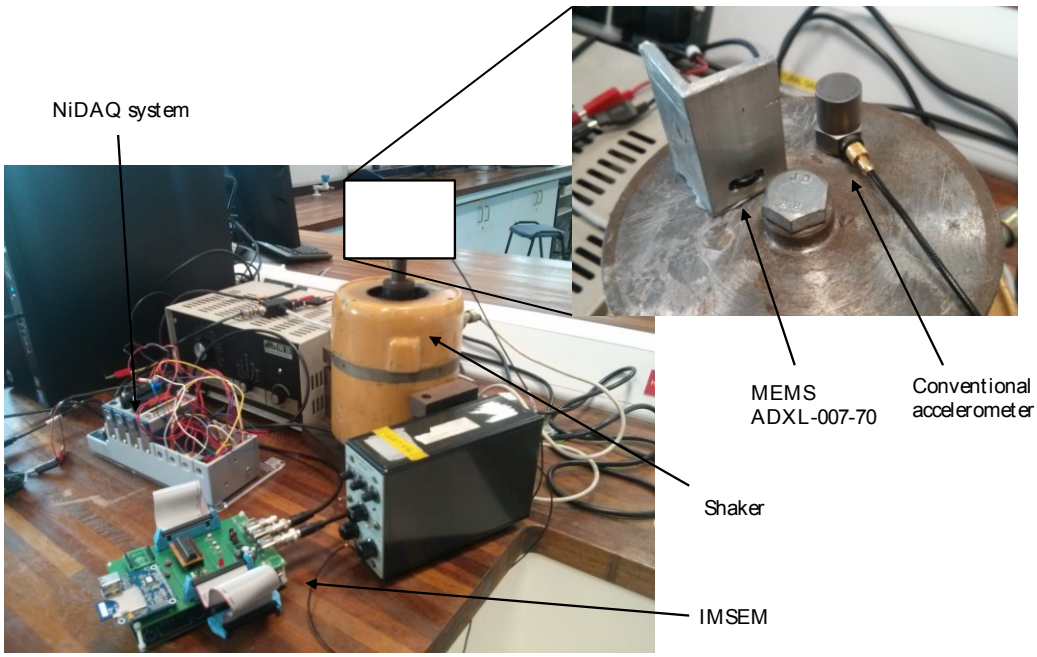

Figure 6-3 Experimental setup for validation of ADXL-001-70 with IMSEM

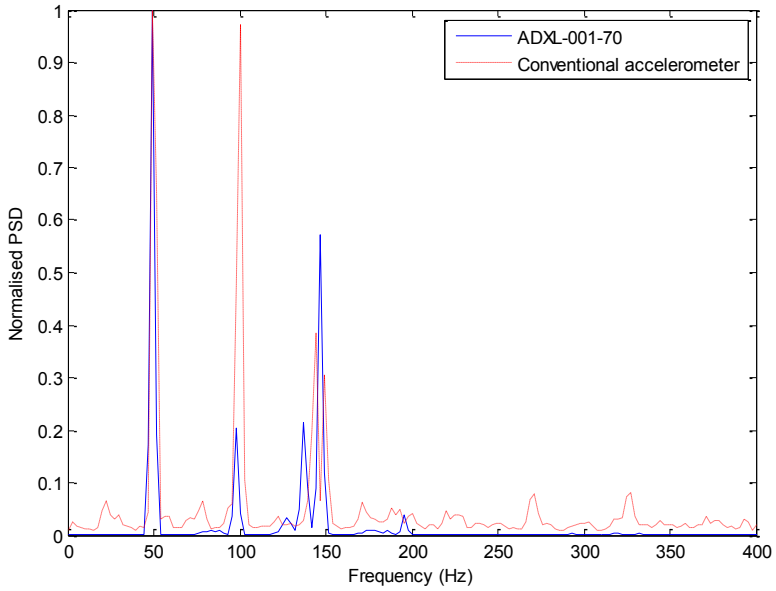

Figure 6-4 Frequency spectrum of acquired vibration signal using ADXL001-70 and conventional accelerometer at 50Hz

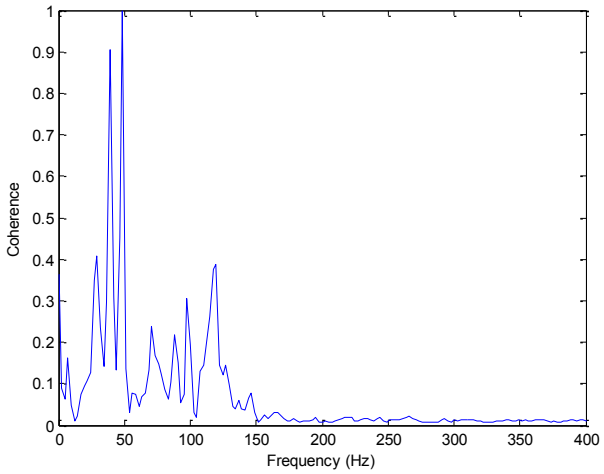

Figure 6-5 Coherence between the vibration signal acquired using ADXL001-70 and conventional accelerometer

6.3 Rotor unbalance detection and diagnosis

6.3.1 Experiment setup

The experimental setup for fault diagnostics on DC motor test rig is illustrated in Figure 6-6. The MEMS ADXL-001-70 is attached at the top of the housing area, while the Hall-effect sensor is located at the side of rotating disc. The diameter of the rotating disc is 0.072m, weighing 2kg. The DC motor test rig is configured in a constant (rigid) state, whereby its corresponding health condition could be evaluated using international standard, namely ISO1940-1:2003. There are 2 possible diagnostic results present throughout the monitoring process: {healthy, alarm}.

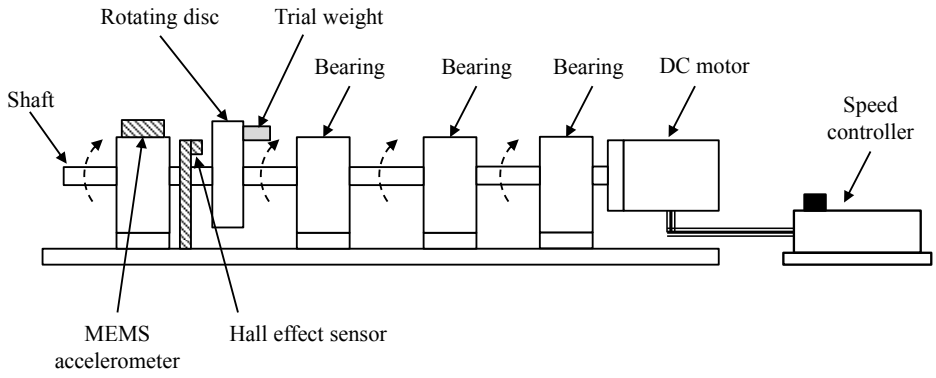

Figure 6-6 DC motor test rig with MEMS accelerometer and Hall-effect sensor

6.3.2 Determining rotor unbalance threshold using ISO 1940-1

To validate any vibration monitoring system; it is essential to accurately establish the permissible residual unbalance using an approved standard such as ISO 1940-1:2003[4]. In ISO 1940-1:2003. The balance quality grades for various machines are outlined, known as G. The grade G is a product term of specific unbalance, e and the angular velocity at maximum speed, ω:

$$G = e \times \omega \tag{6-2}$$

In practice, the grade G could be defined based on the guidelines provided by ISO 1940-1:2003, as tabulated in Table 6-2. The permissible residual unbalance, U_p (measured in g·mm), on the other hand, can be computed using:

$$U_p = 9549 \times G \frac{m_r}{W} \tag{6-3}$$

Where m_r is the rotor mass in kg and W is the maximum rotating speed in rpm. The ISO 1940-1:2003 standard can be illustrated as shown in Figure 6-7.

Table 6-2 Extracted guidance for balance quality grades for rotors in a constant state [132]

Machinery types: General example	Balance quality grade, G
Crankshaft drives for large slow marine diesel engine (piston speed below 9m/s), inherently unbalanced	4000
Crankshaft drives for large slow marine diesel engines (piston speed below 9m/s), inherently balanced	1600
Crankshaft drives, inherently unbalanced, elastically mounted	630
Crankshaft drives, inherently unbalanced, rigidly mounted	250
Complete reciprocating engines for cars, trucks and locomotives	100
Agricultural machinery, crankshaft drives, crushing machines, drive shafts (cardan shafts, propeller shafts)	16
Electric motors and generators (of at least 80mm shaft height), of maximum rated speed up to 950rpm	6.3

[4] International standard 1940-1:2003 Mechanical vibration – Balance quality requirements for rotors in a constant (rigid) state. This standard has been reviewed and confirmed in 2013. [Online] Available: www.iso.org [Accessed Mar-2015]

Electric motors and generators (of at least 80mm shaft height), of maximum rated speed above 950rpm	2.5
Audio and video drives	1
Gyroscopes, spindles and drives of high-precision systems	0.4

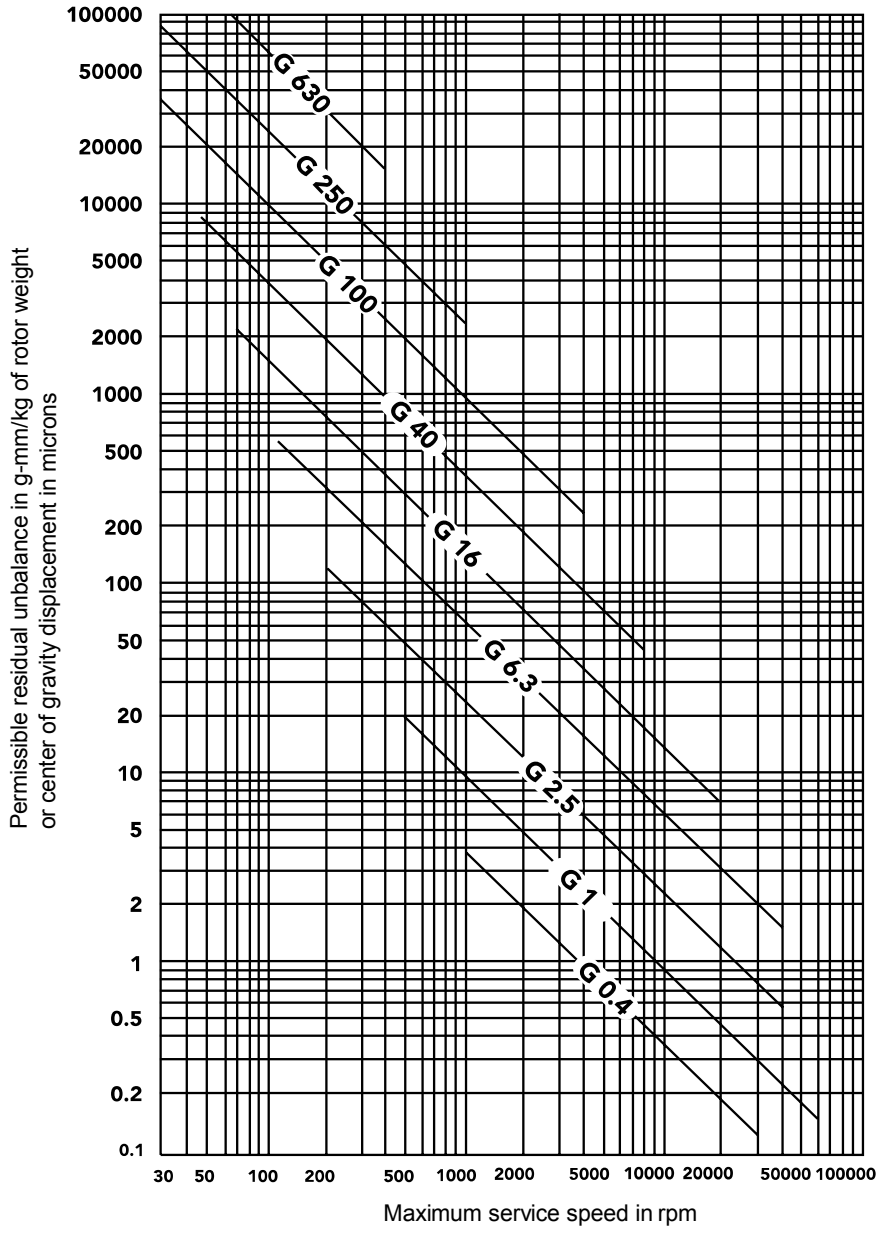

Figure 6-7 Maximum permissible residual unbalance, e_p (adapted from ISO 1940-1:2003)

The experimental DC motor test rig has a rated rotating speed of up to 2000rpm. The balance quality grade of 2.5 is used to determine the permissible residual

unbalance of the motor test rig. The trial weight is loaded on the axial plane of the rotating disc. In the balancing theory, the unbalance coefficient, U_p can be determined by establishing the trial mass, m_t and distance from unbalance to the centre of rotation axis, d: $U = m_t \times d$. This serves as a benchmark to detect the faulty condition of a DC motor test rig. The threshold for training data is identified as based on the calculated U_p.

The DC motor allows to carry out fault diagnosis on rotor unbalance under variable rotating speeds. The MEMS accelerometer is placed at the bearing housing, whereas the Hall-effect sensor is placed at the side of the rotating disc, as shown in Figure 6-6. Moreover, 63 sets of data are taken with trial weights under the rotating speed. The first 25 sets are used to train the data fusion model, whilst the other 38 sets are used for testing. The data is saved under an XML format or can be transmitted in a simplified format with user commands. The performance and monitoring results are discussed in section 6.3.3.

6.3.3 Results and discussions

The alarm threshold level is firstly specified according to ISO 1940-1:2003 standard. Figure 6-8 shows the threshold levels under different rotating speeds. In this experiment, different trial weights: 1.87g, 3.42g, 4.45g, 5.48g, 6.52g and 17.16g are attached to the rotating desk. The rotor unbalance and its residual permissible threshold are computed using equations (6-2) and (6-3). The solid line classifies the threshold region: The region above the solid line presents the residual unbalance coefficients while the region below the solid line presents the healthy region. The dotted horizontal lines present the machinery condition with different loads and speeds. The dotted lines of 1.87g, 3.42g, 4.45g, 5.48g, 6.52g and 17.16g fall into the healthy region when the rotational speed is low. This clearly satisfies the statement in ISO 1940-1:2003: Lower rotational machines have higher permissible residual unbalance.

A total of 63 sets of vibration and Hall-effect signals are acquired for training and testing purpose (11 sets of healthy data and 52 sets of faulty data). Amongst these, 25 sets of data are used for generating the SVM classification model. All datasets have their respective rotor unbalance calculated for training and evaluation purpose.

The vibration signals of acquired datasets are shown in Figure 6-9. These vibration signals are then transformed to frequency domain using a 2048-point FFT. It should be noted that the power spectrum peak increases in higher load and speed. The digital signals from Hall-effect sensor are acquired for accurate rotating speed determination. The Hall-effect sensor is configured in an active-high mode, giving a low signal pulse when a magnetic object is approaching the sensing terminal. In this experiment, one digital pulse is given out in one rotating cycle. Hence, the rotating speed can be accurately calculated by multiplying the digital signal period with the sampling frequency of IMSEM, f_s.

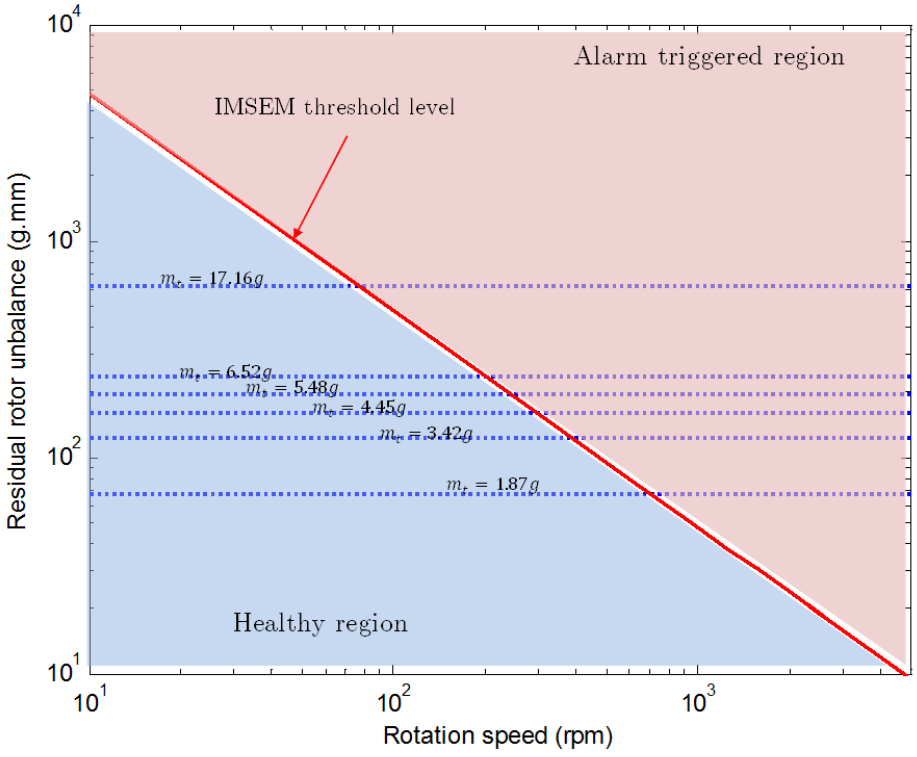

Figure 6-8 Rotor unbalance threshold over trial weights based on ISO 1940/1. The permissible threshold level decreases when rotational speed increases.

With an in-built LIBSVM, the classification computation is completed in 17 iterations. After the experiment, the IMSEM reached an accuracy of 94.74%, where 36 out of 38 data sets are predicted correctly. This performance is compared with the SVM classification with RBF kernel using a computer. Both sets of data have the same accuracy of 94.74%, as tabulated in Table 6-3. The training and test samples are mapped onto the ISO1940-1 guidelines, as shown in Figure 6-10. The accuracy error is expected from the classification over-fitting due to the stochastic characteristics of mean and kurtosis components. In Figure 6-11, it is obvious that rms, standard deviation and peak have greater impact than mean and kurtosis statistically. These 3 feature components provide a relatively linear response with respect to the increased unbalance and speed. By removing the mean and kurtosis from the feature component list, the IMSEM reached an accuracy of 100%.

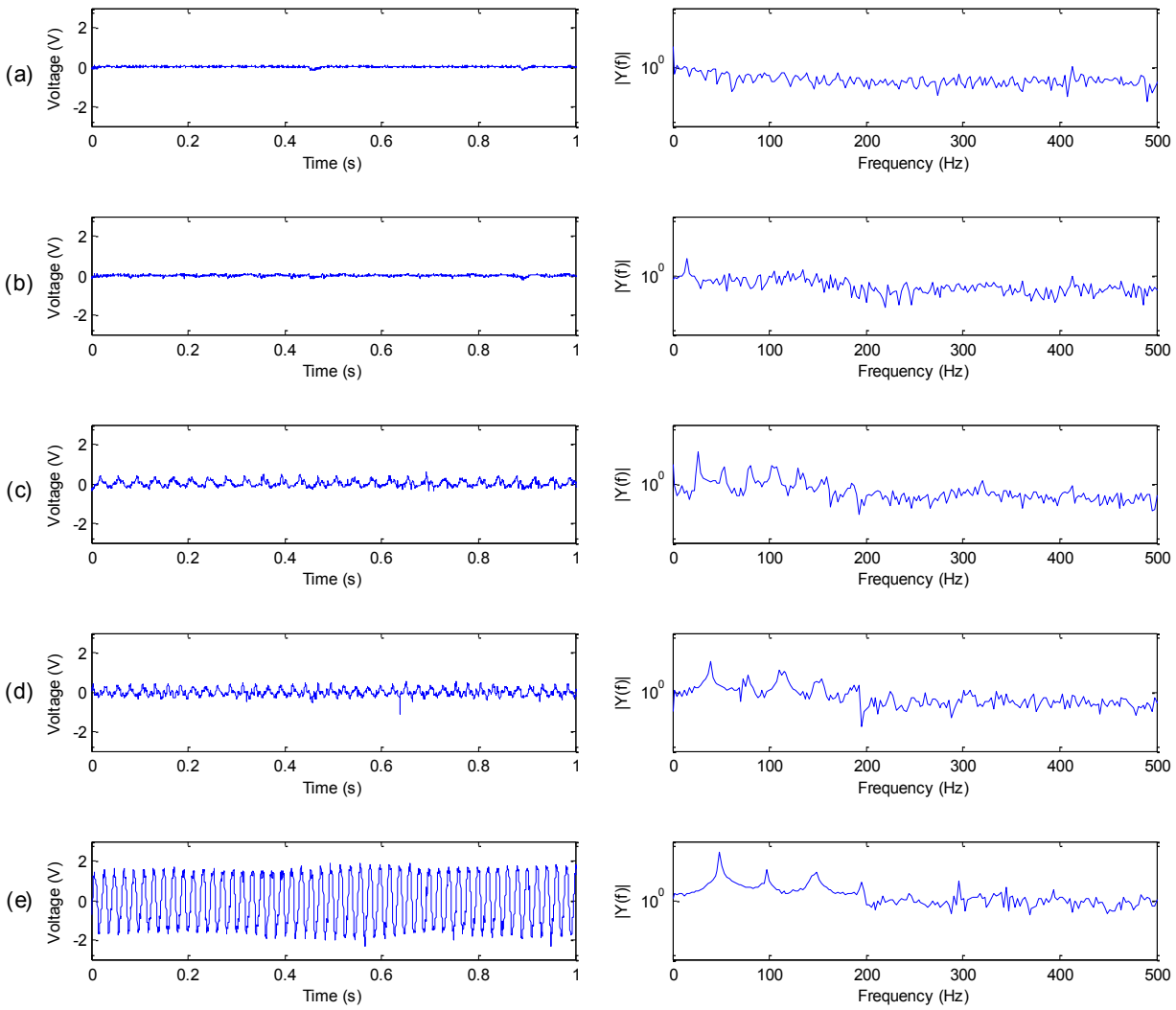

Figure 6-9 Vibration waveforms and power spectrum of acquired signals from IMSEM at different rotating speed: a) 280rpm, b) 914rpm, c) 1602rpm, d) 2281rpm and e) 2864rpm

Table 6-3 Comparison of kernel type for SVM classification – DC motor test rig

Type of kernel	Linear (IMSEM)	RBF (Computer)
Iteration of computation	17	15
Correct fault detection	36 out of 38	36 out of 38
Accuracy	94.74%	94.74%

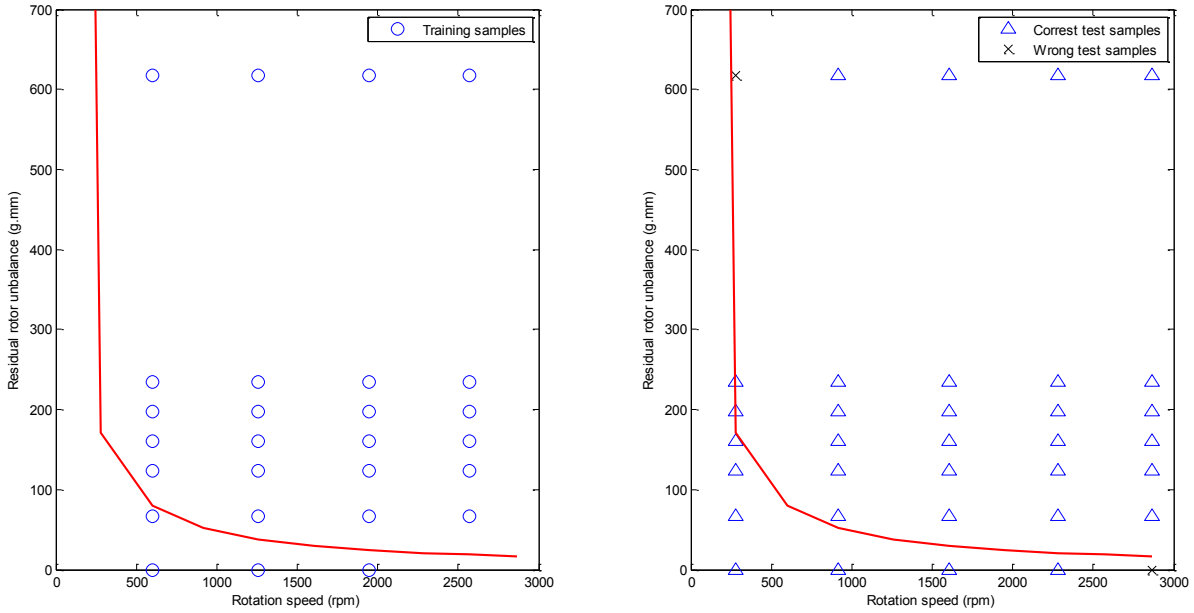

(a) (b)

Figure 6-10 Mapping of (a) training and (b) test samples on ISO1940-1 guideline

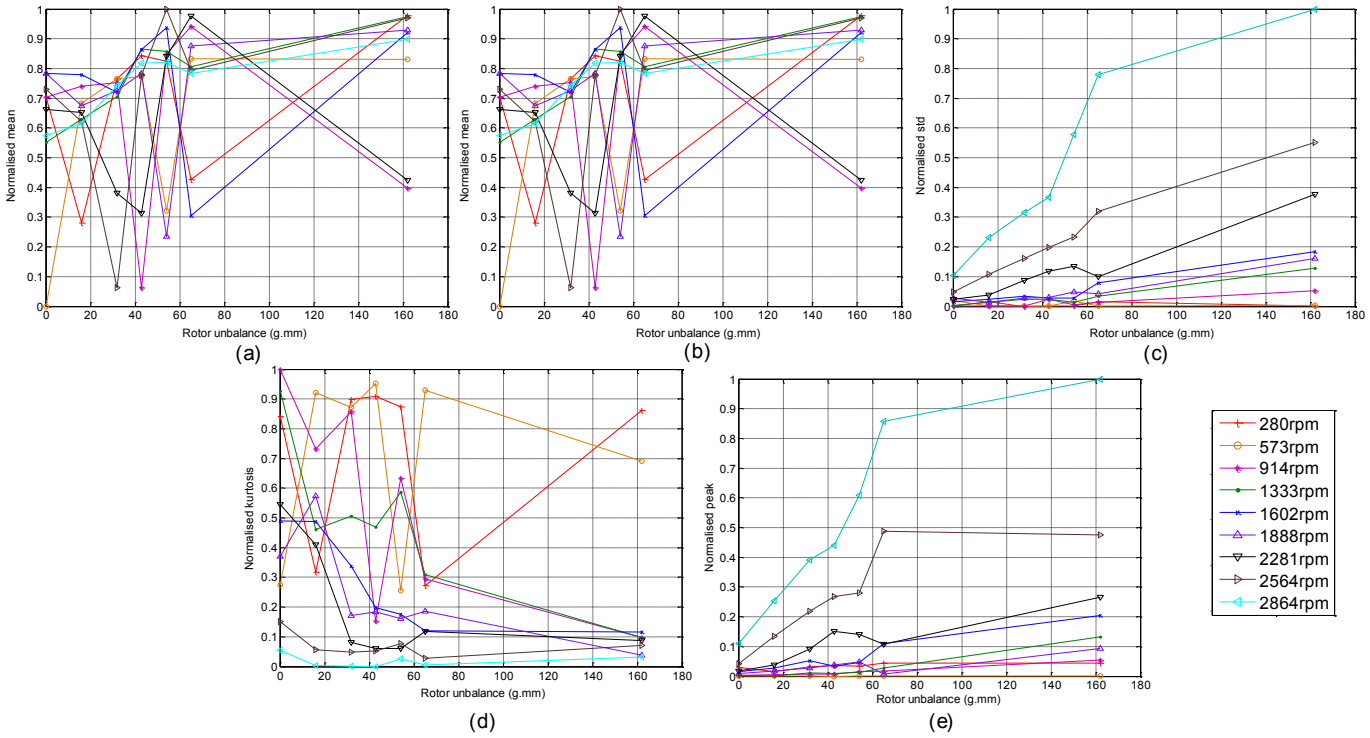

Figure 6-11 Feature components with different rotor unbalance and speed: (a) mean, (b) rms, (c) standard deviation, (d) kurtosis, (e) power spectrum peak

6.4 Fault diagnostics on phase imbalance of 3-phase induction motor

6.4.1 Experiment setup

Electrical equipment, especially motors and their controllers, will not operate reliably on unbalanced voltage in a 3-phase system. Greater imbalances might cause overheating and sudden tear-down of rotating machinery, which are not desirable in practical industries. As a rule of thumb, the temperature of the motor rises by 25% for every 3.5% voltage imbalance [133]. In this test, a 1.1kW 3-phase induction motor test rig allows to control voltage imbalances. An ideal 3-phase induction motor presents 3 equal magnitude voltage phasor at 120°. By changing the external resistance, it is able to control imbalances to be induced by voltage drop on single-phase. Since the 3-phase induction motor remain at the same speed, the signals provided by Hall-effect sensor is omitted from the following analysis. The ADXL001-70 is attached on the squirrel cage of induction motor, as shown in Figure 6-12.

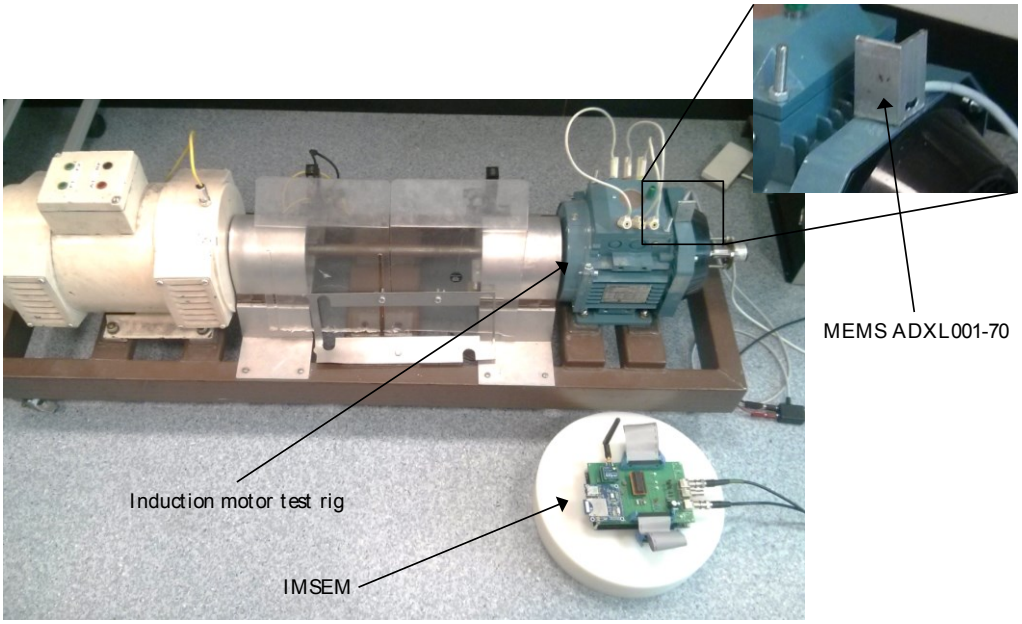

Figure 6-12 Experimental setup on 3-phase induction motor

6.4.2 Determining phase imbalance under different load condition

According to National Electrical Manufacturers Association (NEMA) standard MG 2-2001, motors are designed to operate within 10% voltage variation [134]. However, this characteristic is based on no load conditions. The motor has different levels of tolerances when it is under different load condition. Previous researchers in the research group found that the motor test rig will operate without noticeable impediment for an imbalance of 8.3% at zero-load and motor being tripped (due to in-built thermistor protection) after 90 minutes of operation [38]. To test the developed working prototype, the baseline for triggering the diagnostic alarm is set to 6%. Similar to previous experimental work, there are two classifications which yields 2 outputs from IMSEM: {healthy}, {alarm}. To accurately determine the voltage imbalance to be induced, line-to-neutral voltage readings across 3 lines are recorded using voltmeter: $V \in \{V_1, V_2, V_3\}$. Found in [135], the following equation could be used to calculate voltage phase imbalance, V_{im} of a polyphase system:

$$V_{im} = \frac{\max(|V - \bar{V}|)}{\bar{V}} \tag{6-4}$$

Where V_{im} is the voltage umbalance rate, which could be expressed in percent by multiplying with 100. $\bar{V}$ denotes the mean average of set V.

For the 1.1kW 3-phase induction motor test rig, the average voltage rms across the 3 lines (Line A, B and C) is: 128V. To generate voltage phase imbalance, only 1 line-to-neutral voltage is altered. Table 6-4 outlines the voltage imbalance in 3-phase induction motor test rig with different power load. Note that with the same configuration, the power loads being applied has contributed slight voltage drop across 3 lines, thus deviating the values of $\bar{V}$ and V_{im}. Since the variation of V_{im} corresponding to power load is small, the value of V_{im} was calculated for the load variation from 0W to 1000W (0%, 25%, 50% and 100% of full load).

Table 6-4 Voltage phase imbalance

Power load (W)	Percent slip across V_1 (%)	V_1 (V)	V_2 (V)	V_3 (V)	$\bar{V}$ (V)	V_{im} in percent (%)
0	0	128	129	129	128.67	0.5181
0	5	121	129	129	126.33	4.22
0	10	115	129	128	124	7.2581
0	15	110	129	128	122.3333	10.0817
0	20	104	129	129	120.67	13.8122
0	25	98	129	129	118.67	17.4157
1000	0	127	128	128	127.33	0.522
1000	5	122	128	127	125.67	2.9178
1000	10	116	128	127	123.67	6.1995
1000	15	110	128	127	121.67	9.589
1000	20	104	128	127	119.67	13.0919
1000	25	98	127	127	117.3333	16.4773

16 sets of vibration data are recorded using IMSEM with several levels of voltage slip across line A (0%, 5%, 10%, 15%, 20% and 25% based on V_1) at different loads (0W, 250W, 500W, 750W and 1000W). The respective V_{im} in percent with V_1 is calculated as referenced value to train and validate the performance of IMSEM. 6 healthy datasets are profiled to the IMSEM, whereby their V_{im} in percent is less than 6%. The mapping of training samples is illustrated as shown in Figure 6-13. To validate the performance of the training model, another 14 sets of data is obtained. Their respective classification output is then evaluated and compared in the next section.

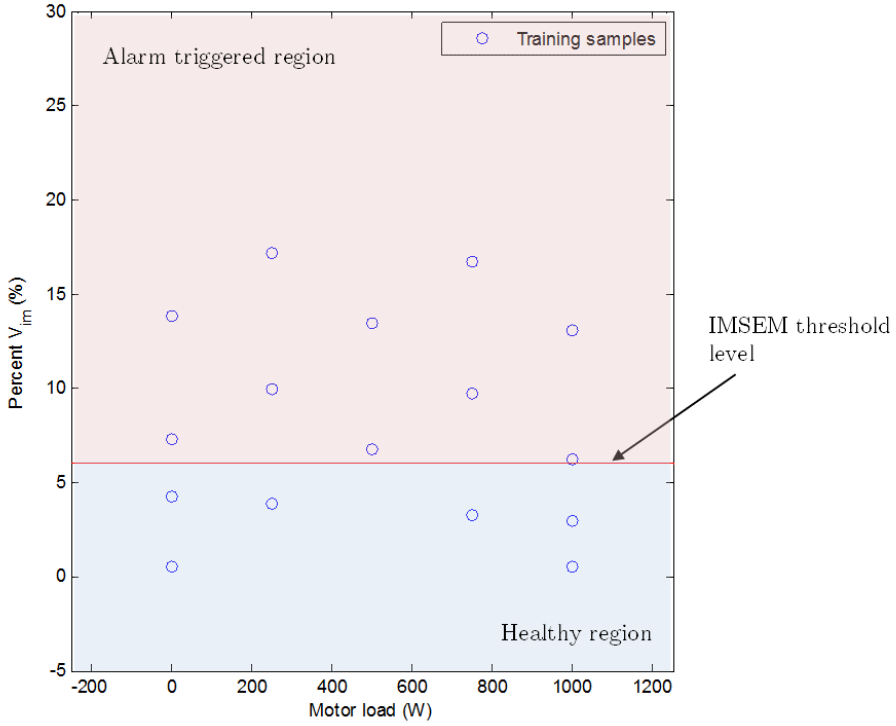

Figure 6-13 Mapping of training samples of IMSEM for voltage imbalance fault diagnostic

6.4.3 Results and discussion

With on-board built-in intelligent algorithms, IMSEM extracted 5 feature components from the measured vibration signals: mean average, RMS, standard deviation, kurtosis and power spectrum peak at dominant rotating frequency. As shown in Figure 6-14, the mean average has stochastic characteristic across the mesh grid of voltage phase imbalance and power loads. Thus, this means that the components have contributed useful information in the SVM algorithm. RMS (Figure 6-15), standard deviation (Figure 6-16) and power spectrum peak (Figure 6-18) have relatively linear characteristic response to the voltage phase imbalance. Whereas kurtosis Figure 6-17 has negative linear characteristic with other feature components. Such relational characteristics are important and significant contributor to the SVM as data fusion layer. However, based on the 5 extracted features, no significant relational characteristics between the voltage phase

imbalance and load is indicated. This causes a difficult issue in classification problem. More suggested work is outlined in section 6.6.

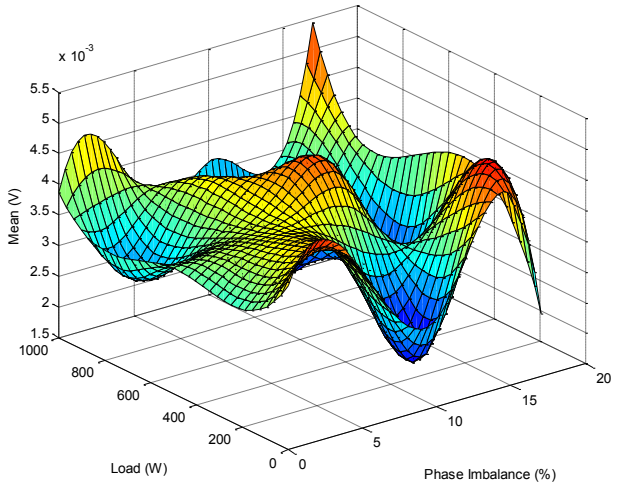

Figure 6-14 Mean components of vibration signals under different loads and percent slip of phase imbalance

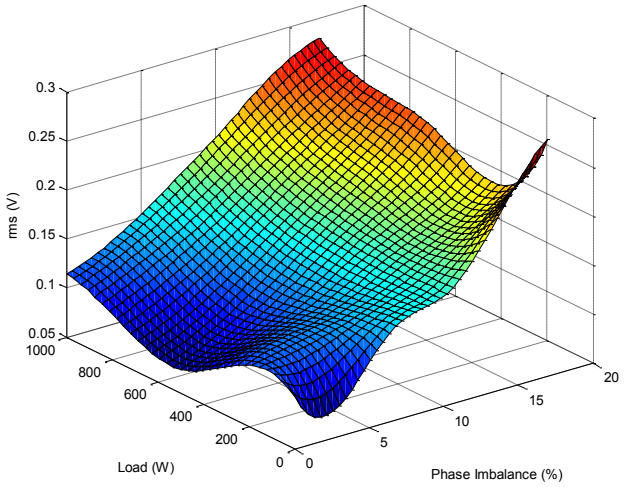

Figure 6-15 RMS of vibration signals under different loads and percent slip of phase imbalance

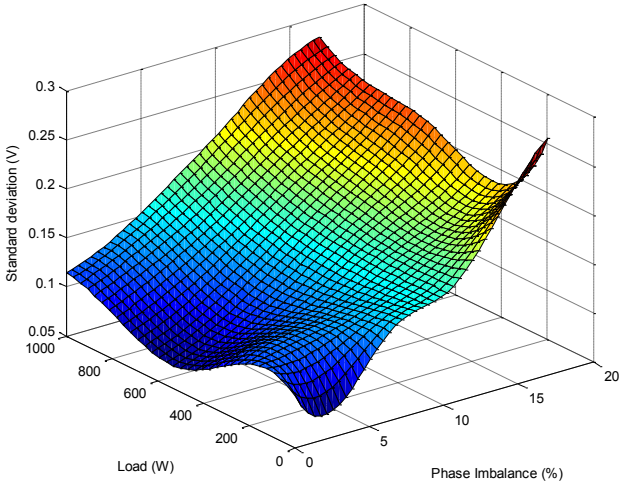

Figure 6-16 Standard deviation of vibration signals under different loads and percent slip of phase imbalance

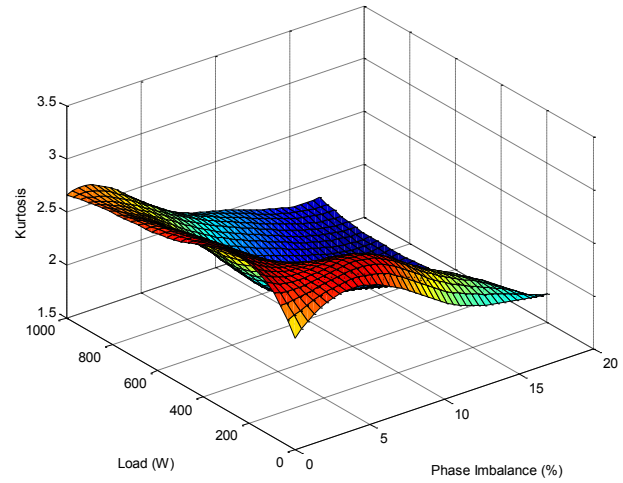

Figure 6-17 Kurtosis of vibration signals under different loads and percent slip of phase imbalance

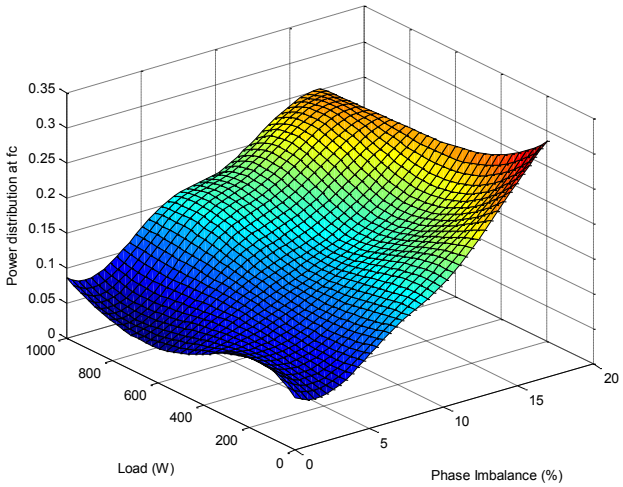

Figure 6-18 Power spectrum peak of vibration signals under different loads and percent slip of phase imbalance

14 vibration datasets are being used to validate the performance of IMSEM on voltage phase imbalance. 4 healthy signals and 8 faulty signals are accumulated. Figure 6-19 illustrated the mapping of test samples at different levels of motor loads and voltage phase imbalances. The performance of IMSEM's SVM (with linear kernel) is compared with the LIBSVM running on desktop computer (RBF kernel). With the training model being established in section 6.4.2, the IMSEM reaches to the accuracy of 92.8571%, which successfully detects 13 sets of voltage phase imbalance datasets (out of 14 datasets). It is believed that with more training samples being projected to the system, IMSEM could reach better diagnostic performance. On the contrary, the computer has lower accuracy in this experiment. It might be due to the unsuitable type of kernel being used in this classification problem.

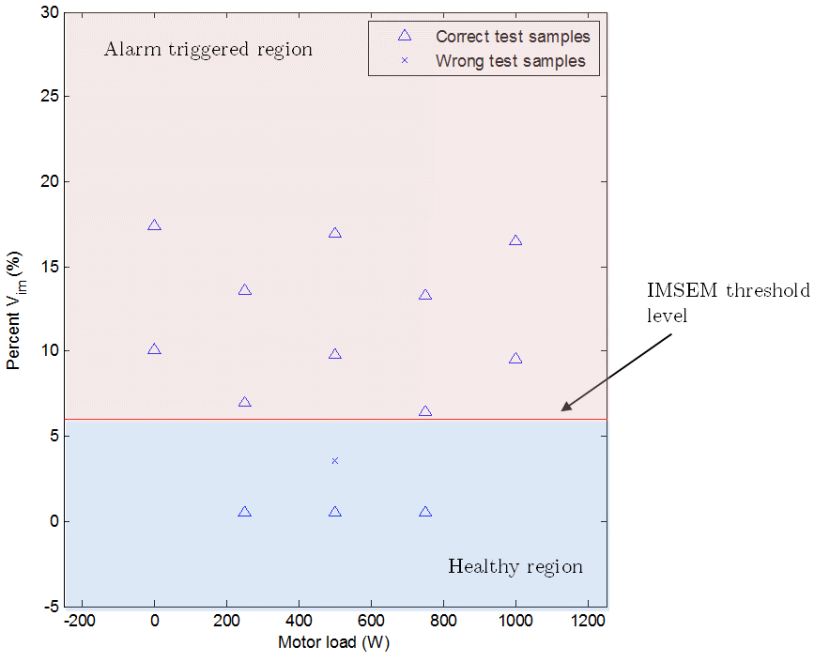

Figure 6-19 Mapping of testing samples of IMSEM for voltage imbalance fault diagnostic

Table 6-5 Comparison of kernel type for SVM classification – 3-phase induction motor

Type of kernel	Linear (IMSEM)	RBF (Computer)
Iteration of optimisation	14	12
Correct fault detection	13 out of 14	12 out of 14
Accuracy	92.8571%	85.7143%

6.5 Energy budget analysis

In this section, experiments are conducted to determine the harvestable amount of energy from both an artificial light source and natural solar irradiance. The light source in the laboratory produces constant solar luminance while the natural solar irradiance has intermittency depending on weather condition, daylight and other atmospheric effects. To evaluate the power characteristics, the IMSEM is set to have its operational duty cycle at every one hour, establishing a periodic monitoring system with $k = 24$ a day. Similar to equation (5-30), the energy produced within timeslot n can be expressed as:

$$E_h(n) = E_{h1}(n) + E_{h2}(n) = \int_t^{t+T} P_h(n)dt\,, T = T_1 + T_2 \quad (6\text{-}5)$$

Where E_h and P_h represent the harvested energy and power from energy source module, respectively. E_{h1} and E_{h2} are harvested energy within the time duration of T_1 and T_2. In this experiment, the duration for the time slot is $T = 3600s$ ($T_1 = 20s$ and $T_2 = 3580s$).

A simulation model is developed to analyse the performance of IMSEM with different solar energy input (insolation), as depicted in Figure 6-20. There are two inputs for current source which is used to control constant charge current (constant light source) and variable charge current (generated current from global solar irradiance). The switch is implemented to control different current sink by IMSEM in two modes (active and inactive). The activation threshold is used to simulate the inactivation of IMSEM when the voltage level is below 4.8V, thus resulting insufficient voltage to power up IMSEM. The simulation model has been validated for its accuracy as presented in Figure 5-12, Figure 5-17 and Figure 5-18.

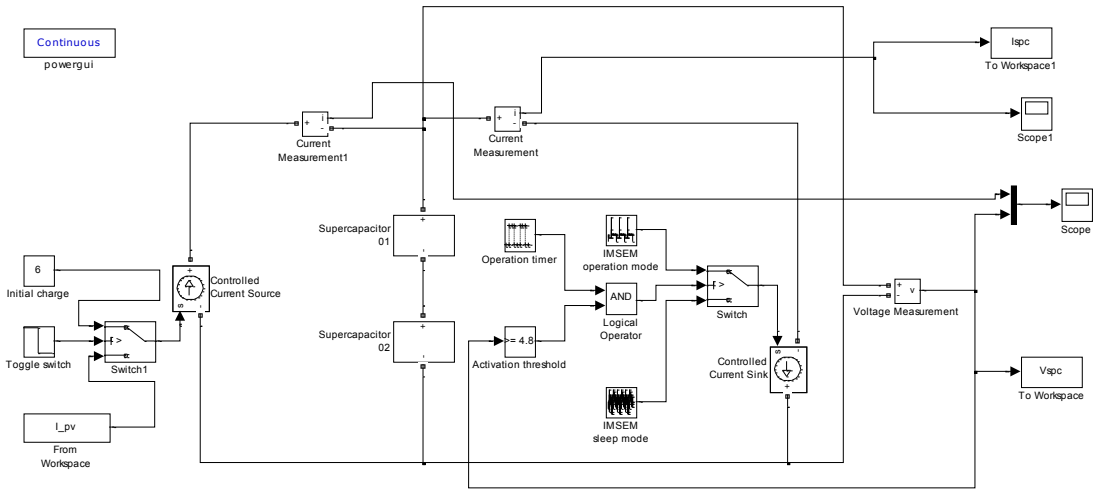

Figure 6-20 Complete Simulink model of IMSEM with supercapacitor array and PV generated current

6.5.1 Scavenging energy from artificial light source

As tabulated in Table 5-6, the power characteristics of IMSEM have been well determined. To prevent IMSEM from being shut down, the constant lighting source should produce enough energy to charge up the energy buffer module (supercapacitor array) of IMSEM. Since the gradient of voltage drop during operational dutycycle is 0.125V, the system should maintain the voltage level at 4.925V before the operation mode is activated. In inactive mode, the energy source module should produce sufficient utilisable stored energy, E_u to prevent discharge. The mathematical term of E_u could be expressed as:

$$E_u(n) = E_h(n) - E_{dc}(n) - E_{sdc}(n) \quad (6\text{-}6)$$

Where E_{dc} and E_{sdc} represent discharge and self-discharge characteristic of supercapacitor array. The sign of E_u determines the store efficiency of energy storage module. If $E_u(n) > 0$, it represents the surplus harvested energy which could be stored in the energy storage module. If $E_u(n) < 0$, it represents the insufficient harvested energy to keep positive energy gradient of IMSEM, thus suffers voltage drop.

3 different datasets of constant lighting sources have been used to test the performance of IMSEM. Their charging characteristics of IMSEM with constant lighting sources are tabulated in Table 6-6.

Table 6-6 SoC characteristics of IMSEM with constant lighting source

Solar illuminance (lux)	Solar irradiance (W/m^2)	Generated PV current, I_{pv} (A)	Average generated power, P_h (W)	Generate energy within T_1, E_{h1} (J)	Generate energy within T_2, E_{h2} (J)
770×100	700	0.402	2.412	48.24	8.635k
170×10^2	260	0.142	0.852	17.04	3.05k
31×10^2	80	0.043	0.258	5.16	923.64

The energy storage has initial capacitor voltage of 0.05V. It is then connected to the energy source module to charge its voltage to 4.8V, reaching the minimum threshold of IMSEM's activation. The PV cell is set to provide 6V to prevent excessive voltage input that might damage the energy storage module. Based on the energy consumption extracted from Figure 5-15, $E_{c1} = 28.1058J$ and

$E_{c2} = 1.3907J$. Their average power consumptions are $P_{c1} = 1.4053W$ and $P_{c2} = 1.6128W$. The value of E_s is voltage-dependent which could be determined by analysing the self-discharge characteristic under no load condition. Figure 6-21 shows the supercapacitor self-discharge characteristic within 1200 seconds from full charged volume (rated voltage at 5.4V) in room condition. It is obvious that the self-discharge characteristic of supercapacitor is voltage-dependent with time. According to the HV100F supercapacitor datasheet, the rated leakage current is 0.26mA. This value serves as a baseline to indicate the dissipated power of supercapacitor under no load condition, hence determining the numerical value of E_{dc}. Figure 6-22 shows the average rate of charge voltage of HV100F supercapacitor with constant charge current. This experiment is carried in simulation as its model has been validated in previous section. Moreover, it is difficult to supply accurate small current to determine the characteristics of supercapacitor. In Figure 6-22, the supercapacitor suffers from power dissipation with the charge current of 0.26mA (Average discharge rate at -70.0637μV/s). The new charge current baseline is approximately located at 0.97mA.

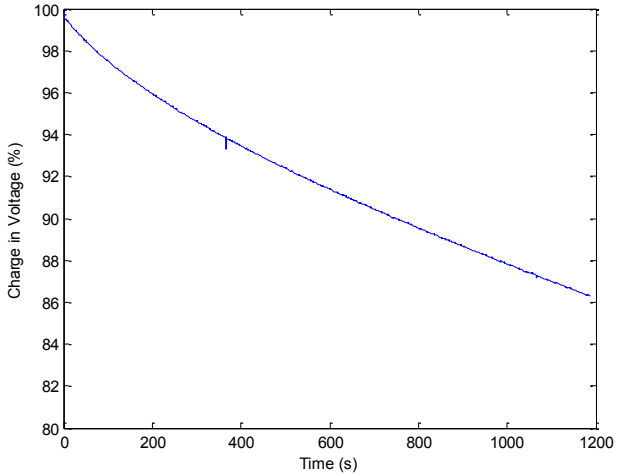

Figure 6-21 Supercapacitor self-discharge characteristics under no load condition

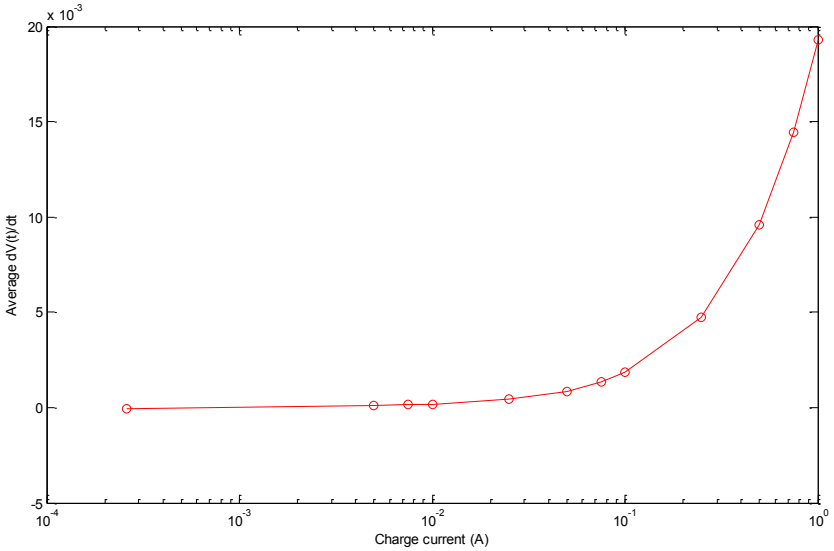

Figure 6-22 Rate of charge voltage of HV100F supercapacitor with constant charge current (No load)

Assuming the supercapacitor is charged to its nominal voltage level, to simplify the calculation; it could be assumed that the dissipated capacitor voltage remains constant. Hence, the self-discharge power of supercapacitor is $P_{sdc} = 5.431mW$. Its respective dissipate energy within T_1 and T_2 are $E_{sdc1} = 0.10864J$ and $E_{sdc2} = 19.4466J$.

For the configuration with solar illuminance of 770×100 lux, the IMSEM could be always be in SoC state, as P_h is larger than summation P_{dc} and P_{sdc}. Such

configuration has indefinite operation time as long as PV current is available. The other two configurations have negative energy voltage during IMSEM's active mode, as the resultant energy E_{u1} is in negative ($E_{h1} < E_{dc1} + E_{sdc1}$). However, the IMSEM remain in charged state as the generated current has overcome the dissipated power by IMSEM's inactive mode and HV100F self-discharge characteristic ($E_{h2} > E_{dc2} + E_{sdc2}$). Despite the voltage drop within T_1, one should note that the generated PV current should have charged out its voltage level to original state, which overcomes the average voltage drop of 0.125V during IMSEM's active mode. Table 6-7 outlines the charged current that affects the SoC of IMSEM. Note that the charged current that below 0.001 has insufficient power to maintain the IMSEM at it nominal operating mode, as the supercapacitor's voltage drop continuously. With the charged current at 0.005A, the IMSEM is able to have positive average rate of charge voltage, yielding positive E_u during T_2. Its respective total charged time is 7763s. With this the IMSEM need approximate 2.15 hours to charge supercapacitor back to its original voltage level before the next dutycycle. Any charged current that above 0.01A has sufficient charge rate and time within 3600s, which is within the time duration set in this paper. Moreover, the supply current at 0.01A could be easily achieved with many commercial PV cells with the panel area of 30cm×30cm, which make the energy harvesting system to be possible for IMSEM's system framework.

Table 6-7 Total charge time of IMSEM to overcome voltage drop (0.125V)

Charge current (mA)	Average rate of charge voltage, $dV_{scap}(t)/dt$ (V/s)	Total charge time (s)
0.26	-70.0637µ	Inf.
0.5	-65.4465µ	Inf.
1	-55.73µ	Inf.
5	22.543µ	7763
10	105.8499µ	1653
50	759.4429µ	230

100	1.63183m	107
500	8.1277m	22
1000	19.2979m	9

6.5.2 Scavenging energy from natural solar irradiance

Relevant solar irradiance data for central Manchester (provided by British Data Archive Centre (BADC)) were used to carry out energy calculations in this section. Figure 6-23 shows the monthly solar irradiance recorded at the Rosthern No 2 monitoring station from August 2013 to July 2014.

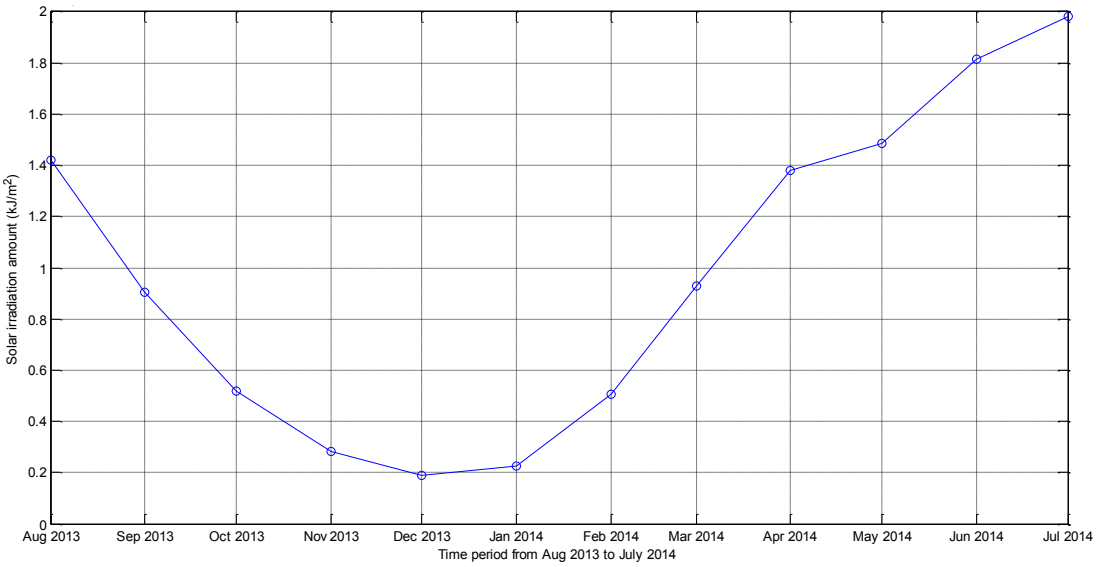

Figure 6-23 Averaged monthly solar irradiance energy nearby Manchester area – Rosthern No 2 Monitoring Station (MIDAS station number: 57199).

The period from November 2013 to January 2014, Manchester area has lowest solar irradiance. It is due to the winter season which has the shortest day time of the year. During this period, two sets of a 10-day data are extracted for evaluating energy harvesting performance: July 5, 2013 to July 15, 2013 (dataset A) and January 5, 2014 to January 15, 2014 (dataset B), as shown in Figure 6-24. There are significant differences between these two datasets, the average solar irradiance energies are 262520kJ/m^2 and 19340kJ/m^2 respectively. In other words, the PV

arrays have much higher ambient energy resource for harvesting in summer (approximate 1300% higher in winter season). Apart from the solar irradiance, the temperature on the surface of PV array is the other important parameter in solar energy scavenging. BADC has provided daily temperature data which are recorded twice a day (0900 and 2100). The temperature data is loaded into the developed simulation model.

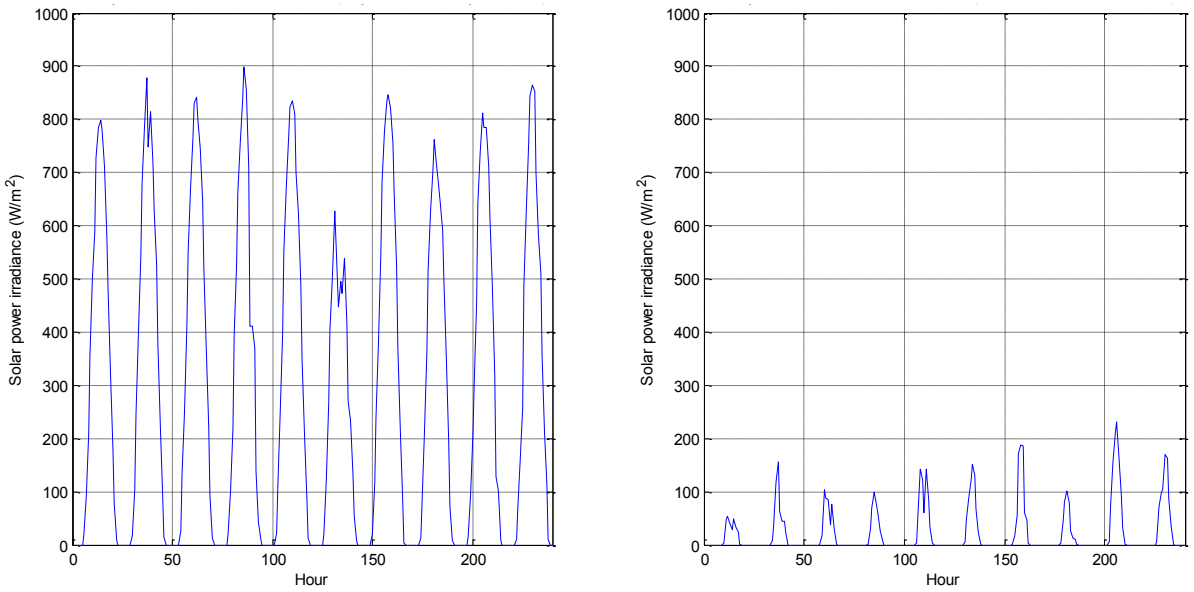

(a) (b)

Figure 6-24 10 days solar irradiance data nearby Manchester area – Rosthern No 2 Monitoring Station (MIDAS station number: 57199): (a) July 5-15, 2013, (b) Jan 5-15, 2014

Figure 6-25 shows the temperature variations at which the above irradiance was achieved, respectively. These 2 datasets are then integrated into the simulation model. The converter displayed the regulating voltage level, battery charging and delivery of subsequent power to energy consumer. In this experiment, the buck-boost converter is virtually implemented into the simulation. The generated PV current, I_{pv} is illustrated in Figure 6-26. The generated current in winter season (dataset B) experienced a relatively low PV current (average 1.2639Ah). While in summer, the PV solar panel is sufficient to harvest average 36.48375Ah. It should be noted that the PV current has raw fluctuating currents which are critically dependent on the

weather conditions; a converter is required before the power is transmitted to the energy storage module. Both datasets have average generated current that is above the required charge current of IMSEM's equilibrium state.

The power characteristic of supercapacitor array is evaluated with average for 24 hours. By observing the simulated result in Figure 6-27, dataset A (during summer) has positive I_{pv} in earlier time (approximate at 0400), the IMSEM has positive supply current which could be charged to its nominal voltage within 5000 seconds. As for dataset B (during winter), the PV cell starts generating current at approximate 0900. It has shorter operating period compared to the performance during summer time. Figure 6-28 shows the current drawn by IMSEM for 24 hours cycles. The spikes shows supercapacitor array has reached above 4.8V, thus providing sufficient power to activate the IMSEM for monitoring tasks. It also shows that there are great differences in energy supply along the timeline, the IMSEM energy is insufficient to power up the system during night time. Alternative methods or secondary energy buffer should be implemented to prevent system's shut down.

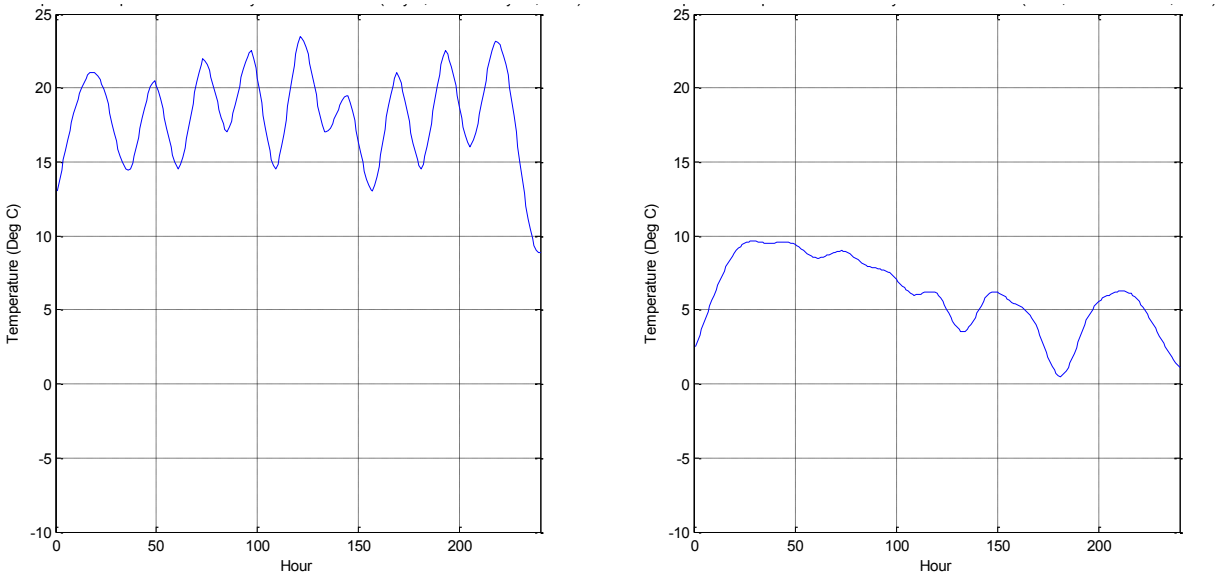

(a) (b)

Figure 6-25 10 days temperature data nearby Manchester area – Rosthern No 2 Monitoring Station (MIDAS station number: 57199): (a) July 5-15, 2013, (b) Jan 5-15, 2014

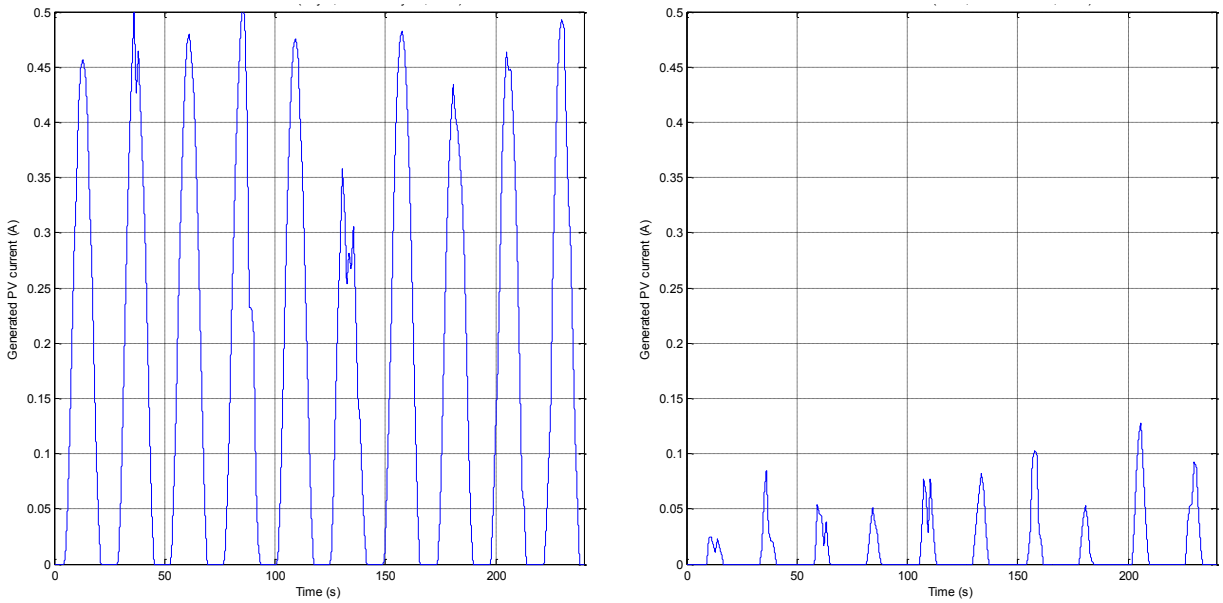

(a) (b)

Figure 6-26 10 days generated PV current from SolarTec KS10T solar panel): (a) July 5-15, 2013, (b) Jan 5-15, 2014

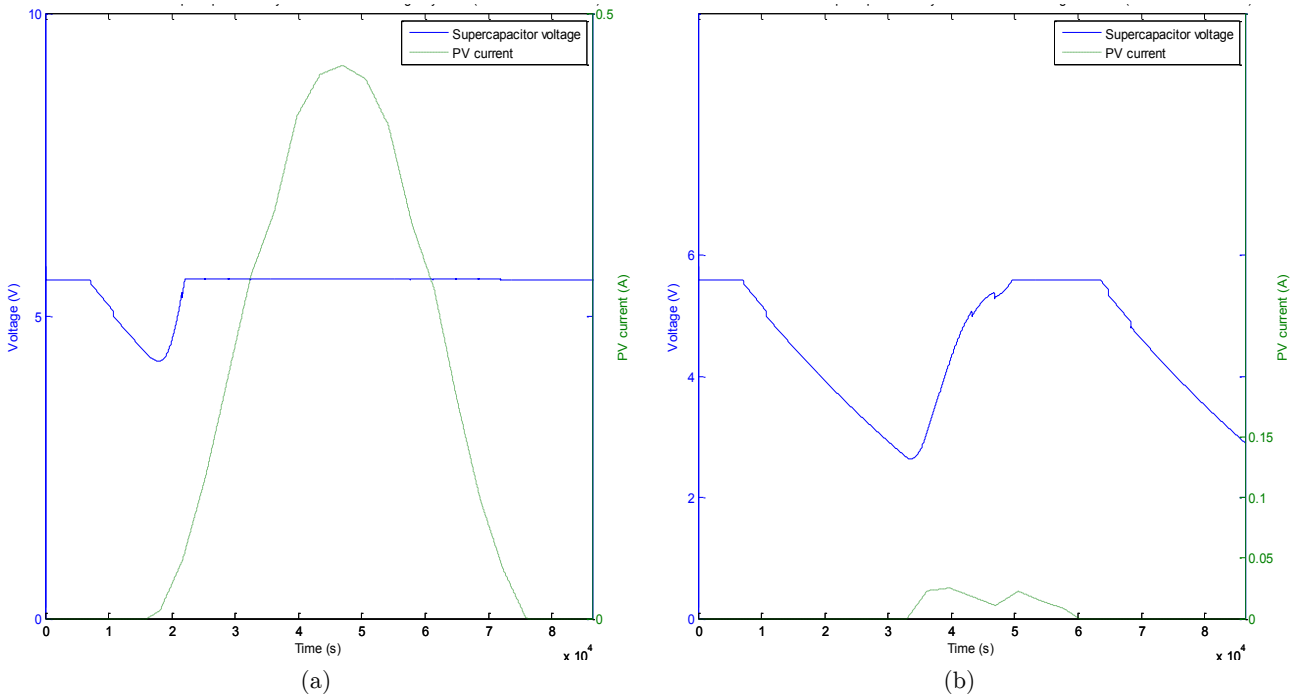

(a) (b)

Figure 6-27 Simulated power characteristics of supercapacitor array: (a) July 5-15, 2013, (b) Jan 5-15, 2014

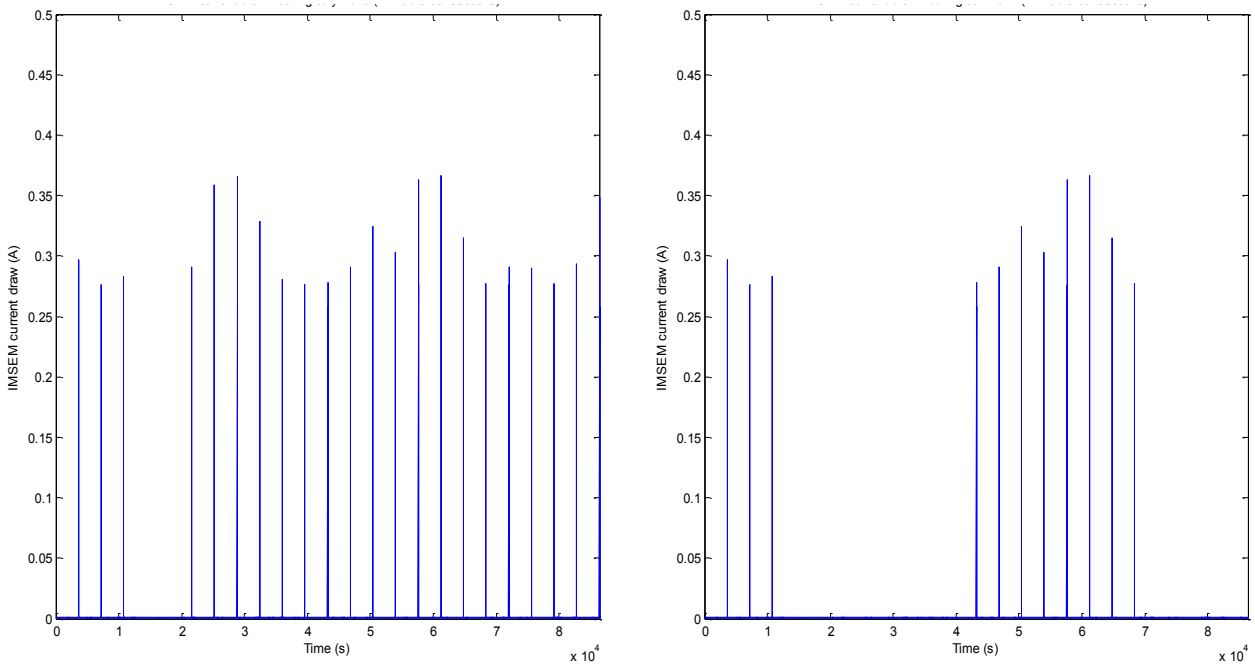

(a) (b)

Figure 6-28 Simulated current drawn of IMSEM with voltage level of supercapacitor array: (a) July 5-15, 2013, (b) Jan 5-15, 2014

6.6 Summary

A series of experiments and analysis are carried out to validate the performance of IMSEM on fault diagnostics of DC motor (rotor unbalance) and 3-phase induction motor (phase imbalance). With sufficient training datasets, the in-built intelligent algorithm with LIBSVM has the ability to indicate faulty datasets, thus triggering alarm signal for monitoring attention. For fault diagnostics of rotor imbalance, the IMSEM has reached the accuracy of 94% of fault diagnostic. On the other hand, the IMSEM has the ability to carry fault detection and diagnostics on 3-phase induction motor where its accuracy is at 93%. For energy sustainability, the IMSEM has successfully maintained its minimum power consumption at 16.8mW. With the lighting source from normal ceiling light (Approximate solar irradiance of 80W/m^2), the IMSEM has the ability to carry out periodic monitoring task at every 1 hour (total charge time is smaller than 1653 seconds, referring from Table 6-7). Such energy consumption characteristics have ensured its flexibility with other possible

ambient energy sources, which provide long-term power harvesting techniques in the future design.

Chapter 7
Achievements, conclusion, contributions to knowledge and suggested future work

This chapter outlines the progress made throughout the research project. Achievement for each objective is addressed. It is then followed by an overall conclusion of the proposed intelligent sensor system. Future prospects of the research work are also presented as research directions in the next endeavour.

7.1 Review of the objectives and achievements

This Thesis presents a novel system framework of decentralised IS system for RMD. The proposed system framework is then realised through practical implementation and design of the hardware system. An energy-aware software and hardware module is integrated into the system to enhance power efficiency throughout the monitoring process.

Referring to the objectives outlined in section 1.4.2, the relative achievements could be addressed as listed below:

1. Objective 1: To review the research status in the deployment of smart sensors for machinery condition monitoring and diagnostics

   The research background of RMD and smart sensor technology is studied as discussed in Chapter 2. Based on the literature review, the definition of IS system has been fuzzily defined. The limitation of IS system mainly focuses on its hardware robustness and capability of computation. Moreover, the power budget of an IS system for the RMD has not been well studied.

   By reviewing the above research works, the research questions for the project is outlined. First, the selection of hardware system is based upon the integrated circuit system with good memory space, computational speed and energy consumption. Second, suitable mathematical algorithms and models are studied and implemented, aiming to provide suitable software architecture for signal analysis and decision making. The energy budget for the proposed system is set as another primary objective of the research project.

2. Objective 2: To design an embedded monitoring system with on-board feature extraction , feature comparison and decision making

   To efficiently analyse the measured signals, several statistical feature extractions are applied on the IMSEM's computation model: mean, rms, standard deviation,

kurtosis and power spectrum peak. The details of the statistical equations are discussed in section 4.3.1.2. All calculated parameters are saved into the removable data storage module as discussed in section 3.5. To fuse extracted feature components, a data fusion layer with the SVM is integrated, as introduced in 4.3.1.3. 2 possible outputs are generated from the SVM algorithm: {healthy} and {alarm}, which summarises the diagnostic report from the IMSEM to other system platform or human experts. The performances of the integrated intelligent algorithms are validated through a series of experiments as discussed in Chapter 6.

3. Objective 3: To establish a low-power wireless communication system using XBee

   To remotely send the diagnostics report to other platforms, an XBee is successfully integrated to the IMSEM. The model selection and integration of XBee is well discussed in section 3.6.1. There are two types of XBee by Digi Corporation: XBee 802.15.4 and XBee Pro, which have different transmission capability and energy characteristics. By studying the product specification and rationale, XBee 802.15.4 is selected due to its significant low energy consumption as compared to the XBee Pro. At the end of the system design, the IMSEM has the ability to send remote signals up to a range of 15m indoor in the laboratory.

4. Objective 4: To apply time and frequency domain analysis on rotating machinery induced vibration, such as Fourier transform

   Statistical algorithms such as mean average, rms, standard deviation, kurtosis are applied into IMSEM. For frequency domain analysis, an embedded FFT algorithm is well implemented into the developed sensing device. The IMSEM has the ability to perform 2048-point FFT with 16-bit data register. With the default sampling frequency at 5kHz, its respective FFT resolution is 4.88Hz/bin.

5. Objective 5: To implement hibernate mode and other power management techniques to prolong operation life

An energy-aware system module of the IMSEM is developed as elaborated in Chapter 5. To ensure its compatibility with low power harvesting module, different technical methods are applied to reduce the energy consumption to its minimum level (compliant with hardware system). The peripheral computation core, operated with an 8-bit MCU, serves as the management unit to shut down unwanted system modules when turning into inactive modes. The MCU itself turns into a hibernate mode with retained interrupt service handler to wake up the IMSEM at the next time interval. By carrying out the practical test, the 8-bit MCU only draws 4μA at an operating voltage of 4.8V (19.2μW). With the overall integrated PCB, the total current drawn by the IMSEM in inactive mode is 1.1mA (5.28mW), whilst other energy consumptions are contributed by current leakage and current shut down of electronic components of the IMSEM.

The performance of the IMSEM is validated through practical experiments and simulations. With the PV current generated from constant light source on the ceiling (0.01A) with 35cm×30cm solar panel, the IMSEM has the ability to overcome voltage drop of 0.125V in active modes, which provide sufficient energy storage for the next monitoring operation.

6. Objective 6: To validate the performance of working prototype using an induction motor test rig running under different operating conditions

Two types of motor test rigs are utilised in this research, as deliberated in Chapter 6. First, the MEMS accelerometer is calibrated and validated with conventional data acquisition system comprising of conventional accelerometer by Brüel & Kjær and commercial data acquisition system by National Instruments. With the coherence of both vibration signals, the MEMS accelerometer with the IMSEM successfully provides accurate peak amplitudes at dominant frequency components. Subsequently, the IMSEM is validated by diagnosing the rotor unbalance of a DC motor test rig. With the trained SVM model, the IMSEM has reached the fault diagnostic accuracy of 94%. Similar procedure is carried out on

diagnosing voltage phase imbalance on the 3-phase induction motor test rig. The IMSEM has an accuracy of 93% in the latter experiment.

7. Objective 7: To design, build a test a final working prototype with a friendly user interface

   A respective PCB with neat unit packaging design of the IMSEM is fabricated at the end of the project, as depicted in Figure 3-21. To communicate with the IMSEM, a serial terminal is used as an end-user interface to monitor/debug the IMSEM. Four GPIO pins are reserved for further expansions with other system modules in the future. The working prototype is then put to test as outlined in the next objective.

7.2 Conclusions

Conclusions can be drawn throughout the research with the mature development of micro-scaled electronic technologies and the design of a decentralised intelligent sensor for RMD system. The proposed intelligent sensor system targeted for periodic monitoring on the working prototype presents a fundamental milestone of intelligent learning model to carry decentralised condition monitoring diagnostics. The sought sensing unit has the ability to carry out signal acquisition, signal conditioning and analysis on a single sensing node to feature an easy extraction and early fault detection to allow repairs, planned and executed independently. They are several advantages over conventional sensors in the aspects of user experience, interface and power management whereby the spectrum data can be further developed to engage for fixed frequency bands. The user interface can identify the applications for large or small frequency bands with agreement for the neutral network oriented to intranet/internet implementation to diagnose real health condition of any rotating machines in real-time to enhance both the management maintenance and production to obtain predictive results and conclusion. This is an innovative novel approach to interface with mobile unit and more works can be done to enhance the reliability of

mobile devices with advanced electronic components, emerging harvesting devices, high capacity of wireless technology and A.I analogy.

In terms of functionality, the key findings of the IMSEM has inbuilt intelligent algorithms which computes 5 feature components within the sensing framework. Experiments show that the extracted mean average component does not contribute much useful information in both experiments of the DC motor test rig and 3-phase induction motor test rig. Hence, it is suggested that this feature component could be omitted for these two types of condition monitoring.

The indoor constant energy could be sourced with the integration of energy harvesting and energy storage module by using supercapacitor is taken into account. The testing shows that the efficiency of the system draws an average of 0.22A and 3.5mA (16.8mW) during its active and inactive modes respectively and only requires 4.8V to charge up the IMSEM. This energy consumption of the IMSEM is relatively low and to perform at such a low photovoltaic (PV) current, an energy array of 10mA could be easily harvested from the light irradiance on the ceiling. In addition, the low current consumption in inactive mode provides the spare time to charge up the IMSEM. Based on the simulation and analysis outlined in section 6.5, the IMSEM has constant operating characteristic with constant energy harvesting source provided that the energy buffer is fully charged. While for outdoor monitoring condition, the IMSEM has insufficient power input at night, with losses of 4 and 13 operating duty-cycles in summer and winter respectively. Such a drawback shall be considered with a secondary energy buffer to be included in the future design. The IMSEM has also the potential to scavenge energy from outdoor global solar irradiance, where its voltage level could be maintained above 4.8V to prevent a system shut down.

The results indicate an innovative potential of the decentralised sensing system with an embedded single chip and MCU and energy harvesting awareness have enabled costs saving on material and labour, unscheduled shutdown time by

50% and 75% respectively, without undergoing a complicated development process for RMD deployment under time-varying rotation speed and large extraneous shocks for future industries.

7.3 Contribution to knowledge

This research work has made the following contributions to knowledge as it has:

- Established a system framework of intelligent sensor system for rotating machinery diagnostics, has the ability of signal acquisition, signal conditioning, signal analysis and decision making within a single sensing node featuring an easy extraction and early fault detection to allow repairs, planned and executed independently. More improvements could be done to simplify the data-reading, extraction and dissemination of information.
- Presented a compliant embedded data format of rotating machinery diagnostics with the OSA-CBM format to resolve multiple vibration sources, such as low signal to noise ratios and time-varying statistical parameters.
- Practically developed and analysed the energy budget of intelligent sensor system for periodic machinery monitoring strategy by means of A.I tools to send signals and alarms according to needs to harvest energy awareness.
- Practically evaluated the MEMS accelerometer on machinery condition monitoring compliant with embedded system design.

7.4 Suggested future work

Despite the successful development of the presented sensor system, there are several drawbacks which can be tackled in future work:

7.4.1 Intelligent algorithms of fault diagnostics

Currently, only one type of SVM kernel, the linear kernel is being applied as the monitoring algorithm for the IMSEM. To enhance the robustness of fault diagnostic, several SVM kernels are suggested as future implementation: polynomial, radial basis function (RBF) and sigmoid [96]. For further diagnostics which consist of larger training and test samples, higher-dimensional kernels such as polynomial and RBF shall give better classification outputs [125], [136]. With external memory and ability for floating-points calculations, it is believed that computation on large datasets with different kernels could be realised within the system architecture of the IMSEM.

7.4.2 Extended architecture of energy management module

As concluded in sections 6.6 and 7.2, secondary energy buffer modules should be taken into account in future energy storage module design. As proposed by [75], a Lithium polymer battery could be integrated as supplementary back-up to prevent the voltage drop below 4.8V, thus providing a stable operating lifetime of the IMSEM. Such a design has several advantages over conventional energy storage module, in which - both types of energy buffer units (supercapacitor and battery) tend to overcome each other's drawback (discussed in section 2.4.1.2) to establish a robust energy storage module.

Moreover, current IMSEM does not practically include buck/boost converter and maximum power point tracker for scavenging solar energy. To provide stable power supply at its maximum power point, such a design is necessary to be taken into account for future design.

7.4.3 Performance measurements of IMSEM

Currently, the proposed system has not been test. Its robustness in RMD system shall be tested practically to ensure the deployment of IMSEM in machinery monitoring condition, which might be operated in harsh environment.

According to the datasheet [86], XBee 802.15.4 operates at the frequency range between 2.4GHz to 2.48GHz. This frequency band has been divided into 16 channels, with each interval of 5MHz. However, such frequency band fall within the unlicensed band of ISM. Which the IMSEM communicate is subjective to disturbance from other wireless signals, affecting its reliability in critical monitoring condition. Hence, A robust wireless communication from remote sensing device shall be a future direction to enhance the reliability of IMSEM's communication.

In terms of practical implementation, the advantage of IMSEM on cost and plant's operation shall be assessed. It is estimated that with the predictive maintenance characteristic of IMSEM would reduce the unscheduled downtime and labour cost as stated in Chapter 2. However, there is lack of quantitative data to support the statement. More analysis shall be carried out to determine performance of IMSEM in practical applications.

7.4.4 Optimal power management in wireless sensing network

Currently, there are 2 system platforms being involved throughout the research study: the IMSEM and end user interface on the human expert's computer. To realise practical deployment, a wireless sensing network for the IMSEM is the next direction to expand the monitoring scale and capability. With the functional and energy budget being determined in this research work, a network topology with optimal power management shall be the next direction of a future research project.

Bibliography

[1] R. Barron, *Engineering condition monitoring: practice, methods and applications*. Harlow: Longman, 1996.

[2] A. Kelly, *Strategic maintenance planning*. Oxford: Elsevier Butterworth-Heinemann, 2006.

[3] J. Fitch, "Proactive Maintenance can Yield More than a 10-Fold Savings Over Conventional Predictive/Preventive Maintenance Programs," in *Predictive Maintenance Indaba Proceedings*, South Africa, 1992, pp. 1–9.

[4] H. P. Bloch and J. J. Hoefner, *Reciprocating Compressors: Operation & Maintenance*. Gulf Professional Publishing, 1996.

[5] V. T. Do and U.-P. Chong, "Signal Model-Based Fault Detection and Diagnosis for Induction Motors Using Features of Vibration Signal in Two-Dimension Domain," *Strojniški vestnik – Journal of Mechanical Engineering*, vol. 57, no. 9, pp. 655–665, 2011.

[6] E. B. Halim, S. L. Shah, M. J. Zuo, and M. A. A. S. Choudhury, "Fault detection of gearbox from vibration signals using time-frequency domain averaging," in *American Control Conference, 2006*, 2006, pp. 4430–4435.

[7] R. B. W. Heng and M. J. M. Nor, "Statistical analysis of sound and vibration signals for monitoring rolling element bearing condition," *Applied Acoustics*, vol. 53, no. 1–3, pp. 211–226, Jan. 1998.

[8] M. Tsypkin, "Induction motor condition monitoring: Vibration analysis technique - A practical implementation," in *Electric Machines Drives Conference (IEMDC), 2011 IEEE International*, 2011, pp. 406–411.

[9] H. G. Sedding, S. R. Campbell, G. C. Stone, and G. S. Klempner, "A new sensor for detecting partial discharges in operating turbine generators," *IEEE Transactions on Energy Conversion*, vol. 6, no. 4, pp. 700–706, Dec. 1991.

[10] Y.-J. Kim, D.-H. Hwang, B.-C. Shin, D.-Y. Park, and J.-W. Kim, "Development of continuous partial discharge monitoring system for generator stator insulations," in *Conference Record of the 2000 IEEE International Symposium on Electrical Insulation, 2000*, 2000, pp. 5–8.

[11] G. R. Ibrahim and A. Albarbar, "Comparison between Wigner–Ville distribution- and empirical mode decomposition vibration-based techniques for helical gearbox monitoring," *Proceedings of the Institution of Mechanical Engineers, Part C: Journal of Mechanical Engineering Science*, Jun. 2011.

[12] J. Lin, "An integrated time domain averaging scheme for gearbox diagnosis," in *8th International Conference on Reliability, Maintainability and Safety, 2009. ICRMS 2009*, 2009, pp. 808–812.

[13] G. K. Singh and S. A. S. Al Kazzaz, "Development of an Intelligent Diagnostic System for Induction Machine Health Monitoring," *IEEE Systems Journal*, vol. 2, no. 2, pp. 273–288, Jun. 2008.

[14] H. Wang and P. Chen, "Fuzzy Diagnosis Method for Rotating Machinery in Variable Rotating Speed," *Sensors Journal, IEEE*, vol. 11, no. 1, pp. 23 –34, Jan. 2011.

[15] W. Wang, "A Hybrid Fuzzy System for Real-Time Machinery Health Condition Monitoring," in *Fuzzy Systems*, A. Taher, Ed. InTech, 2010.

[16] IEEE, "IEEE Standard for a Smart Transducer Interface for Sensors and Actuators - Common Functions, Communication Protocols, and Transducer Electronic Data Sheet (TEDS) Formats," *IEEE Std 1451.0-2007*, pp. 1 –335, 2007.

[17] IEEE, "IEEE Standard for a Smart Transducer Interface for Sensors and Actuators-Network Capable Application Processor (NCAP) Information Model," *IEEE Std 1451.1-1999*, p. i, 2000.

[18] Y.-J. Kim, K.-C. Lee, D.-H. Hwang, and D.-S. Kang, "Technologies and cost evaluation of condition monitoring and diagnosis system under ubiquitous environment," in *Proceedings of 2005 International Symposium on Electrical Insulating Materials, 2005. (ISEIM 2005)*, 2005, vol. 3, pp. 857–860 Vol. 3.

[19] X. Chen, X. Jiang, and L. Wang, "Development on ARM9 System-on-chip Embedded Sensor Node for Urban Intelligent Transportation System," in *Industrial Electronics, 2006 IEEE International Symposium on*, 2006, vol. 4, pp. 3270 –3275.

[20] G. J. Yun, S.-G. Lee, J. Carletta, and T. Nagayama, "Decentralized damage identification using wavelet signal analysis embedded on wireless smart sensors," *Engineering Structures*, vol. 33, no. 7, pp. 2162–2172, Jul. 2011.

[21] GBI Research, "Microcontroller Market to 2015 - Commissioning of Smart Grid Projects to Create Market Opportunities in Advanced Metering Infrastructure and Grid Equipment," GBI Research, GBISC020MR, Jan. 2012.

[22] S. Glass, "The Impact of the $1 32bit Microcontroller," in *Austronics*, New Zealand, 2006.

[23] Digi-Key Corporation, "Microcontroller prices will fall despite strong demand," *Digi-Key Corporation*, 20-Aug-2010.

[24] J. P. Lynch, "Decentralization of Wireless Monitoring and Control Technologies for Smart Civil Structures," Ph. D., Stanford University, 2002.

[25] W. Wang, "An Intelligent System for Machinery Condition Monitoring," *IEEE Transactions on Fuzzy Systems*, vol. 16, no. 1, pp. 110–122, Feb. 2008.

[26] J.-M. Stauffer, B. Dutoit, and B. Arbab, "Standard MEMS Sensor Technologies for Harsh Environment," in *The Institution of Engineering and Technology Seminar on MEMS Sensors and Actuators, 2006*, 2006, pp. 91–96.

[27] Microchip Technology Inc., "PIC32MX5XX/6XX/7XX Family Data Sheet," Microchip Technology Inc., DS61156G, 2011.

[28] STMicroelectronics, "STM32F205xx, STM32F207xx," STMicroelectronics, 15818 Rev 8, Dec. 2011.

[29] Cypress Semiconductor Corporation, "PSoC5 CY8C55 Family Datasheet," Cypress Semiconductor Corporation, 001-66235 Rev. *D, Feb. 2012.

[30] Zhu Z and R. Pietruszkiewicz, "Architecture Investigation of Energy Harvester for Wireless Sensor Nodes."

[31] J. A. Paradiso and T. Starner, "Energy scavenging for mobile and wireless electronics," *Pervasive Computing, IEEE*, vol. 4, no. 1, pp. 18–27, Mar. 2005.

[32] T. Christen and M. W. Carlen, "Theory of Ragone plots," *Journal of Power Sources*, vol. 91, no. 2, pp. 210–216, Dec. 2000.

[33] A. Sanchez, S. Blanc, S. Climent, P. Yuste, and R. Ors, "SIVEH: Numerical Computing Simulation of Wireless Energy-Harvesting Sensor Nodes," *Sensors*, vol. 13, no. 9, pp. 11750–11771, Sep. 2013.

[34] S. Escolar, S. Chessa, and J. Carretero, "Energy-neutral networked wireless sensors," *Simulation Modelling Practice and Theory*, vol. 43, pp. 1–15, Apr. 2014.

[35] R. Ma, G. M. P. O'Hare, and M. J. O'Grady, "Embedded Intelligence: Enabling In-Situ Power Management for Wireless Sensor Networks," in *Smart Sensing and Context*, P. Havinga, M. Lijding, N. Meratnia, and M. Wegdam, Eds. Springer Berlin Heidelberg, 2006, pp. 244–247.

[36] S. Y. Yurish, "Sensors: Smart vs. Intelligent," *Sensors and Transducers*, vol. 114, no. 3, 2010.

[37] K. M. Tsang and W. L. Chan, "Non-destructive stiffness detection of utility wooden poles using wireless MEMS sensor," *Measurement*, vol. 44, no. 6, pp. 1201–1207, Jul. 2011.

[38] Rmdan Abdussalm Ashnibha, "An investigation into current and vibration signatures of three phase induction motors," Ph. D., Manchester Metropolitan University, Manchester, 2012.

[39] J. Salvado, A. Espírito-Santo, and M. Calado, "An Intelligent Sensor Array Distributed System for Vibration Analysis and Acoustic Noise Characterization of a Linear Switched Reluctance Actuator," *Sensors*, vol. 12, no. 6, pp. 7614–7633, Jun. 2012.

[40] J. B. Janier and M. F. Z. Zaharia, "Condition Monitoring System for Induction Motor Using Fuzzy Logic Tool," in *2011 First International Conference on Informatics and Computational Intelligence (ICI)*, 2011, pp. 3–7.

[41] W. Wang and O. A. Jianu, "A Smart Sensing Unit for Vibration Measurement and Monitoring," *IEEE/ASME Transactions on Mechatronics*, vol. 15, no. 1, pp. 70–78, Feb. 2010.

[42] G. A. Alonso, J.-L. Marty, J. M. Gutiérrez, and R. Muñoz, *Implementation of the discrete wavelet transform used in the calibration of the enzymatic biosensors*. INTECH Open Access Publisher, 2011.

[43] S. Knezevic and R. Stojanovic, "MSP430 implementation of wavelet transform for purposes of physiological signals processing," in *Education and Research Conference (EDERC), 2012 5th European DSP*, 2012, pp. 119–123.

[44] Q. He, R. Yan, F. Kong, and R. Du, "Machine condition monitoring using principal component representations," *Mechanical Systems and Signal Processing*, vol. 23, no. 2, pp. 446–466, Feb. 2009.

[45] I. M. Devonshire, M. J. Preston, E. J. Dommett, K. L. Murphy, and S. A. Greenfield, "Design and evaluation of a low-cost respiratory monitoring device for use with anaesthetized animals," *Lab Anim*, vol. 43, no. 4, pp. 382–389, Oct. 2009.

[46] J.-D. Son, G. Niu, B.-S. Yang, D.-H. Hwang, and D.-S. Kang, "Development of smart sensors system for machine fault diagnosis," *Expert Systems with Applications*, vol. 36, no. 9, pp. 11981–11991, Nov. 2009.

[47] H. Nejjari and M. E. H. Benbouzid, "Application of fuzzy logic to induction motors condition monitoring," *IEEE Power Engineering Review*, vol. 19, no. 6, pp. 52 –54, Jun. 1999.

[48] I. J. Karassik, *Centrifugal Pump Clinic, Second Edition, Revised and Expanded*, 2nd ed. CRC Press, 1989.

[49] M. Koc, J. Ni, and J. Lee, "Introduction of e-Manufacturing," in *Proceedings of the 5th International Conference on Frontiers of Design and Manufacturing (ICFDM'2002)*, 2002, pp. 43–47.

[50] T. Han and B.-S. Yang, "Development of an e-maintenance system integrating advanced techniques," *Computers in Industry*, vol. 57, no. 6, pp. 569–580, Aug. 2006.

[51] Penn State University, The Boeing Company, and MIMOSA, "Open Systems Architecture for Condition-based Maintenance (OSA-CBM) - Primer." MIMOSA, Aug-2006.

[52] K. Lee, R. X. Gao, and R. Schneeman, "Sensor network and information interoperability integrating IEEE 1451 with MIMOSA and OSA-CBM," in *Proceedings of the 19th IEEE Instrumentation and Measurement Technology Conference, 2002. IMTC/2002*, 2002, vol. 2, pp. 1301–1305 vol.2.

[53] M. Bengtsson, "Standardization Issues in Condition Based Maintenance," presented at the Proceedings of the 16th International Congress on Condition Monitoring and Diagnostic Engineering Management, 2003.

[54] G. Niu, B.-S. Yang, and M. Pecht, "Development of an optimized condition-based maintenance system by data fusion and reliability-centered maintenance," *Reliability Engineering & System Safety*, vol. 95, no. 7, pp. 786–796, Jul. 2010.

[55] D. Niyato, E. Hossain, M. M. Rashid, and V. K. Bhargava, "Wireless sensor networks with energy harvesting technologies: a game-theoretic approach to optimal energy management," *IEEE Wireless Communications*, vol. 14, no. 4, pp. 90–96, Aug. 2007.

[56] A. S. Weddell, G. V. Merrett, N. R. Harris, and N. M. White, "Energy devices for sensor networks: Properties for simulation and deployment," in *Wireless Communication, Vehicular Technology, Information Theory and Aerospace Electronic Systems Technology, 2009. Wireless VITAE 2009. 1st International Conference on*, 2009, pp. 26 –30.

[57] J. M. Gilbert and F. Balouchi, "Comparison of energy harvesting systems for wireless sensor networks," *Int. J. Autom. Comput.*, vol. 5, no. 4, pp. 334–347, Oct. 2008.

[58] A. Harb, "Energy harvesting: State-of-the-art," *Renewable Energy*, vol. 36, no. 10, pp. 2641–2654, Oct. 2011.

[59] MIDE, "MIDE Piezoelectric Energy Harvesters," MIDE, Datasheet, Jan. 2013.

[60] PMG Perpetuum, "Vibration Energy Harvesters," Perpetuum Ltd, Datasheet 66000 - Rev 4.0, Oct. 2013.

[61] Micropelt, "MPG-D655 Thin Film Thermogenerator," Micropelt, Germany, Datasheet 0056DSPG6550914v2e, Sep. 2014.

[62] "Thermo Life Energy Corp," *Thermo Life Energy Corp.* [Online]. Available: http://www.poweredbythermolife.com/. [Accessed: 15-Mar-2015].

[63] Powercast, "P1110-915MHz RF Powerharvester Receiver," Powercast, Datasheet, Apr. 2010.

[64] SolarTec, "KS10T High Efficiency Polycrystalline Photovoltaic Module," SolarTec, Datasheet ETE KS10T v8.

[65] Multicomp, "MC-SP0.8-NF-GCS," Multicomp, Datasheet, Dec. 2010.

[66] C. B. Williams, C. Shearwood, M. A. Harradine, P. H. Mellor, T. S. Birch, and R. B. Yates, "Development of an electromagnetic micro-generator," *Circuits, Devices and Systems, IEE Proceedings* -, vol. 148, no. 6, pp. 337–342, Dec. 2001.

[67] H. Kulah and K. Najafi, "An electromagnetic micro power generator for low-frequency environmental vibrations," in *Micro Electro Mechanical Systems, 2004. 17th IEEE International Conference on. (MEMS)*, 2004, pp. 237–240.

[68] H. Karl, A. Willig, and Wolisz, *Wireless Sensor Networks: First European Workshop, EWSN 2004, Berlin, Germany, January 19-21, 2004, Proceedings*. Springer Science & Business Media, 2004.

[69] H. Ostaffe, "RF-based Wireless Charging and Energy Harvesting Enables New Applications and Improves Product Design," *Mouser Electronics*. [Online]. Available: http://uk.mouser.com/applications/rf_energy_harvesting/. [Accessed: 30-Jul-2013].

[70] G. Abadal, J. Alda, and J. Agust, "Electromagnetic Radiation Energy Harvesting – The Rectenna Based Approach," in *ICT - Energy - Concepts Towards Zero - Power Information and Communication Technology*, G. Fagas, Ed. InTech, 2014.

[71] H. S. Rauschenbach, *Solar cell array design handbook the principles and technology of photovoltaic energy conversion*. New York: Van Nostrand Reinhold Co., 1980.

[72] A. Driesse, S. Harrison, and P. Jain, "Evaluating the Effectiveness of Maximum Power Point Tracking Methods in Photovoltaic Power Systems using Array Performance Models," in *IEEE Power Electronics Specialists Conference, 2007. PESC 2007*, 2007, pp. 145–151.

[73] M. G. Villalva, J. R. Gazoli, and E. R. Filho, "Modeling and circuit-based simulation of photovoltaic arrays," in *Power Electronics Conference, 2009. COBEP '09. Brazilian*, 2009, pp. 1244–1254.

[74] S. Chowdhury, S. P. Chowdhury, G. . Taylor, and Y.-H. Song, "Mathematical modelling and performance evaluation of a stand-alone polycrystalline PV plant with MPPT facility," in *2008 IEEE Power and Energy Society General Meeting - Conversion and Delivery of Electrical Energy in the 21st Century*, 2008, pp. 1–7.

[75] M. E. Glavin, P. K. W. Chan, S. Armstrong, and W. G. Hurley, "A stand-alone photovoltaic supercapacitor battery hybrid energy storage system," in

Power Electronics and Motion Control Conference, 2008. EPE-PEMC 2008. 13th, 2008, pp. 1688–1695.

[76] R. Freeland, "Energy harvesting: A Practical Reality for Wireless Sensing," Perpetuum, Jan. 2012.

[77] P. Glynne-Jones, S. P. Beeby, and N. M. White, "Towards a piezoelectric vibration-powered microgenerator," *Science, Measurement and Technology, IEE Proceedings* -, vol. 148, no. 2, pp. 68–72, Mar. 2001.

[78] M. Marzencki, Y. Ammar, and S. Basrour, *Design, Fabrication and Characterization of a Piezoelectric Microgenerator Including a Power Management Circuit*. 2008.

[79] P. D. Mitcheson, B. H. Stark, P. Miao, E. M. Yeatman, A. S. Holmes, and T. C. Green, "Analysis and optimisation of MEMS electrostatic on-chip power supply for self-powering of slow-moving sensors," 2003.

[80] G. Despesse, T. Jager, C. Jean-Jacques, J.-M. Léger, A. Vassilev, S. Basrour, and B. Charlot, "Fabrication and characterization of high damping electrostatic micro devices for vibration energy scavenging," *Proc. Design, Test, Integration and Packaging of MEMS and MOEMS*, pp. 386–390, Jun. 2005.

[81] C. Farcas, D. Petreus, I. Ciocan, and N. Palaghita, "Modeling and simulation of supercapacitors," in *Design and Technology of Electronics Packages, (SIITME) 2009 15th International Symposium for*, 2009, pp. 195–200.

[82] A. S. Weddell, G. V. Merrett, T. J. Kazmierski, and B. M. Al-Hashimi, "Accurate Supercapacitor Modeling for Energy Harvesting Wireless Sensor Nodes," *IEEE Transactions on Circuits and Systems II: Express Briefs*, vol. 58, no. 12, pp. 911–915, Dec. 2011.

[83] Maxwell Technologies, "Gateway to a New Thinking in Energy Management - Ultracapacitors," San Diego, CA, USA, 18-Jan-2005.

[84] P. Johansson and B. Andersson, "Comparison of Simulation Programs for Supercapacitor Modelling," Master of Science, Chalmers University of Technology, Gothenburg, Sweden, 2008.

[85] D. V. Ess, "PSoC1 Understanding Switched Capacitor Filters," Cypress Semiconductor Corporation, Application Note 001-43151 Rev. *B, Sep. 2011.

[86] Digi International Inc., "XBee/XBee-PRO RF Modules," 90000982_P, Jun. 2014.

[87] E. Sordiashie, "Electromagnetic Harvesting to Power Energy Management Sensors in the Built Environment," M. Sc., University of Nebraska-Lincoln, Lincoln, Nebraska, 2012.

[88] P.-O. Logerais, O. Riou, M. A. Camara, and J.-F. Durastanti, "Study of Photovoltaic Energy Storage by Supercapacitors through Both Experimental and Modelling Approaches," *Journal of Solar Energy*, vol. 2013, p. e659014, Sep. 2013.

[89] M. I. Mohamed, W. Y. Wu, and M. Moniri, "Power harvesting for smart sensor networks in monitoring water distribution system," in *2011 IEEE International Conference on Networking, Sensing and Control (ICNSC)*, 2011, pp. 393–398.

[90] J. Li, Y. Chen, and Y. Liu, "Research on a Stand-alone Photovoltaic System with a Supercapacitor as the Energy Storage Device," *Energy Procedia*, vol. 16, Part C, pp. 1693–1700, 2012.

[91] S. Peng and C. P. Low, "Prediction free energy neutral power management for energy harvesting wireless sensor nodes," *Ad Hoc Networks*, vol. 13, Part B, pp. 351–367, Feb. 2014.

[92] J. F. Nash, "Non-Cooperative Games," Ph. D., Princeton University, Princeton, 1950.

[93] D. Gunduz, K. Stamatiou, N. Michelusi, and M. Zorzi, "Designing intelligent energy harvesting communication systems," *IEEE Communications Magazine*, vol. 52, no. 1, pp. 210–216, Jan. 2014.

[94] P. Zhang, G. Xiao, and H.-P. Tan, "Clustering algorithms for maximizing the lifetime of wireless sensor networks with energy-harvesting sensors," *Computer Networks*, vol. 57, no. 14, pp. 2689–2704, Oct. 2013.

[95] U. Farooq, M. Amar, E. ul Haq, M. U. Asad, and H. M. Atiq, "Microcontroller Based Neural Network Controlled Low Cost Autonomous Vehicle," in *2010 Second International Conference on Machine Learning and Computing (ICMLC)*, 2010, pp. 96–100.

[96] C.-C. Chang and C.-J. Lin, "LIBSVM: A library for support vector machines," *ACM Transactions on Intelligent Systems and Technology*, vol. 2, no. 3, pp. 27:1–27:27, 2011.

[97] E. Garcia-Breijo, J. Garrigues, L. Sanchez, and N. Laguarda-Miro, "An Embedded Simplified Fuzzy ARTMAP Implemented on a Microcontroller for Food Classification," *Sensors*, vol. 13, no. 8, pp. 10418–10429, Aug. 2013.

[98] T. Galchev, E. E. Aktakka, and K. Najafi, "A Piezoelectric Parametric Frequency Increased Generator for Harvesting Low-Frequency Vibrations," *Journal of Microelectromechanical Systems*, vol. 21, no. 6, pp. 1311–1320, Dec. 2012.

[99] L. M. Roylance and J. B. Angell, "A batch-fabricated silicon accelerometer," *Electron Devices, IEEE Transactions on*, vol. 26, no. 12, pp. 1911 – 1917, Dec. 1979.

[100] A. Albarbar, A. Badri, J. K. Sinha, and A. Starr, "Performance evaluation of MEMS accelerometers," *Measurement*, vol. 42, no. 5, pp. 790–795, Jun. 2009.

[101] A. Albarbar, S. Mekid, A. Starr, and R. Pietruszkiewicz, "Suitability of MEMS Accelerometers for Condition Monitoring: An experimental study," *Sensors*, vol. 8, no. 2, pp. 784–799, Feb. 2008.

[102] F. Mohd-Yasin, C. E. Korman, and D. J. Nagel, "Measurement of noise characteristics of MEMS accelerometers," *Solid-State Electronics*, vol. 47, no. 2, pp. 357–360, Feb. 2003.

[103] Alps Electronic Co. Ltd., "Encoder – Hollow Shaft Type SRGA Series," Alps Electronic Co. Ltd., Tokyo, Japan, Datasheet SRGAVQ1100, 2006.

[104] Avago Technologies, "Ultra-precision 17-Bit Absolute Single Turn Encoder," Avago Technologies, United Stated, Datasheet AV02-3130EN, Sep. 2013.

[105] Analog Devices, "High Performance, Wide Bandwidth Accelerometer – ADXL001," Analog Devices, 2010.

[106] Allergo Microsystem LLC., "Micropower Ultra-Sensitive Hall-Effect Switches – A3213 and A3214," Allergo Microsystem LLC., Massachusetts, United States, Datasheet 27622.62-DS Rev. Y, Oct. 2012.

[107] Cypress Semiconductor Corporation, "CY8C29466, CY8C29566, CY8C29666, CY8C29866," Cypress Semiconductor Corporation, 38-12013 Rev. *S, Jul. 2011.

[108] Cypress Semiconductor Corporation, "Free C Compiler for PSoC Designer," *Cypress*, 27-Feb-2011. [Online]. Available: http://www.cypress.com/?id=4&rID=37785. [Accessed: 24-Dec-2013].

[109] "LMF100 High Performance Dual Switched Capacitor Filter," National Semiconductor, 1999.

[110] Cypress Semiconductor Corporation, "Two-Pole Low-pass Filter Datasheet LPF2 v3.00," Cypress Semiconductor Corporation, 001-13572 Rev. *H, Nov. 2011.

[111] G. Reynolds, "AN47310 - PSoC 1 Power Savings Using Sleep Mode," Cypress Semiconductor Corporation, 001-47310 Rev. *B, Jan. 2013.

[112] W. H. Press, S. A. Teukolsky, W. T. Vetterling, and B. P. Flannery, *Numerical Recipes in C: The Art of Scientific Computing. Second Edition.* 1992.

[113] Cypress Semiconductor Corporation, "PSoC5LP CY8C58LP Family Datasheet," Cypress Semiconductor Corporation, 001-84932 Rev. *F, May 2014.

[114] Cypress Semiconductor Corporation, "Measure two channels signal synchronous using DelSig ADC in PSoC3/5," *Cypress Semiconductor Corporation*, 21-Dec-2011. [Online]. Available: http://www.cypress.com/?id=4&rID=57084. [Accessed: 30-Jul-2013].

[115] Microchip Technology Inc., "dsPIC33EPXXX(GP/MC/MU)806/810/814 and PIC24EPXXX(GP/GU)810/814," Microchip Technology Inc., DS70616G, 2012.

[116] Atmel, "32-bit AVR Microcontroller – AT32UC3C0512C, AT32UC3C1512C, AT32UC3C1256C, AT32UC3C2512C, AT32UC3C2256C, AT32UC3C2128C," Atmel, 9166DS–AVR–01, 2012.

[117] Freescale Semiconductor, "MC56F847XX," Freescale Semiconductor, MC56F847XX, 2012.

[118] M. Kingsbury, "AN77900 - PSoC 3 and PSoC 5LP Low-power Modes and Power Reduction Techniques," Cypress Semiconductor Corporation, 001-77900 Rev. *B, Dec. 2013.

[119] LORD MicroStrain Sensing System, "IEPE-Link^{TM} -LXRS® Wireless IEPE Sensor Node," *LORD MicroStrain Sensing System*, May-2014. [Online]. Available: http://www.microstrain.com/wireless/iepe-link. [Accessed: 27-Dec-2014].

[120] GHI Electronics, "ALFAT SoC Processor," GHI Electronics, May 2013.

[121] Cypress Semiconductor Corporation, "Using IMO for UART communication in PSoC 3/5," *Cypress Semiconductor Corporation*, 14-Mar-2011. [Online]. Available: http://www.cypress.com/?id=4&rID=38638. [Accessed: 20-Jul-2012].

[122] P. Horowitz and W. Hill, *The Art of Electronics*, 2 edition. Cambridge England ; New York: Cambridge University Press, 1989.

[123] D. E. Van and A. Krishnan, "PSoC 1 Using the ADCINC ADC," Cypress Semiconductor Corporation, Application Note 001-41065 Rev. *D, Jun. 2014.

[124] C. Cortes and V. Vapnik, "Support-Vector Networks," *Machine Learning*, vol. 20, no. 3, pp. 273–297, Sep. 1995.

[125] Q. Miao, H.-Z. Huang, and X. Fan, "A comparison study of support vector machines and hidden Markov models in machinery condition monitoring," *J Mech Sci Technol*, vol. 21, no. 4, pp. 607–615, Apr. 2007.

[126] A. Boni, F. Pianegiani, and D. Petri, "Low-Power and Low-Cost Implementation of SVMs for Smart Sensors," *IEEE Transactions on Instrumentation and Measurement*, vol. 56, no. 1, pp. 39–44, Feb. 2007.

[127] A. D. Mathew, L. Zhang, S. Zhang, and L. Ma, "A review of the MIMOSA OSA-EAI database for condition monitoring systems," in *CRC Integrated Engineering Asset Management (CIEAM); Faculty of Built Environment and Engineering*, Gold Coast, Australia, 2006.

[128] Multicomp, "MC-SP10-GCS," Multicomp, Datasheet, Dec. 2010.

[129] D. Sera, R. Teodorescu, and P. Rodriguez, "PV panel model based on datasheet values," in *IEEE International Symposium on Industrial Electronics, 2007. ISIE 2007*, 2007, pp. 2392–2396.

[130] Cooper Bussmann, "PowerStor Supercapacitors HV Series," Cooper Bussmann, BU-SB 14040, 2014.

[131] B. C. B. N. Suryam, K. K. Meher, J. K. Sinha, and A. Rama Rao, "Coherence measurement for early contact detection between two components," *Journal of Sound and Vibration*, vol. 290, no. 1–2, pp. 519–523, Feb. 2006.

[132] "ISO 1940-1 Mechanical vibration – Balance quality requirements for rotors in a constant (rigid) state Part 1: Specification and verification of balance tolerances," International Standard, ISO 1940-1:2003(E).

[133] A. H. Bonnett and G. C. Soukup, "Cause and analysis of stator and rotor failures in three-phase squirrel-cage induction motors," *IEEE Transactions on Industry Applications*, vol. 28, no. 4, pp. 921–937, Jul. 1992.

[134] B. S. Payne, "Condition monitoring of electrical motors for improved asset management," Ph. D., University of Manchester, Manchester, 2003.

[135] "American National Standard for Electric Power Systems and Equipment – Voltage Ratings (60 Hertz)," American National Standards Institute, Inc., ANSI C84.1-2011, Dec. 2006.

[136] R. McCue, "A Comparison of the Accuracy of Support Vector Machine and Naive Bayes Algorithms In Spam Classification," University of California at Santa Cruz, Nov. 2009.